Title
Enabling a Laser Plasma Accelerator Driven Free Electron Laser

Author
Majernik, Nathan

Publication Date
2019

UNIVERSITY OF CALIFORNIA
Los Angeles

Enabling a Laser Plasma Accelerator Driven Free Electron Laser

A dissertation submitted in partial satisfaction
of the requirements for the degree
Doctor of Philosophy in Physics

by

Nathan Matthew Majernik

2019

ABSTRACT OF THE DISSERTATION

Enabling a Laser Plasma Accelerator
Driven Free Electron Laser

by

Nathan Matthew Majernik
Doctor of Philosophy in Physics
University of California, Los Angeles, 2019
Professor James Rosenzweig, Chair

The free electron laser (FEL) is the brightest available source of x-rays, surpassing other options by more than ten orders of magnitude. The FEL's short (∼femtosecond), high power (∼gigawatt), coherent x-ray pulses are uniquely capable of probing ultrafast and ultrasmall atomic and molecular dynamics and structure, making them an invaluable research tool for biology, chemistry, material science, physics, medicine, and other fields. Unfortunately, all extant x-ray FELs rely on long rf linacs and undulators, with a footprint of kilometers and a cost on the order of a billion dollars. This severely limits the number of x-ray FELs, with the half dozen existing installations funded at the nation state level. These facilities are significantly oversubscribed, to the detriment of scientific and technological progress. Therefore, attempts to reduce the size and cost of FELs are an active area of research in an effort to increase access to these powerful research tools, with the goal of making x-ray FELs affordable to universities and companies.

One of the approaches being researched is the laser plasma accelerator (LPA). The LPA uses an ultra-high intensity laser to eject plasma electrons from a bubble region, producing longitudinal accelerating fields more than three orders of magnitude higher than what can be achieved in an rf linac. In principle, this could shrink the FEL accelerating section from the kilometer scale to a tabletop. To date though, despite continual progress and refinement over the last decade, LPA beam quality has not yet reached the level where it can be directly used as an FEL driver due to stringent constraints on the lasing dynamics.

The BELLA FEL experiment at Lawrence Berkeley National Lab intends to decompress the beam to skirt some of the beam quality requirements, by stretching the beam longitudinally and reducing local energy spread. This dissertation will discuss the design and implementation of two subsystems essential for the successful operation of this experiment. The first of these is a coherent transition radiation bunch length diagnostic, which is required to measure the length of the LPA bunches and extrapolate other details about the experiment's performance. The second is an electromagnetic chicane which performs the decompression of the electron beam. A final chapter explores the use of advanced undulators to enable the next generation of LPA driven FELs without decompression and discusses methods for realizing such undulators.

The dissertation of Nathan Matthew Majernik is approved.

Robert Candler

Seth Putterman

Pietro Musumeci

James Rosenzweig, Committee Chair

University of California, Los Angeles

2019

To my parents

TABLE OF CONTENTS

LIST OF FIGURES

LIST OF TABLES

ACKNOWLEDGMENTS

When applying to grad schools, I was planning to join a plasma physics program. While at UCLA for the last of my school visits, a series of professors gave short talks on their research: that was my first encounter with Jamie Rosenzweig. He wasn't listed as being in their plasma division so I hadn't read up on him in advance, so his talk completely blindsided me. While I heard about his efforts to shrink particle accelerators and light sources, I also learned how bombastic and enthusiastic he was. He was clearly dreaming big, talking about multiple orders of magnitude of advancement. He was also well funded since there was a direct path for translating such advancements into technology that could benefit humanity. I scheduled a meeting with him that afternoon and in that moment solidified my grad school plans which, until then, had been completely up in the air. In these intervening years, he's been remarkably generous with both his time and funding, patient when I'm making mistakes, and always willing to listen to my latest harebrained scheme. I look forward to continuing to work with him in the coming years.

Of course, a PI's time is always split in many directions so, for an enterprise as large as PBPL, the senior research staff are essential in the smooth operation of the lab and the care and feeding of students. Thanks are due to Atsushi, Oliver, Gerard, and Brian for sharing their expertise. Yusuke, in particular, I must thank for his guidance in the design and safe use of high voltage and pulsed power systems. His use of a label maker is legendary: I found a sticker saying “DANGER PLEASE STAY AWAY THANK YOU” attached to a capacitor bank large enough to stop your heart several times over, he got the point across but was still impeccably polite. I would also like to thank Jeroen and Sam for teaching me the ropes at LBNL.

It's natural though that a grad student spends most of their time with other students. I'd like to thank the senior graduate students who helped me get my bearings during my first few years at PBPL. In particular I need to thank Phuc, my officemate who valued silence as much as I did but was always happy to answer questions and Brendan, my primary point of contact for my first, small projects with the lab and also answerer of many questions.

Students in my cohort seem to be the ones I spent the most time ‘in the trenches’ with; thank you especially to Seth for making me a better scientist during the ICONS project. The students who came after me have both taught and learned from me; thank you for making my time in the office fun and unpredictable. Thanks especially to Walter who has suffered through more of my Brilliant Ideas$^{\text{TM}}$ than anyone else.

Of course, these years haven’t only been spent inside the lab. Thank you to my friends and family who have made this grad school journey a happier time. To the 27 Guns, there’s no group of people I’d rather be lost in the desert with; to the Troika, thank you for turning our apartment into a sitcom and a home; to the nihilist down the hall, thank you for the mutual commiseration; to my fellow TWErp, thank you for the years of steady friendship, seeing you is always a highlight; to my favorIITe engineers, thanks for staying in touch and answering my dumb questions for the last decade; and thank you to the innumerable others who have made my life a little better just by being around. My family has also always been tremendously supportive throughout this process. Thank you in particular to my godmother, who has done this before and helped give me the nudges I needed. And most of all, thank you to my parents, to whom this dissertation is dedicated, for your unwavering support, your thoughtful surprises, your willingness to let me try the dangerous things that formed me into who I am, your advice, your patience, and your love.

VITA

2013-2019	UCLA, Los Angeles, California Graduate student researcher
2018	Lawerence Berkeley National Laboratory, Berkeley, CA Department of Energy Science Graduate Student Research awardee
2014	UCLA, Los Angeles, California M.S. in Physics
2013	Illinois Institute of Technology, Chicago, IL B.S. in Physics, *summa cum laude* B.S. in Applied Mathematics, *summa cum laude*
2012	Antihydrogen Laser Physics Apparatus (ALPHA) collaboration, CERN Undergraduate researcher
2009-2012	Illinois Institute of Technology, Chicago, IL Undergraduate researcher

PUBLICATIONS AND PATENTS

N. Majernik and J. B. Rosenzweig. Design of Comb Fabricated Halbach Undulators. *Instruments*, 3(58), 2019.

N. Majernik and J. B. Rosenzweig. Halbach undulators using right triangular magnets. *Physical Review Accelerators and Beams*, 22(092401), 2019.

R. Roussel, G. Andonian, et. al. Externally Heated Hollow Cathode Arc Plasma Source for Experiments in Plasma Wakefield Acceleration. *Instruments*, 3(48), 2019.

N. Majernik, S. Barber, et. al. Optimization of Low Aspect Ratio, Iron Dominated Dipole Magnets. *Physical Review Accelerators and Beams*, 22(3):32401, 2019.

N. Majernik, W. Lynn, Y. Sakai, and J. Rosenzweig. Plasma Deflection Interrupter for Pulsed Power Applications. *Instruments*, 2(3):14, 2018.

N. Majernik, S. Pree, et. al. Simultaneous Ultra-Fast Imaging and Neutron Emission from a Compact Dense Plasma Focus Fusion Device. *Instruments*, pages 1-11, 2018.

N. Majernik, J. Rosenzweig, B. Naranjo, and P. Hoang. Mesoscale photonic structure fabrication. Prov. patent: US 62/648,989. 2018.

J. B. Rosenzweig, F. Filippi, et. al. Adiabatic plasma lens experiments at SPARC. *Nuclear Inst. and Methods in Physics Research, A*, 909:471-475, 2018.

Y. Sakai, I. Gadjev, et. al. Single shot, double differential spectral measurements of inverse Compton scattering in the nonlinear regime. *Physical Review Accelerators and Beams*, 20(6):1-11, 2017.

N. Majernik and S. Pree. Vacuum pumping aperture. Prov. patent: US 62/503,106. 2017.

N. Majernik. Ultrafast low jitter spark gap. Prov. patent: US 62/482,353. 2017.

N. Majernik and J. Rosenzweig. Resonant excitation of betatron oscillations. *Nuclear Inst. and Methods in Physics Research, A*, 865(October 2016):91-94, 2017.

N. Majernik and J. Rosenzweig. Method of localizing breakdown in high power RF networks. Prov. patent: US 62/449,760. 2017.

CHAPTER 1

Introduction

1.1 History of LPAs and FELs

This dissertation discusses various efforts towards the realization of a laser plasma accelerator (LPA) driven free electron laser (FEL). Although both LPAs and FELs have had at least a decade of experimental demonstration and refinement, to date, there has not yet been a demonstration of FEL gain when using an LPA driver. This section will introduce the fundamentals and history of LPAs and FELs independently and will discuss the difficulties of pairing them together.

1.1.1 Free electron lasers

The free electron laser was first described by John Madey in 1971 [1] and then demonstrated by his group in 1977 [2]. FELs use a beam of relativistic electrons as the laser gain medium, arising from their interaction with and amplification of an electromagnetic field while traveling through a periodic magnetic structure called an undulator. An idealized model of an undulator is a sinusoidally varying, vertically oriented magnetic field, $B_y = B_0 \sin(k_u z)$, where B_0 is the peak magnetic field and k_u is the undulator wavenumber. This in turn causes the electrons to follow a perpendicular, sinusoidal trajectory.

An accelerated charged particle emits synchrotron radiation which, in the context of a constant magnetic field, is broadband and swept out tangentially along the bend. However, in an undulator, the radiation from the individual bends interferes with each other, tightening the emitted radiation into a forward directed cone and narrowing the emitted spectrum into spikes at harmonics of the fundamental wavelength, λ_r. For a trajectory with a small oscillation amplitude, $\lambda_r \approx \frac{\lambda_u}{2\gamma_0^2}$, where λ_u is the undulator wavelength and γ_0 is the Lorentz factor. Intuitively, this situation can be thought of as relativistic Doppler blueshifting the output of a moving antenna, i.e. the moving electrons.

In a free electron laser though, there is an additional term in the electron equation of motion: an external electromagnetic field. If this field is at or near the undulator's fundamental wavelength, it can cause the electrons to microbunch at that wavelength (This process is discussed in much greater detail in Section 4.2.1). As the electrons microbunch, the length of the effective emitter begins to become small relative to the radiation wavelength, meaning that the synchrotron radiation from each individual electron adds at nearly the same phase as all the others. This coherence leads to a the generation of radiation with intensity scaling with the number of electrons squared, instead of linearly as in spontaneous undulator radiation. For bunches with billions of electrons, the coherent enhancement of power can be many orders of magnitude.

Broadly speaking, there are three classes of FEL [3]: oscillator, seeded, and self-amplified spontaneous emission (SASE). The earliest demonstrated examples of the FEL were oscillators which operate like a typical laser cavity resonator; two mirrors reflect light back and forth through a cavity containing the gain medium, which in this case is the electron beam passing through an undulator. Such devices operate in the "low gain" regime where the increase in power per pass is small. High powers can still be reached by relying on many passes through the medium, but it is necessary to have mirrors available for the relevant wavelength, largely limiting them to wavelengths at and above UV. A seeded FEL does not require mirrors and operates in a single pass, where a pulse of radiation at the resonant wavelength is copropagated with the electron beam through the undulator. This approach extends the FEL's operation to regions of the spectrum without high quality mirrors but instead requires another source of the target radiation wavelength; this largely confines seeded FELs to use at deep UV wavelengths. Finally, a SASE FEL relies on a resonant self-interaction with the spontaneous undulator radiation as it slips forward along the subluminal electron beam. This is currently the only class of FEL which can access hard x-ray wavelengths. The issue with such FELs is the stringent requirements on beam quality (Discussed in greater detail in Chapter 4).

The SASE x-ray free electron laser (XFEL) is currently the brightest source of x-rays available, more than 10 orders of magnitude brighter than the next brightest: spontaneous undulator radiation [4]. The ultrashort (∼fs) pulses deliver gigawatts of power to spot sizes on the order of 100 nm, making them an invaluable research tool for biology, chemistry, material science, medicine, and more by allowing researchers to probe length and time scales that would otherwise be inaccessible [5]. The main issue with XFELs is their enormous price tag; costing on the order of a billion dollars each, there are only around a half dozen XFELs, all of them constructed by nation states or supra-national organizations. The invaluable science they can generate paired with the limited access to beamtime means these facilities are massively oversubscribed, to the detriment of scientific and technological progress.

All current XFELs are comprised of an rf linac and a conventional undulator and have a footprint on the order of kilometers. rf linacs can be either normally conducting or superconducting but, in either case, consist of precisely formed metal cavities which are pumped with microwaves which create longitudinal electric fields to accelerate electrons. The linac usually has a final energy of around 10 GeV and, since rf structures are limited by breakdown to a gradient of a few 10s of MV/m, they are necessarily extremely long and therefore extremely expensive. The beam is then delivered to a conventional undulator, comprised either of a pure permanent magnet or hybrid Halbach array, with a length on the order of 100 meters. This is also a very precise, long, and therefore expensive device. To dramatically increase access to beamtime, research into improving both the acceleration and undulator sections of the XFEL are extremely active in an effort to reduce their size and cost.

1.1.2 Laser plasma accelerators

The laser plasma accelerator (LPA) is a compact alternative to the rf linac for electron acceleration, wherein a high intensity laser causes a ponderomotive ejection of plasma electrons, leaving behind a high charge ion channel with extremely large accelerating gradients. The LPA was first described theoretically in 1979 by Tajima and Dawson [6] but advancements in ultra-intense, ultra-short lasers enabled by chirped pulse amplification were required for experimental realization in the “bubble regime”. Early experiments, e.g. Malka et. al in 2002 [7], generated beams with exponential energy distributions, with spreads in excess of 100% with peak energies around 200 MeV. In 2004, three groups [8, 9, 10] reported a significant improvement in energy spread, to the few-% level, while still operating at <200 MeV. Since then, refinements in the LPA process have continued, producing beams in a variety of operational regimes including energies up to 8 GeV [11], currents over 10 kA [12], normalized transverse emittances below 60 nm-rad [13], and sub-% energy spreads [13, 14].

A crucial advantage of the LPA over a conventional rf linac is the enormously higher accelerating gradient, 10s to 100s of GV/m, compared to a linac’s 10s of MV/m. This allows LPAs to be three orders of magnitude shorter than a linac while producing the same final energy, potentially reducing the footprint of an accelerator from kilometers to a tabletop. Generally though, there is a trade-off between beam parameters. Although an individual LPA experiment might deliver high energy, high current, low emittance, or (relatively) low energy spread, no group has demonstrated an LPA which can achieve all these results simultaneously, in the manner that a modern linac can. This leads to the challenges associated with using an LPA to drive an FEL, as detailed in the next section.

1.1.3 LPA driven FEL

As LPA beam quality has continued to improve since 2002, it was natural to propose to use an LPA as an FEL driver. If successful, such an LPA-FEL could radically decrease the size and cost of an FEL installation from a billion dollars to tens of millions and from kilometers to the lab scale. This would increase access to FEL beamtime by making them affordable to universities and companies. Considering the scientific importance of the FEL to many disciplines and the oversubscription of present FEL beamlines, the LPA-FEL could become an essential piece of research infrastructure with far ranging benefits.

At the present time however, experimentally demonstrated LPA beams do not meet the stringent beam quality requirements for direct-drive XFEL operation using a conventional undulator; the most troublesome parameter is the relatively high energy spread of LPA beams (See section 4.2.2 for details). However, beam quality has advanced to the point where it is theoretically possible to skirt these constraints using a non-traditional undulator or beam manipulation techniques.

All of the LPA-FEL experiments currently being attempted are using either a transverse gradient undulator (TGU) [3, 15, 16, 17] or beam decompression [18, 19, 20, 21]. For the TGU approach, beam optics are used to introduce a correlation between transverse position and particle energy before passing the beam through an undulator which has a non-constant undulator parameter across its width; by matching these correlations, a resonant condition can be maintained for the whole beam despite its large energy spread. The decompression approach, employed by the BELLA FEL project, uses a chicane to decompress the beam, reducing the current but also reducing the slice-wise energy spread to an acceptable level for lasing. Neither approach has yet demonstrated FEL gain but work is ongoing. An additional option for an LPA-FEL is also considered in this dissertation: the use of advanced undulators for a direct drive LPA-FEL. Through the use of non-conventional undulator design, it is possible to increase the FEL's tolerance to energy spread.

1.2 Dissertation structure

This dissertation discusses two experimental subsystems designed and built for the BELLA FEL experiment at Lawrence Berkeley National Lab (LBNL): a coherent transition radiation bunch length diagnostic and the beam decompression chicane. The final chapter explores direct drive LPA-FELs based on advanced undulators using simulations and also details approaches for constructing such advanced undulators.

Chapter 2 is about the design, simulation, construction, and commissioning of a coherent transition radiation (CTR) based bunch length diagnostic for the BELLA FEL experiment. It begins with a discussion on the theory of transition radiation and a subsequent derivation of coherent transition radiation with an explanation of how it can be used to understand the temporal structure of a beam. Next it discusses the particular constraints imposed by the

BELLA FEL experiment for the diagnostic system. The custom simulation framework for the optical system is described and used to determine the layout. Simulated detector responses as a function of beam specs are demonstrated. The commissioning of the system using a blackbody source and spectrum reconstruction are discussed. Details regarding installation and alignment are also included. Finally, preliminary electron beam results are considered.

Chapter 3 is about the design, simulation, construction, and commissioning of a chicane for beam decompression for the BELLA FEL experiment. It begins with a discussion about the need for such a decompression scheme. Then fundamentals of chicane dynamics are described theoretically. The next section is an adapted paper which describes the optimization of low aspect ratio dipole magnets, a class of magnet likely to be relevant for future LPA experiments. Next, the requirements imposed on the design of the chicane specifically for the BELLA FEL experiment are enumerated. There are discussions on pole face design, magnetic circuit analysis, coil design, thermal considerations, material selection and properties, mechanical considerations, and the evolution of the dipole design. Details about the fabrication of the dipoles and the chicane kinematic mount are included. Measurements of the field using a Hall probe and 3D gantry are described and compared to a simulated model. The chapter concludes with notes about the degaussing procedure and process as well as the final installation of the chicane at LBNL.

Chapter 4 is about direct drive LPA-FELs using advanced undulators. It opens with a discussion of the fundamentals of FEL operation, explaining the basic principles of high gain FEL operation in the 1D approximation. Then 3D errors and an empirical fitting model for estimating their detrimental effects are explained. The current experimental efforts towards realizing LPA-FEL, the transverse gradient undulator and beam decompression, are described along with their pros and cons. The general concept of advanced undulators are introduced and contrasted with the conventional undulators in use at all extant XFELs. Two specific classes of advanced undulators, cryo-undulators and milliundulators, are considered in more detail. Next, time dependent simulations incorporating all 3D effects are performed, pairing advanced undulators with three different cases of LPAs beams to explore the potential of a direct drive LPA-FEL. These three cases are the BELLA FEL experiment beam (both a conservative case and a proposed upgrade), the best experimentally demonstrated LPA beam to date, and a particle-in-cell simulated LPA beam. Finally, the chapter closes with sections about the construction of future advanced undulators. One of these approaches is an adapted paper describing the use of right angle, triangular magnets in a pure permanent magnet Halbach array. The other approach is adapted from another paper about the use of "comb fabrication" to construct higher order Halbach and hybrid Halbach milliundulators.

CHAPTER 2

Coherent transition radiation bunch length diagnostic

2.1 Coherent transition radiation introduction

2.1.1 Motivation

Measuring the temporal profile of an electron bunch is a crucial diagnostic for free electron lasers. This is especially true for the BELLA FEL experiment since, combined with a chicane and spectrometer, a bunch profile diagnostic will give information about the beam decompression. Unfortunately, many of the diagnostic techniques developed over the past decades for rf linacs and their few picosecond long beams (e.g. electro-optic methods, streak cameras, and rf and passive deflectors [22, 23, 24]) are unable to resolve the ultra-short, few femtosecond, bunches that laser plasma accelerators produce. Techniques for measuring these beams are an area of active development and there is not yet a *de facto* standard [24]. Based on the requirements for this experiment of single shot measurement and resolution of a wide range of bunch lengths with limited prior knowledge and the desire to use an already-possessed pyroelectric detector, the implementation of a coherent transition radiation (CTR) bunch length diagnostic was requested.

2.1.2 Transition radiation fundamentals

To discuss the operating principle of a CTR bunch length diagnostic, it is necessary to first establish the physics of transition radiation (TR) in general. First predicted theoretically by Ginzburg and Frank in 1946 [25], transition radiation is often described as a particle "shaking off" the field discontinuities that result from traversing the interface between two media with different permittivities. The derivation from first principles is lengthy but straightforward and can be found in standard EM textbooks like [26]. An expression for the forward transition radiation spectral power density for an electron traversing such a discontinuity, normal to the interface, is given by [27] as (in Gaussian units):

$$\frac{\mathrm{d}^2 I(\mathbf{n},\omega)}{\mathrm{d}\omega\,\mathrm{d}\Omega} = \frac{e^2\beta^2\sqrt{\epsilon_2}\sin^2\theta_2}{\pi^2 c\,(1-\beta^2\epsilon_2\cos^2\theta_2)^2}\left|\frac{\cos(\theta_2)(\epsilon_1-\epsilon_2)\left(1-\beta^2\epsilon_2-\beta\sqrt{\epsilon_1-\epsilon_2\sin^2\theta_2}\right)}{\left(1-\beta\sqrt{\epsilon_1-\epsilon_2\sin^2\theta_2}\right)\left(\epsilon_1\cos\theta_2+\sqrt{\epsilon_1\epsilon_2-\epsilon_2^2\sin^2\theta_2}\right)}\right|^2 \tag{2.1}$$

where $\frac{\mathrm{d}I(\mathbf{n},\omega)}{\mathrm{d}\omega\,\mathrm{d}\Omega}$ is the energy radiated along vector $\mathbf{n}$ at frequency ω per unit frequency per unit solid angle, Ω, e is the electron charge, ϵ_1 and ϵ_2 are the permittivities of the initial and final media respectively, θ_2 is the angle between the measurement vector $\mathbf{n}$ and the beam axis, c is the speed of light, and β is the particle velocity normalized to c. Note that the frequency response is flat, i.e. there is no ω dependence, corresponding to an impulse response in the time domain.

For the case of an electron traveling through a media into vacuum, set ϵ_2 to 1. Then consider the second part of the expression in the ultra-relativistic limit ($\beta \to 1$), in the first order approximation for small θ_2:

$$\lim_{\beta\to 1}\left|\frac{\cos(\theta_2)(\epsilon_1-\epsilon_2)\left(1-\beta^2\epsilon_2-\beta\sqrt{\epsilon_1-\epsilon_2\sin^2\theta_2}\right)}{\left(1-\beta\sqrt{\epsilon_1-\epsilon_2\sin^2\theta_2}\right)\left(\epsilon_1\cos\theta_2+\sqrt{\epsilon_1\epsilon_2-\epsilon_2^2\sin^2\theta_2}\right)}\right|^2 = 1+\mathcal{O}(\theta_2^2). \tag{2.2}$$

So in this limit

$$\frac{\mathrm{d}^2 I(\mathbf{n},\omega)}{\mathrm{d}\omega\,\mathrm{d}\Omega} \approx \frac{e^2\beta^2\sin^2\theta_2}{\pi^2 c\,(1-\beta^2\cos^2\theta_2)^2}, \tag{2.3}$$

and the dependance on the media's permittivity, ϵ_1, drops out. Convert to SI units by the substitution $e^2 \mapsto \frac{e^2}{4\pi\epsilon_0}$:

$$\frac{\mathrm{d}^2 I(\mathbf{n},\omega)}{\mathrm{d}\omega\,\mathrm{d}\Omega} \approx \frac{e^2\beta^2\sin^2\theta_2}{4\pi^3 c\epsilon_0\,(1-\beta^2\cos^2\theta_2)^2}, \tag{2.4}$$

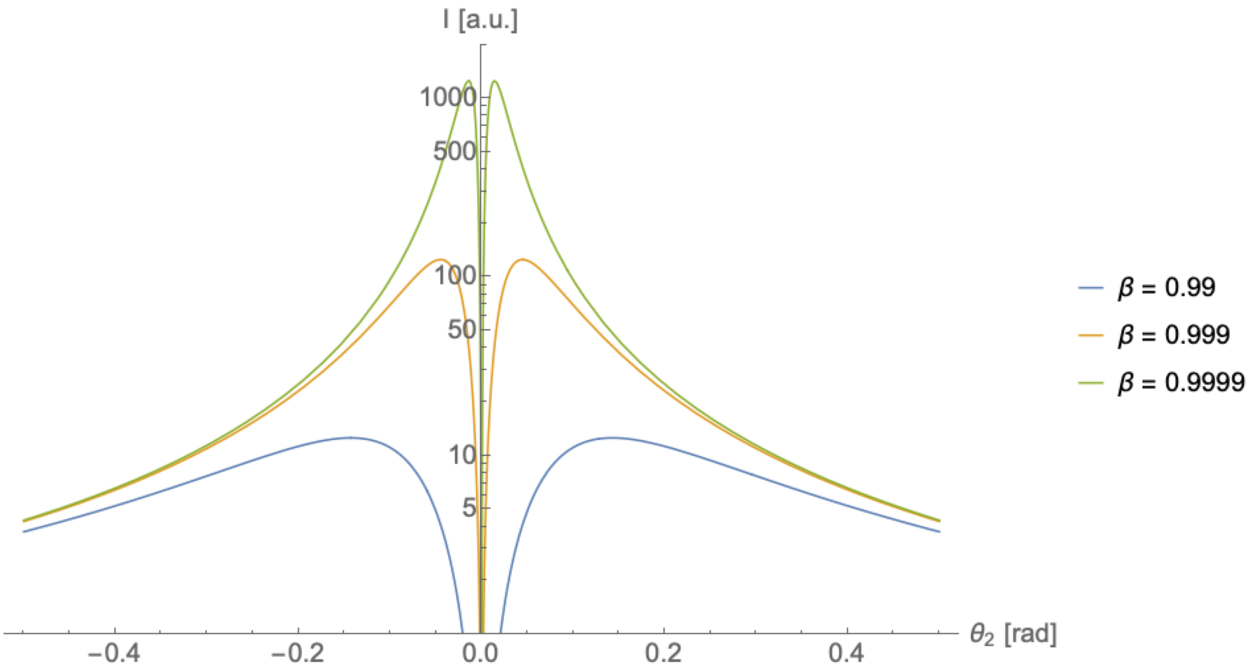

Figure 2.1: Angular and β dependence of transition radiation.

which is a standard expression for TR (e.g. [28]). Figure 2.1 shows the angular dependence of this expression for a few β values.

Taking the derivative of equation 2.4 with respect to θ leads to an expression for the angle corresponding to maximum energy emission, θ_m:

$$\theta_m = \tan^{-1}\left(\sqrt{\frac{1-\beta^2}{2\beta^2-1}}\right). \tag{2.5}$$

Using the standard Lorentz factor, $\gamma = \frac{1}{\sqrt{1-\beta^2}}$, substitute into equation 2.5:

$$\theta_m = \cot^{-1}\sqrt{\gamma^2-2}, \tag{2.6}$$

which to first order in large γ reduces to:

$$\theta_m \approx 1/\gamma. \tag{2.7}$$

Plugging this back into equation 2.4 to find the peak intensity yields:

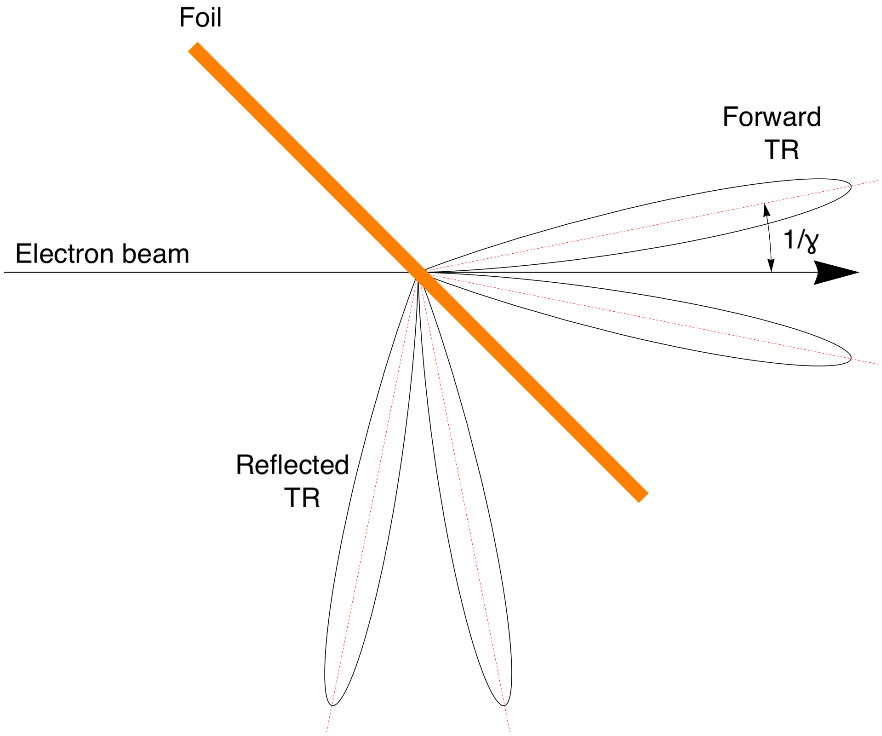

Figure 2.2: Schematic of the distribution of transition radiation.

$$\left.\frac{\mathrm{d}^2 I(\mathbf{n},\omega)}{\mathrm{d}\omega\,\mathrm{d}\Omega}\right|_{\max} \approx \frac{\gamma^2}{4}, \tag{2.8}$$

A schematic of the distribution of transition radiation is shown in Figure 2.2; a similar process for calculating TR resulting from a particle transiting from vacuum to non-vacuum yields “reflected transition radiation” of the same form.

2.1.3 Coherent transition radiation fundamentals

Although the transition radiation of a single particle has a flat frequency response, a bunch will have a non-flat response based on the coherent and incoherent addition of the respective particles’ TR. A derivation of CTR from an electron bunch can be found in many sources including [29]. The derivation begins by taking a linear superposition of all of the TR electric fields from each electron:

$$\mathbf{E}_{\text{total}}(\omega) = \sum_{j}^{N} \mathbf{E}_j(\omega) e^{i(\omega t - k\mathbf{n}_j \cdot \mathbf{r}_j)}, \tag{2.9}$$

where this is a sum over the N bunch electrons, $\mathbf{n}$ is a normalized vector pointing from the j^{th} electron to the observer, and k is the wavenumber ω/c. The intensity is proportional to the electric field squared:

$$I(\omega) \propto \left| \sum_{j}^{N} \mathbf{E}_j(\omega) e^{i(\omega t - k\mathbf{n}_j \cdot \mathbf{r}_j)} \right|^2, \tag{2.10}$$

which can be expressed as a product of sums running over different indices using a complex conjugate to enforce the absolute value:

$$I(\omega) \propto \sum_{j}^{N} E_j(\omega) e^{i(\omega t - k\mathbf{n}_j \cdot \mathbf{r}_j)} \sum_{m}^{N} E_m^*(\omega) e^{-i(\omega t - k\mathbf{n}_m \cdot \mathbf{r}_m)}, \tag{2.11}$$

with $E = |\mathbf{E}|$. This can be reexpressed in the suggestive form:

$$I(\omega) = \sum_{j}^{N} |E_j(\omega)|^2 + \sum_{j,m;\, j \neq m}^{N} E_j(\omega) E_m^*(\omega) e^{ik\mathbf{n} \cdot (\mathbf{r}_j - \mathbf{r}_m)}. \tag{2.12}$$

The total intensity can be found in absolute rather than proportional terms by substituting in the intensity from a single electron, i.e. $|E_j(\omega)|^2 \propto I_e(\omega)$. If all the electrons can be taken to have approximately the same energy, then the same replacement can be made between electron field contributions, i.e. $E_j(\omega)E_m^*(\omega) = I_e(\omega)\ \forall j, m$. Then equation 2.12 simplifies to:

$$I(\omega) = N I_e(\omega) + I_e(\omega) \sum_{j,m;\, j \neq m}^{N} e^{ik\mathbf{n} \cdot (\mathbf{r}_j - \mathbf{r}_m)}, \tag{2.13}$$

where the first term is the incoherent contribution, I_{incoh}, and the second term is the coherent contribution, I_{coh}. In the limit that $k\mathbf{n} \cdot (\mathbf{r}_j - \mathbf{r}_m) \to 0\ \forall j, m$ then $I_{\text{coh}} \to N(N-1)I_e(\omega)$ and, if it is also true that N is large, $I_{\text{coh}} \approx N^2 I_e(\omega) >> N I_e(\omega) = I_{\text{incoh}}$. Qualitatively, this means approximately that wavelengths which are long relative to the bunch's size will be generated coherently and will therefore have more spectral power than if the bunch was long relative to the wavelength.

If N is large, a continuum approximation can be made, permitting the use of integrals rather than sums. Let $S(\mathbf{r})$ be the normalized distribution function for the bunch such that $\int_{\mathbb{R}^3} S(\mathbf{r})\mathrm{d}^3r = 1$. Then equation 2.10 can be converted to

$$I(\omega) \propto \left| \int_{\mathbb{R}^3} NE(\omega)e^{ik\mathbf{n}\cdot\mathbf{r}}S(\mathbf{r})\mathrm{d}^3r \right|^2 . \tag{2.14}$$

As before, getting the intensity as an absolute rather than proportional expression by substituting a single electron intensity:

$$I(\omega) = N^2 I_e(\omega) \left| \int_{\mathbb{R}^3} e^{ik\mathbf{n}\cdot\mathbf{r}}S(\mathbf{r})\mathrm{d}^3r \right|^2 , \tag{2.15}$$

which can be simplified by defining the squared Fourier transform of $S(\mathbf{r})$ as the *form function*

$$f(\omega) \equiv \left| \int_{\mathbb{R}^3} e^{ik\mathbf{n}\cdot\mathbf{r}}S(\mathbf{r})\mathrm{d}^3r \right|^2 , \tag{2.16}$$

giving

$$I(\omega) = N^2 I_e(\omega) f(\omega). \tag{2.17}$$

This is the fully general expression for CTR but, for many relevant cases, making a few further assumptions can simplify the expression. The first assumption is that the bunch distribution function is separable in cylindrical coordinates: $S(\mathbf{r}) = S_z(z)S_\perp(\rho, \phi)$. With θ taken to be the angle between the z-axis and $\mathbf{n}$, $\mathbf{n}\cdot\mathbf{z} = z\cos\theta$ and $\mathbf{n}\cdot\mathbf{r}_\perp = r_\perp \sin\theta$, and with ϕ defined as the angle between ρ's projection onto the xy-plane and the x-axis equation 2.16 becomes:

$$f(\omega, \theta) = \left| \int_0^\infty \int_0^{2\pi} S_\perp(\rho, \phi)e^{ik\rho\cos\phi\sin\theta}\mathrm{d}\phi\,\mathrm{d}\rho \int_{-\infty}^{\infty} S_z(z)e^{ikz\cos\theta}\mathrm{d}z \right|^2 . \tag{2.18}$$

By further assuming that the bunch distribution is cylindrically symmetrical, i.e. $S_\perp(\rho,\phi) = S_\perp(\rho)$, then

$$f(\omega,\theta) = \left| \int_0^\infty S_\perp(\rho) \int_0^{2\pi} e^{ik\rho\cos\phi\sin\theta}\mathrm{d}\phi\, \mathrm{d}\rho \int_{-\infty}^{\infty} S_z(z) e^{ikz\cos\theta}\mathrm{d}z \right|^2, \tag{2.19}$$

and the identify for a zeroth order Bessel function,

$$2\pi J_0(u) \equiv \int_0^{2\pi} e^{iu\cos\phi}\mathrm{d}\phi \tag{2.20}$$

gives

$$f(\omega,\theta) = 4\pi^2 \left| \int_0^\infty S_\perp(\rho) J_0(k\rho\sin\theta)\mathrm{d}\rho \int_{-\infty}^{\infty} S_z(z) e^{ikz\cos\theta}\mathrm{d}z \right|^2. \tag{2.21}$$

For a transversely symmetric, tri-gaussian bunch, i.e. $S_\perp(\rho) = \frac{1}{\sqrt{2\pi\sigma_r^2}} e^{-\rho^2/2\sigma_r^2}$ and $S_z(z) = \frac{1}{\sqrt{2\pi\sigma_z^2}} e^{-z^2/2\sigma_z^2}$, the form factor is

$$f(\omega,\theta) \approx e^{\frac{-\omega^2}{c^2}\left(\sigma_z^2\cos^2\theta + \sigma_r^2\sin^2\theta\right)}. \tag{2.22}$$

Substituting back into equation 2.17 which gives CTR in terms of the form factor, also substituting the definition of single particle transition radiation from equation 2.4 gives:

$$\frac{\partial^2 I_{\mathrm{CTR}}}{\partial\omega\,\partial\Omega} = N^2 \frac{e^2\beta^2\sin^2\theta}{4\pi^3 c\epsilon_0 \left(1-\beta^2\cos^2\theta\right)^2} e^{\frac{-\omega^2}{c^2}\left(\sigma_z^2\cos^2\theta + \sigma_r^2\sin^2\theta\right)}, \tag{2.23}$$

the generic expression for spectrally and angularly dependent CTR for a transversely symmetric, tri-gaussian electron bunch.

Some experiments [30, 29] use a simplified version of the form factor which supposes that the effects of the transverse beam size are negligible, i.e. $\sigma_z^2\cos^2\theta >> \sigma_r^2\sin^2\theta$. Recalling that radiation is peaked at $\theta \approx 1/\gamma$ and nearly entirely contained within a few factors of $1/\gamma$, this supposition is good in the limit of large γ. This permits the form function to be reduced to

$$\lim_{\gamma\to\infty} f(\omega,\theta) \approx e^{-\left(\frac{\omega\sigma_z}{c}\right)^2}. \tag{2.24}$$

eliminating its angular dependence. However, for the CTR system discussed below, this is not a valid approximation due to the relatively low beam energy (∼100-200 MeV) and the fact that $\sigma_z < \sigma_x$.

2.2 CTR diagnostic constraints

The CTR bunch length diagnostic for the BELLA FEL experiment had a number constraints which influenced its design. These included:

- Measurement of beams ranging from 1 to 10 μm
- Single shot diagnostic
- No pre-shot beam length assumption
- Use of existing detector
- Compact layout

A detailed discussion of these requirements and their implications follows.

2.2.1 Measurement of beams ranging from 1 to 10 μm

LBNL requested the ability to resolve beams over a wide range of lengths, from 1 to 10 μm, due to the tunability of the LPA process [31]. They were confident in their ability to generate 10 μm beams initially and, by having a detection range up to that point, the accelerator parameters could be tuned to reduce the bunch length. 1 μm was taken as the feasible lower bound for this optimization process. Assuming gaussian beams at 50, 100, and 250 MeV with a 10 μm spot size, equation 2.23 integrated over θ up to $6/\gamma$ gives spectra shown in Figure 2.3. This plot shows the normalized CTR spectra for the maximum and minimum

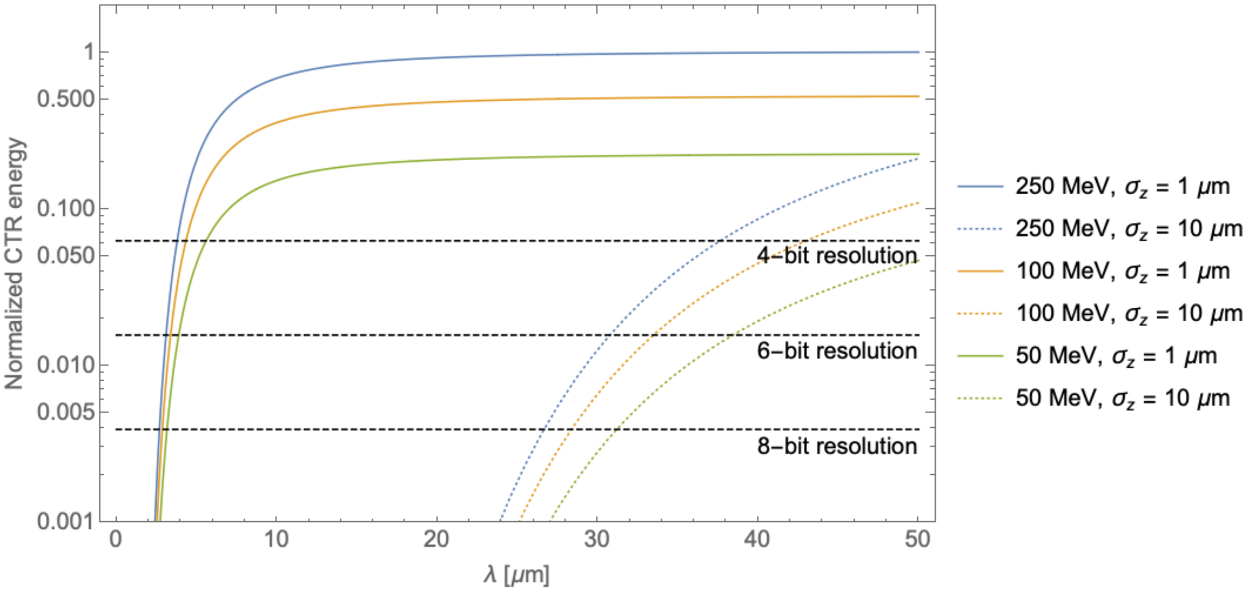

Figure 2.3: Normalized CTR spectra for the shortest (1 μm) and longest (10 μm) beams to be resolved at representative energies 50, 100, and 250 MeV. For reference, 4-, 6-, and 8-bit detection limits are shown.

length beams. Also shown is the minimum resolvable intensity based on a non-clipping, 6-bit detector (to be discussed later). Therefore, a spectral range from 1 to 40 μm was selected for the spectrometer.

2.2.2 Single shot diagnostic

The next constraint for the diagnostic system is that it needs to be single shot. Many other CTR bunch length diagnostics require either a multi-shot approach or significant pre-shot knowledge, both of which require a stable beam. Some examples of a multi-shot CTR diagnostic include interferometry [32, 33, 22] or employing discrete spectral filters on a non-dispersed CTR signal [30] while techniques that require pre-shot knowledge of the beam's structure include real-time interferometry (RTI) [34, 35] or absolute energy measurement of the whole spectrum by a single bolometer pixel [36]. Since LPA beams are highly variable shot-to-shot compared to conventional accelerators [37, 38, 39, 40, 41], it is necessary that all information required for bunch length reconstruction be available from a single shot. This requires the use of a multi-pixel detector for the spectrometer which dovetails with a later constraint.

2.2.3 No pre-shot beam length assumption

As addressed previously, a wide range of bunch lengths are expected, with potentially high variability. Without being able to reliably predict the approximate length of the beam beforehand, the use of gratings as a diffractive element was ruled out. Although gratings can have lower losses than transmissive, diffractive elements like a prism, they also can produce multiple order reflections of the dispersed spectra, which can sometimes overlap. Without prior knowledge of what the expected spectra should be, attempting to deconvolve these multiple orders could be intractable. Therefore, a prism, with its single order output, was selected as the dispersive element.

2.2.4 Use of existing detector

The design considerations above along with the nature of CTR radiation apply stringent constraints to the selection of the spectrometer detector. The detector must be:

- Broadband - sensitive at least to photons with wavelengths from 1 to 40 μm
- Sensitive - based on the energy output expected from the CTR foil and losses in the optical system, the detector needs to be able to resolve few to 10s of nJ
- Pulse compatible - the detector must be able to tolerate and integrate the extremely short pulses that the CTR interaction generates
- Multiple pixel - the detector needs a few 10s of pixels to meaningfully resolve the spectrum

A detector satisfying all of these requirements might be an expensive, potentially custom device. Fortunately, a suitable detector was available to be loaned for this experiment. This custom detector, SDX-1105 [34, 35], was produced as a collaboration between Gentec-EO

USA Inc. and Radiabeam Technologies LLC. It employs a 32 channel, pyroelectric strip sensor, comprised of 0.5 mm wide by 1 mm tall $LiTaO_3$ active elements. It has broadband sensitivity from the visible through THz regimes. Each channel has 1 nJ sensitivity with 6 bit resolution.

2.2.5 Compact layout

A vacuum chamber is dedicated to beam diagnostics on the BELLA FEL beamline. All of the CTR system needs to fit inside this chamber with approximate internal dimensions of 0.35 m × 0.35 m × 0.30 m.

2.3 CTR diagnostic design

2.3.1 Prism

Based on the design constraints, a prism with transmission from 1 to 40 μm is required. Unfortunately, very few materials satisfy this requirement as shown in Figure 2.4 (data from [42]). Some of the cesium salts are transmissive over this range but are considered very difficult to work with. For example, cesium iodide is described as "extremely difficult to polish, and so performance is compromised for range" [43]. Another material has a smaller transmissive range but covers our required spectrum: thallium bromoiodide, also called KRS-5. KRS-5 has been used in other CTR diagnostics with similar spectral requirements including [44, 45, 33]. It is still a difficult material to work with as it has the following undesirable properties [43]:

- Toxic - it is fatal in both acute and chronic exposures with a HMIS health hazard rating of 4, the maximum value
- Soft - its Knoop hardness of 40 is comparable to gypsum and more than 10 times lower than glass
- Hygroscopic - which can lead to clouding as it absorbs moisture from the air

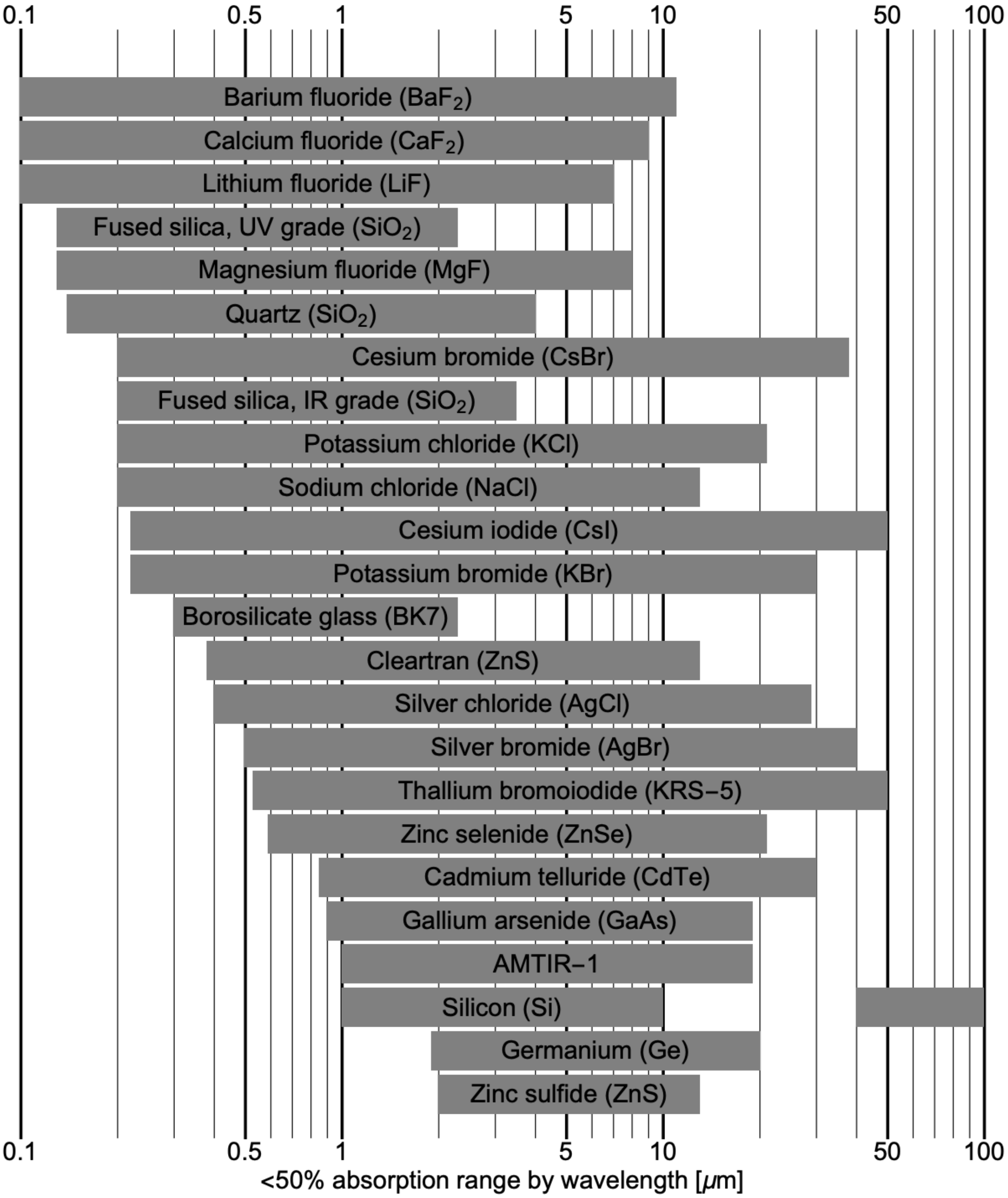

Figure 2.4: Optical material transmission ranges. Data from [42].

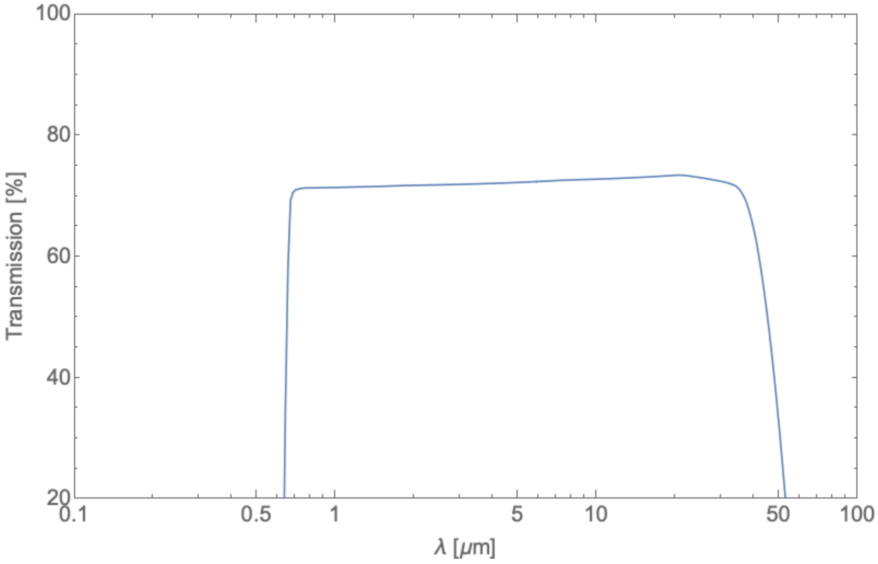

Figure 2.5: Transmission spectrum for KRS-5. Data from [46].

The transmission spectrum for KRS-5 is shown in Figure 2.5 (data from [46]). The losses in transmission are dominated by interactions at the surfaces, i.e. these curves are accurate for all KRS-5 optics of a few mm thickness, without scaling.

The vendor Crystran was engaged to produce custom KRS-5 prisms for this experiment with details discussed in section 2.3.3.4.

2.3.2 Mirror coating material

On the consumer optics market, e.g Thorlabs and Newport, there are four common, metallic, broadband coatings available for mirrors: protected aluminum, protected silver, protected gold, and unprotected gold. “Protected” in this context refers to the application of a thin layer of dielectric(s) in order to protect the soft metal and prevent tarnishing from exposure to atmosphere [47]. Uniquely among these three metals, gold will not tarnish in atmosphere so it is possible to leave the bare metal surface, though without the mechanical protection of the dielectric layer, it requires considerable care to prevent damage or deterioration of the optical qualities. Data for the reflectivity of these 4 materials for unpolarized light at a 45 degree angle of incidence (AOI), provided by Thorlabs, is shown in Figure 2.6 (data from [47]). This illustrates the superiority of unprotected gold for the relevant spectrum of 1 to

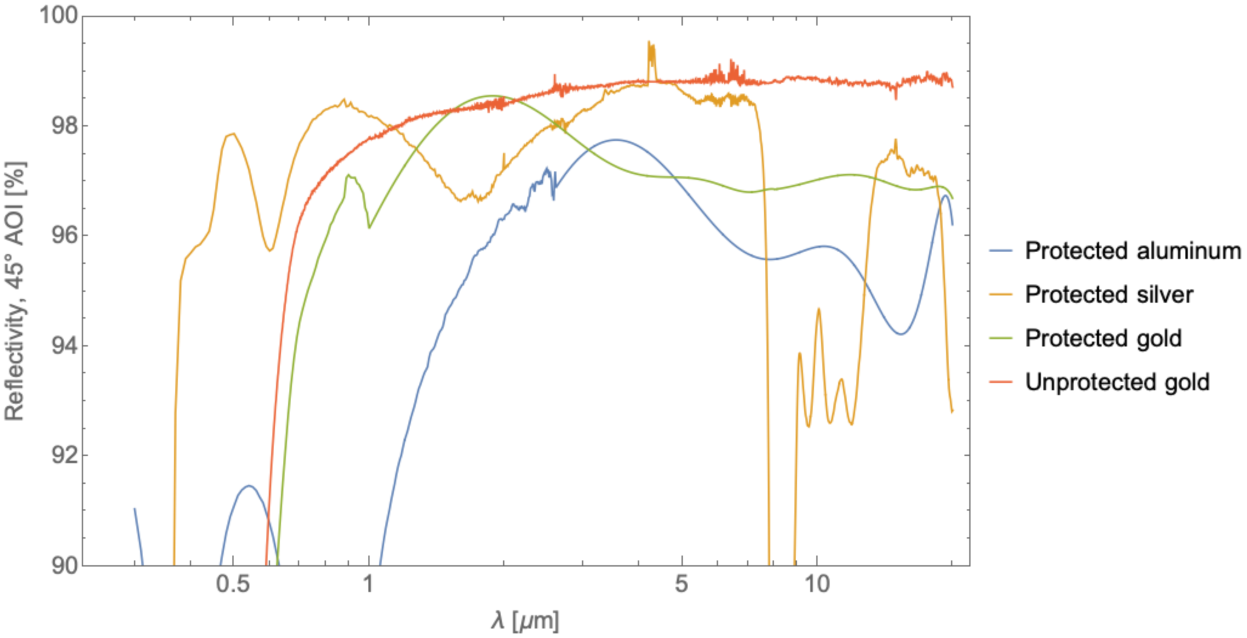

Figure 2.6: Reflectivities of four common, broadband mirror materials for unpolarized light at a 45 degree angle of incidence. Data from [47].

40 μm.

2.3.3 Optical layout

Early designs of the CTR system's optical layout included three off-axis parabolic mirrors (OAP) to create an additional focus which could employ a spatial filter as in [44, 45]. However, to reduce size and complexity, a two OAP design was selected. For initial planning purposes, the system was modeled using first order ray transfer matrices. The ray vectors include a slightly unconventional fifth term to account for the transverse angular kick induced by the prism, $\delta x'(\lambda)$, and are of the form:

$$\mathbf{r} = \begin{pmatrix} x \\ x' \\ y \\ y' \\ \delta x'(\lambda) \end{pmatrix}. \tag{2.25}$$

Three classes of optical elements are also are described in matrix form: thin lenses, drifts, and prisms:

$$\mathbf{M}_{\text{thin lens}}(f) = \mathbf{M}_{\text{L}}(f) \equiv \begin{pmatrix} 1 & 0 & 0 & 0 & 0 \\ -1/f & 1 & 0 & 0 & 0 \\ 0 & 0 & 1 & 0 & 0 \\ 0 & 0 & -1/f & 1 & 0 \\ 0 & 0 & 0 & 0 & 1 \end{pmatrix}, \tag{2.26}$$

$$\mathbf{M}_{\text{drift}}(d) = \mathbf{M}_{\text{D}}(d) \equiv \begin{pmatrix} 1 & d & 0 & 0 & 0 \\ 0 & 1 & 0 & 0 & 0 \\ 0 & 0 & 1 & d & 0 \\ 0 & 0 & 0 & 1 & 0 \\ 0 & 0 & 0 & 0 & 1 \end{pmatrix}, \tag{2.27}$$

$$\mathbf{M}_{\text{prism}} = \mathbf{M}_{\text{P}} \equiv \begin{pmatrix} 1 & 0 & 0 & 0 & 0 \\ 0 & 1 & 0 & 0 & 1 \\ 0 & 0 & 1 & 0 & 0 \\ 0 & 0 & 0 & 1 & 0 \\ 0 & 0 & 0 & 0 & 1 \end{pmatrix}, \tag{2.28}$$

where f is the focal length of the lens and d is the length of the drift. The overall system can be characterized by the matrix:

$$\mathbf{M}_{\text{system}} = \mathbf{M}_{\text{D}}(d_{\text{M2}-\text{D}})\mathbf{M}_{\text{L}}(f_{\text{M2}})\mathbf{M}_{\text{D}}(d_{\text{P}-\text{M2}})\mathbf{M}_{\text{P}}\mathbf{M}_{\text{D}}(d_{\text{M1}-\text{P}})\mathbf{M}_{\text{L}}(f_{\text{M1}})\mathbf{M}_{\text{D}}(d_{\text{S}-\text{M1}}), \tag{2.29}$$

where $d_{\text{X}-\text{Y}}$ denotes the distance between elements X and Y, f_{X} is the focal length of element X, and the subscripts S, D, M1, and M2 refer to the source, detector, first OAP, and second OAP respectively.

Three additional conditions were desirable for the design of the system. First, that the rays be collimated at the prism face to minimize the complications of non-normal incidences.

Second, that the system disperse the relevant spectrum across the full pyroelectric sensor area with position dictated exclusively by photon energy to the extent possible. And finally that all of the optics, aside from the prism, be off the shelf components. This final requirement severely constrains the design of the system (see section 2.3.2).

2.3.3.1 Requirement - collimated at prism face

Since the expected CTR source is small (few μm) compared to its divergence ($\sim 1/\gamma \approx 3 \times 10^{-3}$ rad) it can be reasonably approximated as a point source for the purposes of rough optical layout. The first condition described above, that the radiation be collimated when incident on the prism, is encapsulated in the ray transport through the first few elements:

$$\mathbf{r}_{\text{at prism face}} = \mathbf{M}_{\mathrm{D}}(d_{\mathrm{M1-P}})\mathbf{M}_{\mathrm{L}}(f_{\mathrm{M1}})\mathbf{M}_{\mathrm{D}}(d_{\mathrm{S-M1}})\mathbf{r}_{\text{source}}. \tag{2.30}$$

The point source approximation means that the source rays are of the form:

$$\mathbf{r}_{\text{source}} = \begin{pmatrix} 0 \\ x' \\ 0 \\ y' \\ \delta x'(\lambda) \end{pmatrix}, \tag{2.31}$$

and the collimation condition is equivalent to having $\mathbf{r}_{\text{at prism face}}$ of the form:

$$\mathbf{r}_{\text{at prism face}} = \begin{pmatrix} x \\ 0 \\ y \\ 0 \\ \delta x'(\lambda) \end{pmatrix}. \tag{2.32}$$

Plugging in the definitions for the transfer matrices and equation 2.31 into the right hand side of equation 2.30 becomes:

$$\mathbf{r}_{\text{at prism face}} = \begin{pmatrix} x'\left(d_{\text{M1}-\text{P}}\left(1-\frac{d_{\text{S}-\text{M1}}}{f_{\text{M1}}}\right)+d_{\text{S}-\text{M1}}\right) \\ x'\left(1-\frac{d_{\text{S}-\text{M1}}}{f_{\text{M1}}}\right) \\ y'\left(d_{\text{M1}-\text{P}}\left(1-\frac{d_{\text{S}-\text{M1}}}{f_{\text{M1}}}\right)+d_{\text{S}-\text{M1}}\right) \\ y'\left(1-\frac{d_{\text{S}-\text{M1}}}{f_{\text{M1}}}\right) \\ \delta x'(\lambda) \end{pmatrix}, \tag{2.33}$$

so setting $d_{\text{S}-\text{M1}} = f_{\text{M1}}$ satisfies the condition of equation 2.32:

$$\mathbf{r}_{\text{at prism face}} = \begin{pmatrix} f_{\text{M1}}x' \\ 0 \\ f_{\text{M1}}y' \\ 0 \\ \delta x'(\lambda) \end{pmatrix}. \tag{2.34}$$

This is merely a rigorous approach to showing that a point source, placed at the focal length of a focusing lens, will be collimated. Equation 2.34 also defines the size of prism required; if $f_{\text{M1}} = 6" = 152.4$ mm and an acceptance of at least $6 \times 1/\gamma$ is desired (containing $> 99\%$ of CTR energy) then a prism with dimension of at least 6 mm × 6 mm is required.

2.3.3.2 Requirement - dispersed along sensor width

To maximize the spectral resolution, all the pixels of the pyroelectric sensor should be used. To achieve this, the CTR spectrum should be dispersed across the whole 16 mm width. Additionally, the position on the sensor should depend only on the photon energy in the point source approximation. And, lastly, the vertical position of the final ray should be constant. These conditions are summarized by the requirement that all rays at the detector, $\mathbf{r}_{\text{detector}}$, are of the form:

$$\mathbf{r}_{\text{detector}} = \begin{pmatrix} F(\lambda) \\ \text{any} \\ 0 \\ \text{any} \\ \delta x'(\lambda) \end{pmatrix}, \tag{2.35}$$

where $F(\lambda)$ is an arbitrary function in terms of λ and “any” denotes there is no form requirement.

Having found one constraint on the free variables, $d_{\text{S}-\text{M1}} = f_{\text{M1}}$, refer again to the full system matrix, $\mathbf{M}_{\text{system}}$, equation 2.29. Then with equation 2.31 have

$$\mathbf{r}_{\text{detector}} = \begin{pmatrix} F(\lambda) \\ \text{any} \\ 0 \\ \text{any} \\ \delta x'(\lambda) \end{pmatrix} = \mathbf{M}_{\text{system}} \begin{pmatrix} 0 \\ x' \\ 0 \\ y' \\ \delta x'(\lambda) \end{pmatrix}. \tag{2.36}$$

Then the RHS evaluates to

$$\mathbf{r}_{\text{detector}} = \begin{pmatrix} F(\lambda) \\ \text{any} \\ 0 \\ \text{any} \\ \delta x'(\lambda) \end{pmatrix} = \begin{pmatrix} -\frac{d_{\text{M2}-\text{D}}(f_{\text{M1}}x' + \delta x'(\lambda) d_{\text{P}-\text{M2}})}{f_{\text{M2}}} + f_{\text{M1}}x' + \delta x'(\lambda)(d_{\text{M2}-\text{D}} + d_{\text{P}-\text{M2}}) \\ -\frac{f_{\text{M1}}x' - \delta x'(\lambda) f_{\text{M2}} + \delta x'(\lambda) d_{\text{P}-\text{M2}}}{f_{\text{M2}}} \\ \frac{f_{\text{M1}}y'(f_{\text{M2}} - d_{\text{M2}-\text{D}})}{f_{\text{M2}}} \\ -\frac{f_{\text{M1}}y'}{f_{\text{M2}}} \\ \delta x'(\lambda) \end{pmatrix}. \tag{2.37}$$

Make the substitution $d_{\text{M2}-\text{D}} = f_{\text{M2}}$

$$\mathbf{r}_{\text{detector}} = \begin{pmatrix} F(\lambda) \\ \text{any} \\ 0 \\ \text{any} \\ \delta x'(\lambda) \end{pmatrix} = \begin{pmatrix} \delta x'(\lambda) f_{\text{M2}} \\ -\frac{f_{\text{M1}} x' - \delta x'(\lambda) f_{\text{M2}} + \delta x'(\lambda) d_{\text{P}-\text{M2}}}{f_{\text{M2}}} \\ 0 \\ -\frac{f_{\text{M1}} y'}{f_{\text{M2}}} \\ \delta x'(\lambda) \end{pmatrix}, \tag{2.38}$$

which now satisfies the required form.

To ensure the spectrum covers the detector, the prism angle (discussed in a later section), which dictates $\delta x'(\lambda)$, and f_{M2} must be selected such that:

$$\text{detector width} = 16\text{mm} = |\delta x'(\lambda_{\text{max}}) f_{\text{M2}} - \delta x'(\lambda_{\text{min}}) f_{\text{M2}}| \tag{2.39}$$

2.3.3.3 Non-point source considerations

For the previous two sections, the CTR source was treated as a point source for simplicity. While a good approximation, the CTR source actually has finite size, which impacts the analysis of the optical layout. Applying $\mathbf{M}_{\text{system}}$ to a general $\mathbf{r}_{\text{source}}$ with the substitutions from above, $d_{\text{S}-\text{M1}} = f_{\text{M1}}$ and $d_{\text{M2}-\text{D}} = f_{\text{M2}}$, yields:

$$\mathbf{r}_{\text{detector}} = \begin{pmatrix} f_{\text{M2}} \left(\delta x'(\lambda) - \frac{x}{f_{\text{M1}}} \right) \\ \frac{x d_{\text{M1}-\text{P}} - f_{\text{M1}}(-\delta x'(\lambda) f_{\text{M2}} + \delta \text{x}'(\lambda) d_{\text{P}-\text{M2}} + x) - f_{\text{M1}}^2 x' + x(d_{\text{P}-\text{M2}} - f_{\text{M2}})}{f_{\text{M1}} f_{\text{M2}}} \\ -\frac{y f_{\text{M2}}}{f_{\text{M1}}} \\ \frac{y d_{\text{M1}-\text{P}} - y(f_{\text{M1}} + f_{\text{M2}}) - f_{\text{M1}}^2 y' + d_{\text{P}-\text{M2}} y}{f_{\text{M1}} f_{\text{M2}}} \\ \delta x'(\lambda) \end{pmatrix}. \tag{2.40}$$

Looking at the first and third elements of this ray, it is evident that, to keep the horizontal position on the detector as a function of λ alone to the extent possible and to keep the vertical position on the detector a constant requires minimizing $f_{\text{M2}}/f_{\text{M1}}$. However, there are physical limitations to achieving this, namely that f_{M1} cannot be made too small since there is some unavoidable transport from the CTR source to the first OAP and that f_{M2}

cannot be made too large since the system is subject to space constraints. With this in mind, along with the very limited selection of acceptable, off the shelf OAPs, it was decided to pick $f_{\mathrm{M1}} = f_{\mathrm{M2}} = 6$". This results in an "imaging" condition, where the CTR source is effectively duplicated onto the detector face with the addition of a wavelength dependent transverse kick. Since the spot size is $\ll$ pixel size, the amount of smearing that results is small.

2.3.3.4 Prism design

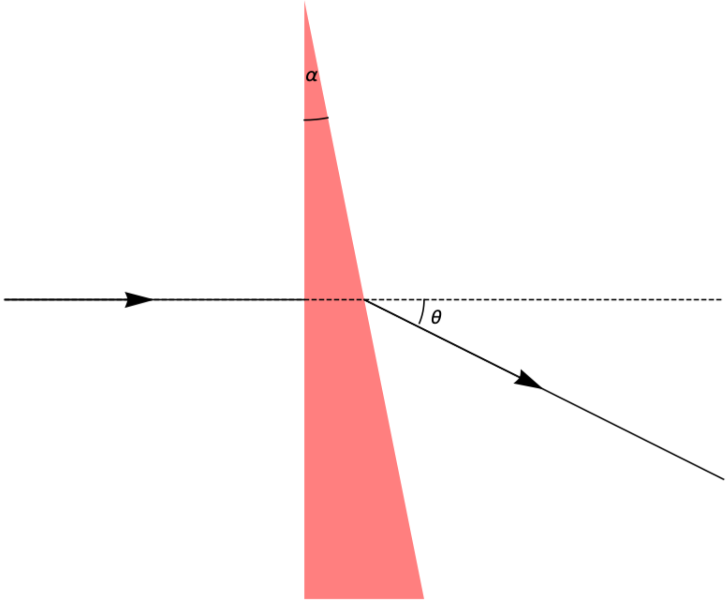

Figure 2.7: Schematic of dispersion by a prism.

With f_{M2} selected, equation 2.39 now must be solved. For a ray impinging normally on a prism in air (See Figure 2.7), with cut angle α, the deflection angle is θ, also called $\delta x'(\lambda)$, is given by [48]:

$$\theta = -\alpha + \sin^{-1}(n(\lambda)\sin(\alpha)), \tag{2.41}$$

where $n(\lambda)$ is the refractive index of the prism material for wavelength λ. The wavelength dependent refractive index for KRS-5 [49] is shown in Figure 2.8.

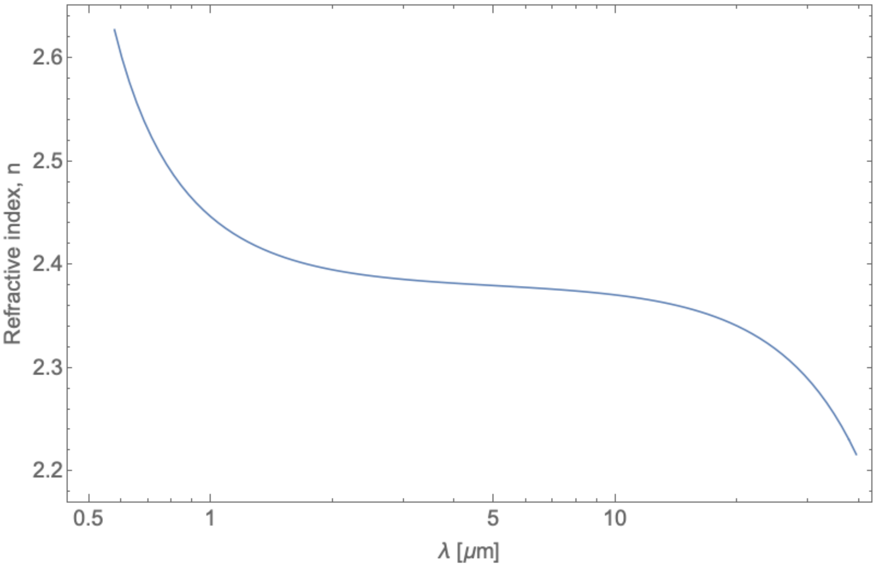

Figure 2.8: Refractive index of KRS-5. Data from [49].

At this point, all that is required is to substitute into equation 2.39 and solve numerically for α:

$$16\,\text{mm} = (152.4\,\text{mm})\left|\left(\alpha + \sin^{-1}(n(40\,\mu\text{m})\sin(\alpha))\right) - \left(\alpha + \sin^{-1}(n(1\,\mu\text{m})\sin(\alpha))\right)\right|. \quad (2.42)$$

This yields a prism angle, α, of 0.315 rad. However, the prisms were ordered based on an earlier version of the design and were cut to a slightly different α of 0.273 rad. So with this actual α and asserting that all 16 mm of detector will be used, λ_{max} becomes a function of λ_{min}, shown in Figure 2.9.

The loss of resolution from the optimal case is relatively small; now if λ_{min} is set to 1 μm, the λ_{max} is 46.6 μm instead of the target value of 40 μm. On the other hand, if λ_{max} is held at 40 μm, λ_{min} is now only 0.74 μm instead of the target value of 1 μm. The loss of resolution is not easy to characterize since the relationship between λ and horizontal position on the detector is highly non-linear. By translating the detector perpendicular to the design ray, any spectral range between these example cases can be selected. For now, suppose that the range 1 - 46.6 μm is selected. Then the first element of equation 2.38 combined with equation 2.41 yields a relationship between transverse position on the detector to photon wavelength,

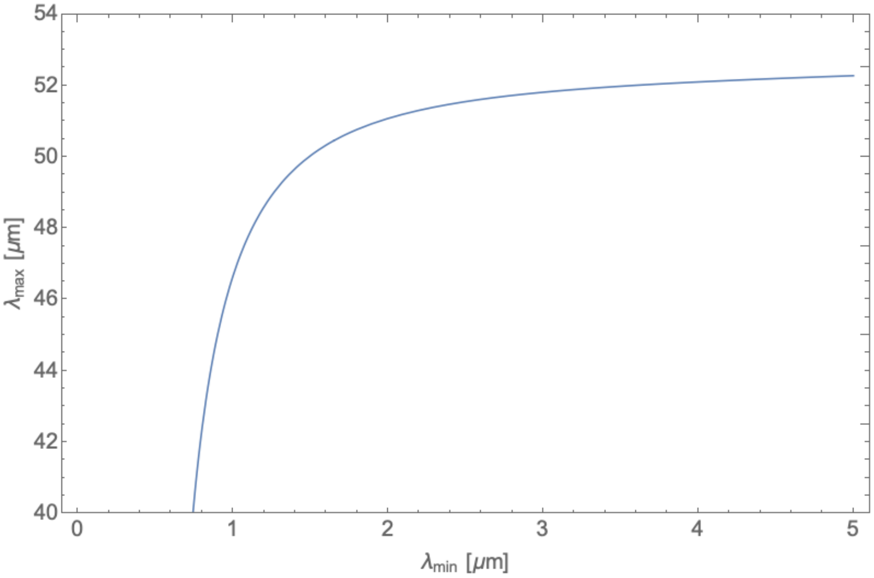

Figure 2.9: Spectrum limits over 16 mm detector using the $\alpha = 0.237$ rad prism.

shown in Figure 2.10. Note that the data has been shifted such that the detector center is at $x = 0$.

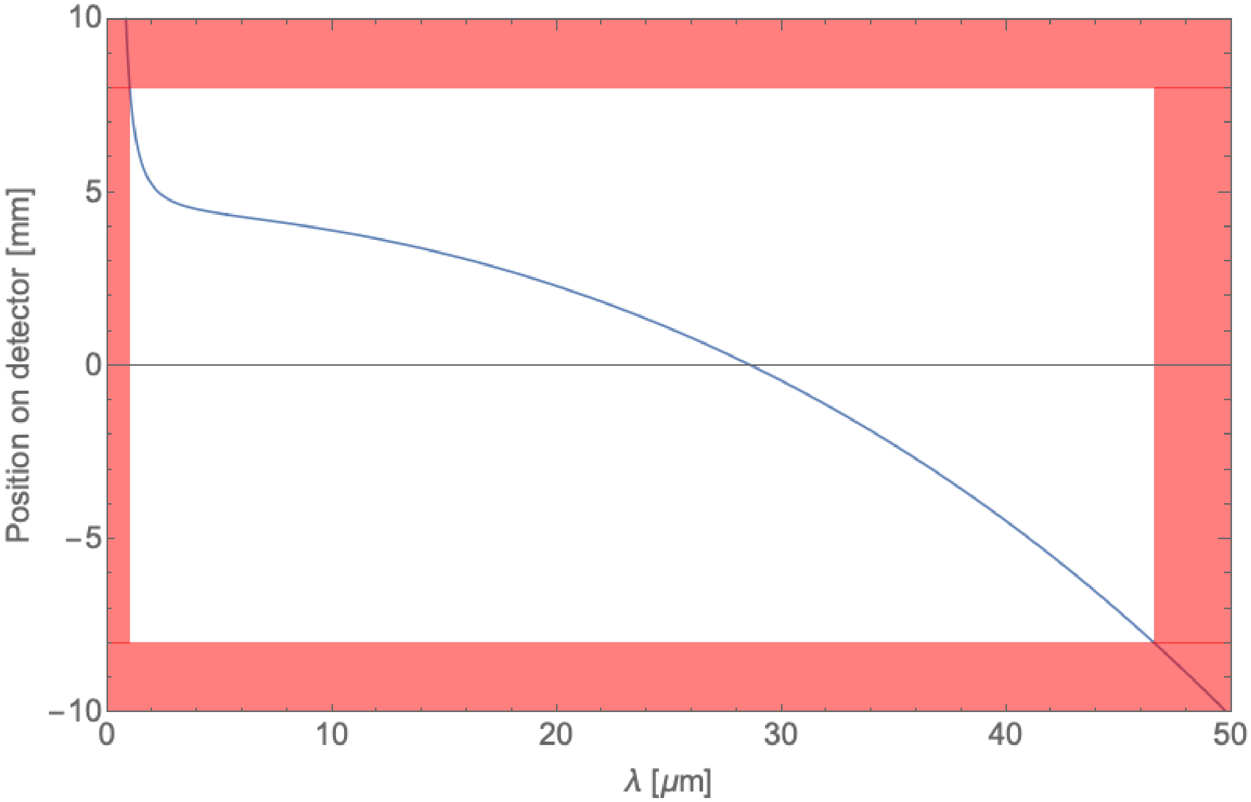

Figure 2.10: Relationship between transverse detector position and photon wavelength. Red regions are beyond the sensor and are not detectable.

Since the detector pixels are of finite width, each will be responsible for a bandwidth of photon wavelength; within this range, all photons are binned together and their wavelengths cannot be more finely resolved. Further, due to the non-linear dispersion curve, these bandwidths are not constant by pixel. These per-pixel bandwidths are shown in Figure 2.11.

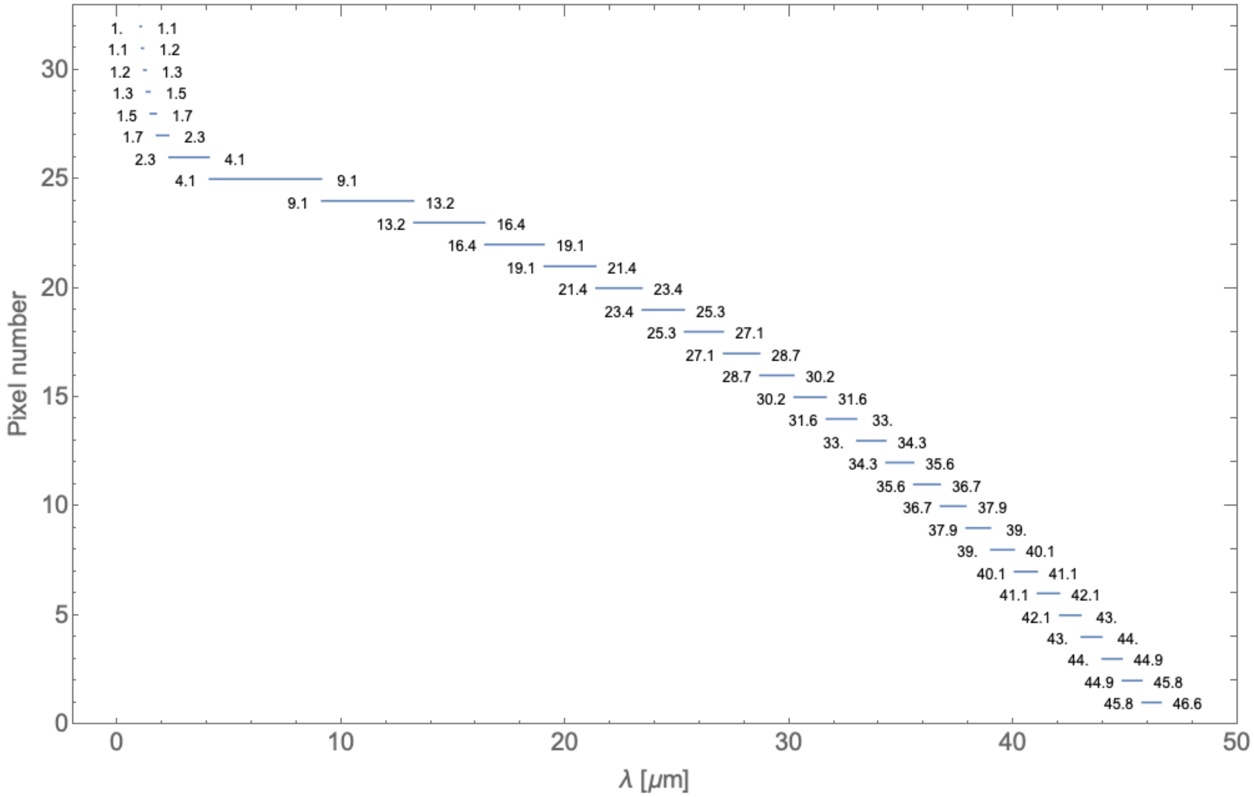

Figure 2.11: Pixel bandwidths using the $\alpha = 0.237$ rad prism and a range of 1 to 46.6 μm. The vertical position corresponds to pixel number (from 1 to 32). Each line shows the bandwidth of the pixel with longer lines indicating a higher degree of spectral smearing. The numbers on the left and right of each line are the lower and upper wavelengths binned by that pixel respectively.

2.3.3.5 Zemax validation

The optical layout was fully constrained by the first order analysis of the preceding sections. However, the system might not be sufficiently characterized at first order leading to issues with constructing and operating a real world version. The greatest concern regarded the interaction of the light, dispersed by the prism, incident on the second OAP. Since the light is no longer collimated, the OAP could have higher order effects. To validate the design, the system was simulated in Zemax OpticStudio [50] which is capable of a fully ray traced solution in 3D.

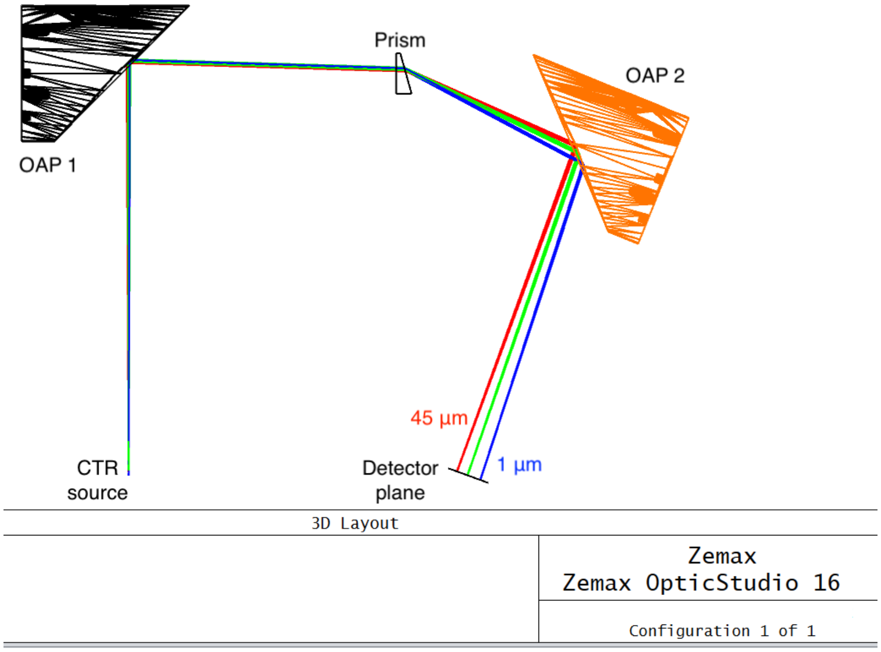

Figure 2.12: Zemax simulation of CTR system optical layout.

The prism was modeled based on the real world prism geometry and used Zemax's built in material library information for KRS-5. The OAP model files were provided by Thorlabs [47]. The Zemax layout is shown in Figure 2.12. The system's behavior was found to conform to first order approximations.

2.4 Start-to-end simulations

To understand the expected experimental outputs from the CTR system, start-to-end simulations were performed. A simulated population of CTR photons is generated, propagated, attenuated, and collected on a virtual detector.

2.4.1 Sample photon population

The first step of this simulation is to generate a sample population of CTR *macrophotons* to propagate through the optical system. Reasonable bounds should be established for the CTR wavelength and angular range as there is no reason to simulate photons that will not make it to the detector. The probability distribution function of equation 2.23 is sampled within those bounds, giving two values ω and θ for each macrophoton. Since the CTR radiation is rotationally symmetric, a random rotation angle ϕ can be picked from a uniform distribution between 0 and 2π, and produce the angular components of the ray vector according to $x' = \sin(\theta)\cos(\phi)$ and $y' = \sin(\theta)\sin(\phi)$. Then randomly sample x and y values from the bi-gaussian distribution associated with the electron beam's transverse distribution. Finally, calculate the last element of the ray vector by calculating $\delta x'(\lambda)$ using the approach of Figure 2.9.

The energy associated with each macrophoton must be normalized according to the expected, total CTR energy (equation 2.23 integrated over solid angle and photon frequency), i.e.

$$\kappa_{\text{normalization}} = \frac{\int_0^{\theta_{\max}} \int_{\lambda_{\min}}^{\lambda_{\max}} N^2 \frac{e^2\beta^2\sin^2\theta}{4\pi^3 c\epsilon_0(1-\beta^2\cos^2\theta)^2} e^{\frac{-\omega^2}{c^2}\left(\sigma_z^2\cos^2\theta+\sigma_r^2\sin^2\theta\right)} 2\pi\sin(\theta)\mathrm{d}\lambda\,\mathrm{d}\theta}{\sum\limits_i \omega_i}, \tag{2.43}$$

where i is an index associated with each macrophoton. So, for the system, a macrophoton with frequency ω is taken to have energy equal to $\kappa_{\text{normalization}}\omega$.

2.4.2 Propagation

Then, each ray vector is propagated using $\mathbf{M}_{\text{system}}$, resulting in a final ray $\mathbf{r}_{\text{detector}}$ according to equation 2.40.

2.4.3 Losses

There are transmissive and reflective losses in this system which are wavelength dependent. Although these losses do not, in reality, modulate an individual photon's energy, in aggregate the effect is equivalent to reducing the energy of a macrophoton. The transmission coefficient of KRS-5, $T_{\text{KRS}-5}(\omega)$ (Figure 2.5), and the reflectivity coefficient of unprotected gold, $R_{\text{gold}}(\omega)$ (Figure 2.6) are used. The reflectivity coefficient is applied for each gold surface; in the real world implementation there are the two OAPs but also a turning mirror which will be discussed later. Also, the pyroelectric detector has an efficiency in converting the photon energy into an electrical signal but this is hidden by the proprietary software which simply reports the incident radiant energy; from the user's perspective, the important part is knowing the minimum resolvable energy (1 nJ) [34, 35] and that it has a flat conversion efficiency over the relevant spectrum [51]. Also, since the entire optical path is in vacuum, there is no need to account for IR absorption lines from air. Therefore the detected energy of each macrophoton is taken to be:

$$E_{\text{macrophoton}}(\omega) = \kappa_{\text{normalization}} \omega T_{\text{KRS-5}}(\omega) R^3_{\text{gold}}(\omega), \tag{2.44}$$

2.4.4 Detector

The detector is represented as an array of 32 bins. For each incoming macrophoton the x and y values of $\mathbf{r}_{\text{detector}}$ are compared to the pyroelectric pixel areas and, if intersecting, the macrophoton energy is added to that pixel bin.

2.4.5 Simulation results

This method was used to simulate the detector responses to BELLA LPA beams. Figure 2.13 shows an example parametric sweep with beams with conservative values: 150 MeV, 50 pC, 100 μm spot size, for a range of bunch lengths from 1 to 10 μm.

2.5 Installation and commissioning

2.5.1 Installation

The CTR system was installed in the "diagnostics chamber" of the BELLA FEL beamline, shown in Figure 2.14. The CTR foil and a gold turning mirror are on a pneumatic pop-in, allowing remote control. Not pictured is a light shield, in the same plane as the chamber floor, which sits between the turning mirror and first OAP, providing a light-tight seal between the top and bottom of the chamber except for a single penetration in line with the CTR

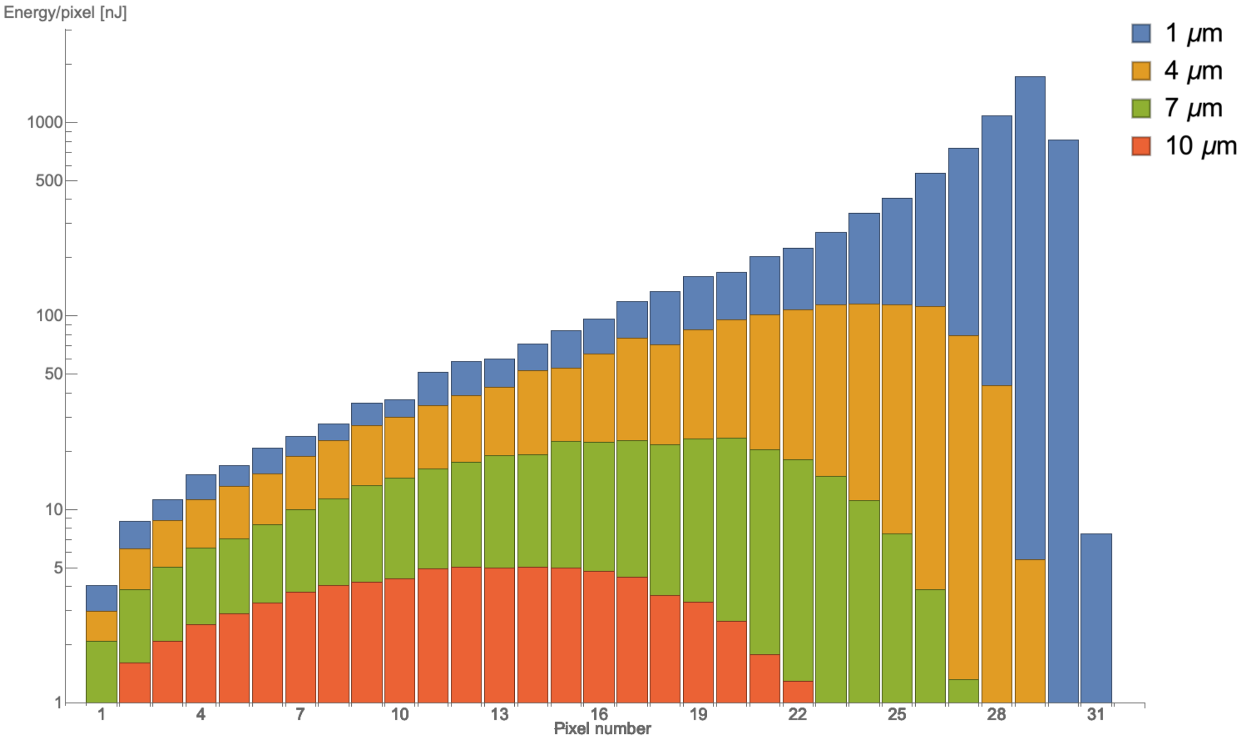

Figure 2.13: Simulated detector responses for LPA beams with specs: 150 MeV, 50 pC, 100 μm spot size with σ_z values of 1, 4, 7, and 10 μm.

path. Shielding the detector from extraneous light from the LPA drive laser and plasma fluorescence upstream is very important; there are 10s of joules of light from these sources, approximately 10 orders of magnitude more than expected from CTR. This is in part why a foil is used, rather than using the turning mirror directly as the CTR emitter. Also, since the diagnostic chamber has a dedicated vacuum pump, the upstream pipe of the chamber is almost completely covered with aluminum foil to further limit light leakage.

2.5.2 Alignment

For the initial installation of the system, a custom mount for a single mode optical fiber was designed to hold the fiber tip at the center of where the CTR foil will be. The fiber tip has a diameter of approximately 5 μm, around the size of the expected CTR spot size. This fiber connects to an 800 nm diode laser, which is a convenient wavelength to work with since it is both in the transmission range of KRS-5 and easily viewable using CCD cameras.

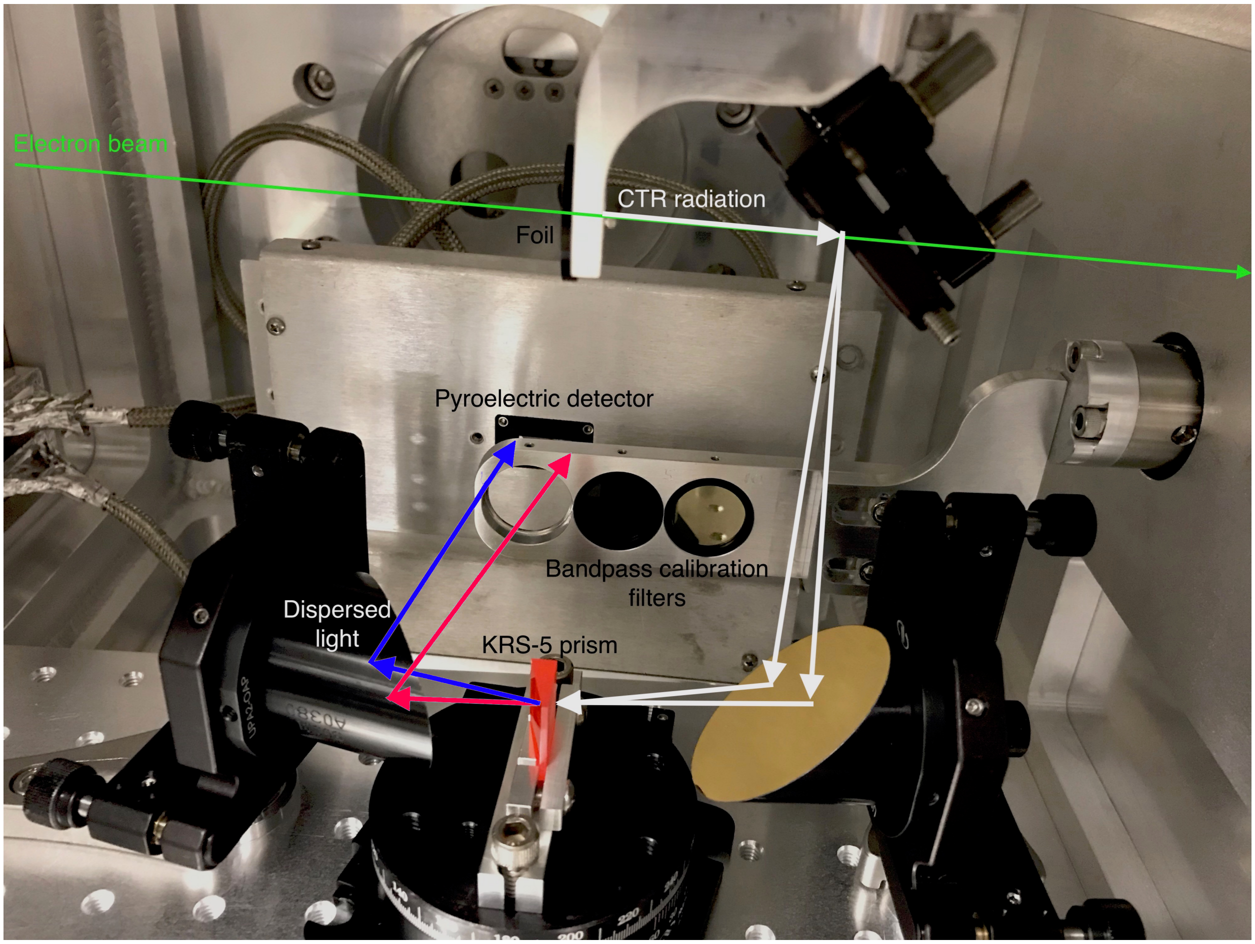

Figure 2.14: Photograph of the installed CTR system.

A “Uniblitz” [52] laser shutter with controllable rep rate and duty cycle was installed in line, as the pyroelectric detector requires a pulsed signal with duration of ≤ 2 ms at a rep rate ≤ 10 Hz to operate. The laser was directed through the system using IR viewer cards and cameras. Once aligned, a bare CCD was placed at the pyroelectric detector position to confirm that the system was performing as expected, shown in Figure 2.15. Then, the fiber holder was removed and the master alignment laser was passed through the LPA laser system and beamline. This laser dictates the path of the high power laser pulse and (up to jitter) the electron beam path. This laser does not have the correct divergence and spot size to be imaged by the CTR system but, since its wavelength is also 800 nm, if the central axis of the beam is aligned to the sensor pixel for 800 nm, the CTR system is referenced to the overall experiment. This is done by simply translating the detector normal to the beam

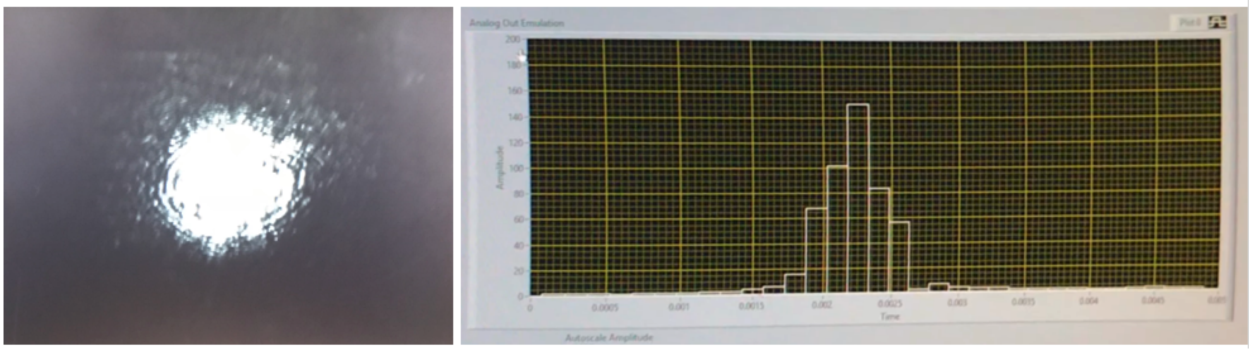

Figure 2.15: Left - Single mode fiber laser imaged on bare CCD at pyroelectric detector plane. Right - master alignment laser, shown on pyroelectric sensor readout.

until the Gaussian, shown in Figure 2.15, is centered on the left-most pixel.

2.5.3 Blackbody source

There are few options for producing intense broadband radiation over the near to far IR spectral range. One option is a blackbody source, i.e. a heated object designed to output a spectrum near that of a blackbody. Ideal blackbody spectra are given by Planck's law [53]:

$$B(\nu, T) = \frac{2h\nu^3}{c^2} \frac{1}{e^{h\nu/kT} - 1}, \tag{2.45}$$

where B is the spectral radiance, ν is the frequency of the radiation, T is the blackbody temperature, h is Planck's constant, c is the speed of light, and k is the Boltzmann constant. Some example spectra for ideal blackbodies at different temperatures are shown in Figure 2.16. Although the relative power at high wavelengths is greater for colder sources, the absolute power at any given wavelength will always be higher for the hotter source.

To benchmark the spectrometer's performance, a blackbody source (Infrared Systems Development model IR-508/201) with a pinhole opening was placed at the location of the CTR foil with the Uniblitz still in place. This source is rated to provide a stability of ±0.2 C with an emissivity >99%. The highest temperature achievable was 1000 C but, even at this high temperature, the power output is relatively low which, combined with the detector's short integration time, leads to very low incident energies. The Stefan-Boltzmann law [54]

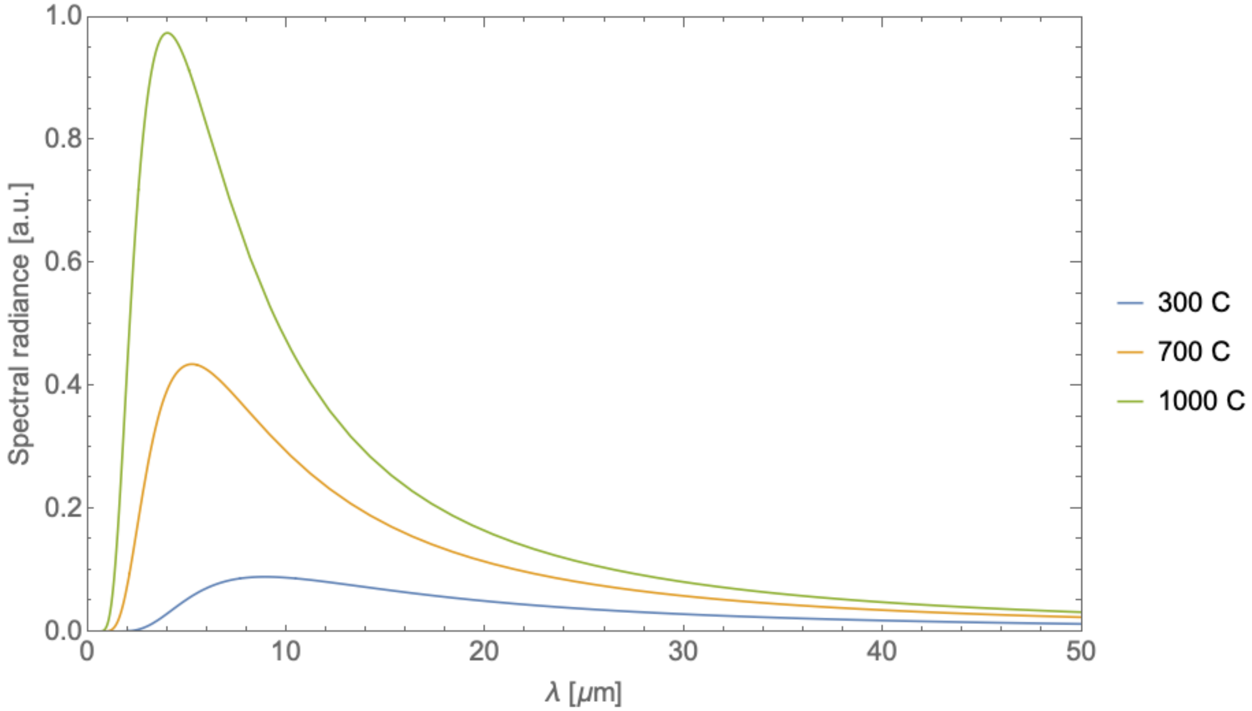

Figure 2.16: Example spectra for ideal blackbodies at different temperatures.

gives the total radiated power (over all wavelengths) for a blackbody source per unit area, j^*, as:

$$j^* = \sigma T^4, \tag{2.46}$$

where σ is the Stefan-Boltzmann constant = 5.67E-8 $\frac{\mathrm{W}}{\mathrm{m}^2\mathrm{K}^4}$. Considering an emitter with diameter 10 μm (i.e. the CTR spot size) and a detector integration time of 2 ms, this gives total energy equal to 23 nJ over all wavelengths for a 1000 C blackbody. Due to the limited spectral range of the system, limited solid angle collection, and transmission losses, this would not be resolvable by the detector with its 1 nJ/pixel sensitivity. Instead, a larger aperture pinhole of 380 μm was used, increasing the available photon energy but reducing the spectral resolution due to smearing from the larger source size, as the pinhole size is around the pixel size (500 μm). This gives more of a buffer with a theoretical upper bound on energy of 34 μJ.

This data was collected along with background data for subtraction; at the very low en-

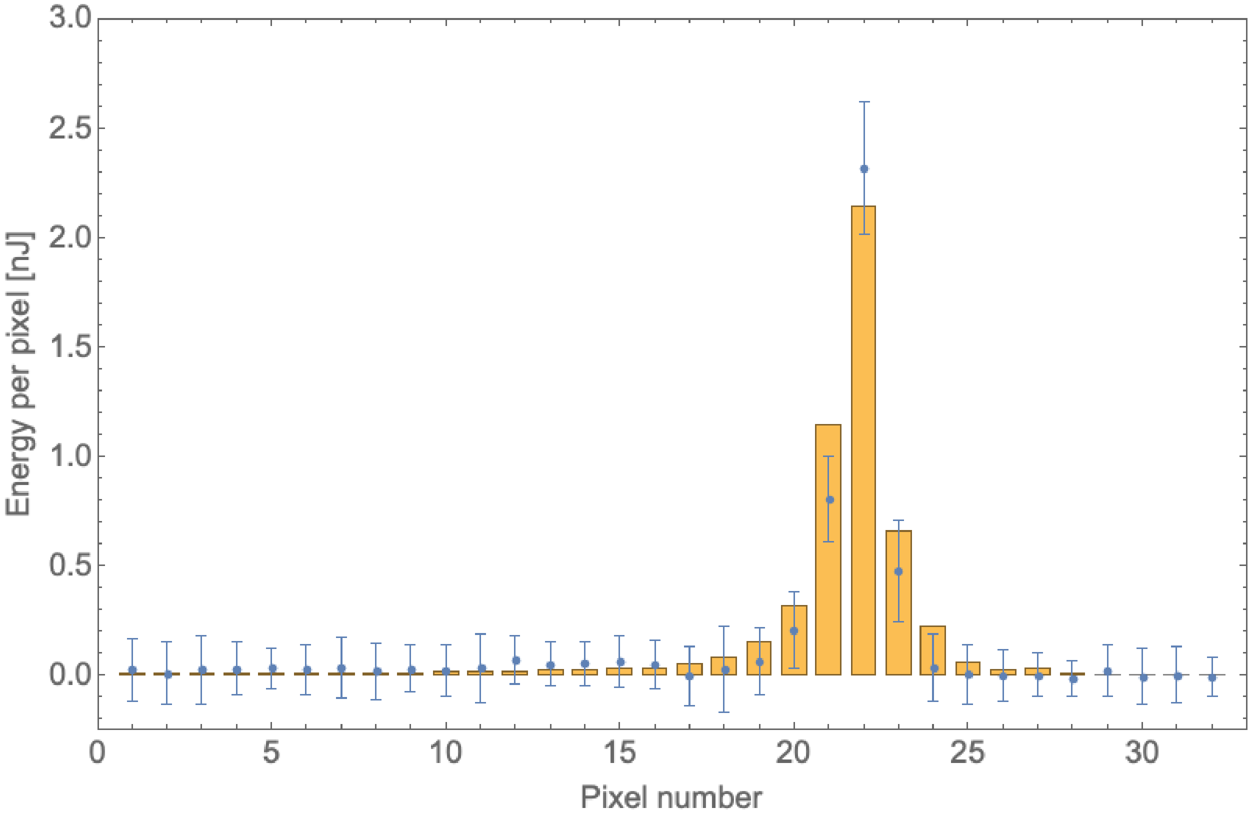

Figure 2.17: Pyroelectric sensor readings, averaged for 200 shots of exposure to 2 ms of 1000 C blackbody radiation through a 380 μm pinhole into the CTR spectrometer. Measured values are in blue with 1 standard deviation error bars. Orange bars are the start to end simulation results for this situation.

ergy levels required for this test, the intrinsic detector noise is considerable. The background scans yielded an average pixel reading of 0.51 nJ with a standard deviation of 0.18 nJ. The average, background subtracted results for 200 shots is shown in Figure 2.17 and compared to simulated results. The simulated results use the same technique described in section 2.4, except with the relevant source parameters updated to reflect the size, spectrum, and divergence of a 1000 C blackbody source through a 380 μm pinhole. The transverse detector position and overall intensity were left as fit parameters.

The spectra of both the measured and simulated cases were reconstructed by asserting that each pixel's central wavelength had a spectral energy density of the recorded value, shown in Figure 2.18. Despite the very poor signal to noise ratio, the reconstructed spectrum

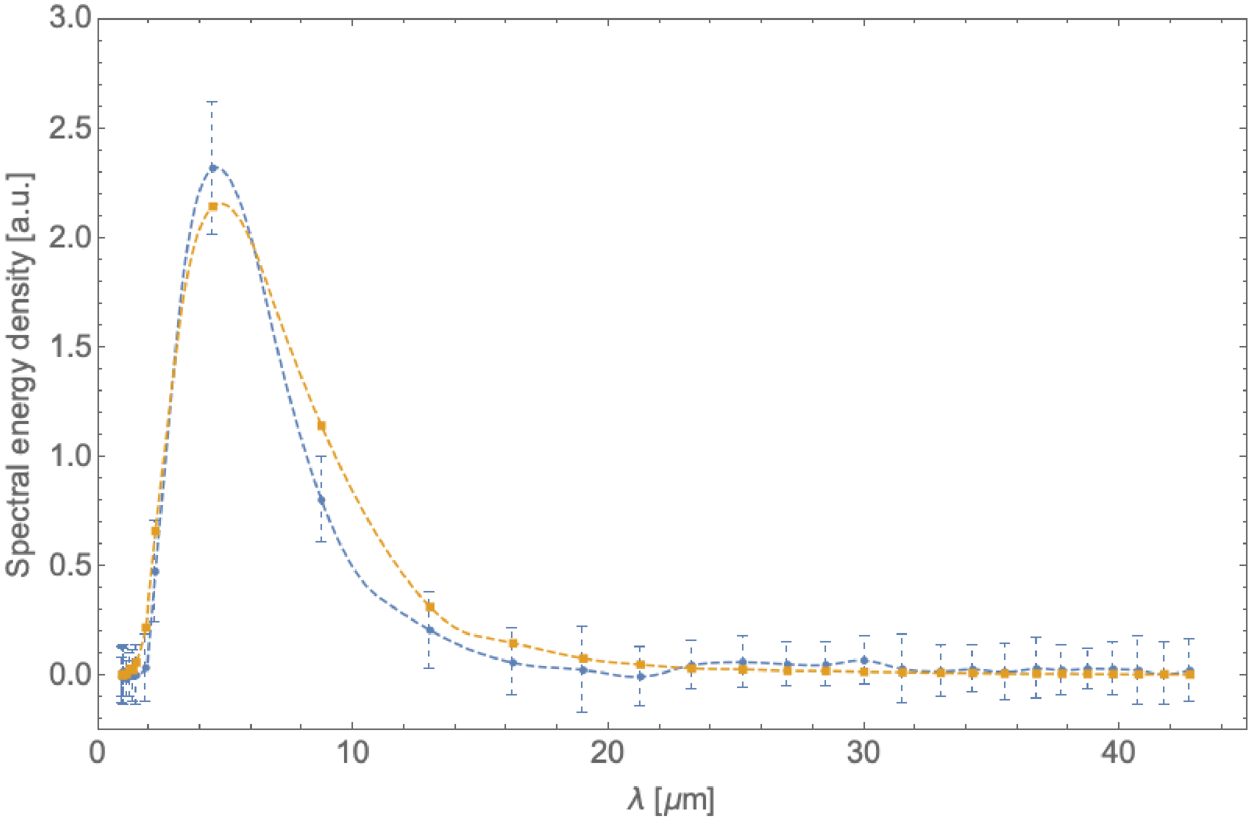

Figure 2.18: Reconstructed spectra for measured (blue) with one standard deviation error bars and simulated (orange) detector readings. Each point corresponds to a central wavelength of a pixel. The lines are intended to guide the eye and employ a second order spline interpolation.

from the measured data appears to agree well with the actual, blackbody spectrum. We sought to measure the blackbody spectrum with calibrated IR filters to more rigorously quantify the spectrometer's performance. Due to the very limited energy available though, no signal above background was measured with any IR filter.

2.5.4 In-situ filters

Since both alignment and calibration via blackbody require removing the CTR foil, they are not suitable for realtime calibration during a run. Another option to verify the system is working as expected is the inclusion of bandpass filters. Two IR bandpass filters at 4,750 nm and 9,500 nm, each with FWHM transmission windows of 500 nm, were purchased and installed on a linear vacuum feedthrough (See Figure 2.14). By inserting the filters while CTR is being generated, those two wavelength bands can be positively identified with the associated pixel(s) of the pyroelectric detector, permitting realtime calibration.

2.6 Preliminary electron beam results

The CTR system was designed for use with LPA generated electron beams described by [21, 31, 55]:

- Energy: 120 - 250 MeV
- Charge: 30 - 100 pC
- Spot size at CTR foil: 10 - 100 μm

To date though, such electron beams have not been delivered due to laser quality issues, an incorrect focusing triplet, chromatic focusing effects, and suboptimal LPA injection techniques. In March of 2019, an experimental run was conducted to test the CTR system. The best beams generated though were approximately 30 pC, 60 MeV with large spread, and focused to a 1 mm spot size. CTR arising from these parameters was simulated using the start to end techniques of Section 2.4. The resulting simulated detector response is shown in Figure 2.19; compare to the expected performance with nominal beams in Figure 2.13. Even with the most ambitious case of $\sigma_z = 1$ μm, no pixel receives even a single nJ and in the $\sigma_z = 10$ μm case, over 1,000 times more energy is required to meaningfully resolve the CTR spectra.

LBNL is continuing to refine their LPA and electron optics to achieve the initial design beam specs. To address laser beam quality, they are installing a deformable mirror and wavefront sensor. They are purchasing a new permanent magnet quadrupole (PMQ) triplet which will improve focusing. Beam quality will be improved by changing from ionization injection to down-ramp injection [38, 37]. The improved laser quality and injection will also reduce the energy spread of the beam and therefore mitigate the chromatic focusing issues.

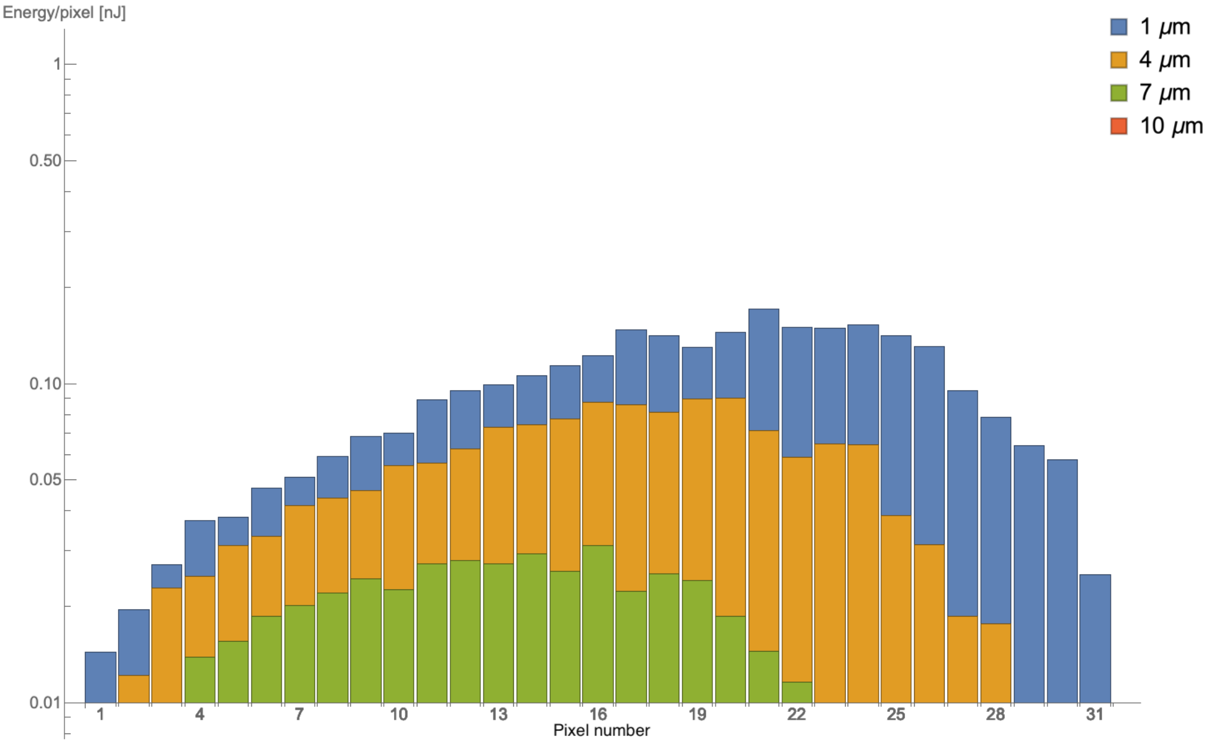

Figure 2.19: Simulated detector responses for LPA beams with specs: 60 MeV, 30 pC, 1000 μm spot size with σ_z values of 1, 4, 7, and 10 μm (The 10 μm case is below the lower limit on this plot).

CHAPTER 3

Chicane

3.1 Motivation

There are many constraints on the beam parameters for an electron beam to be successfully used in an FEL, discussed in greater detail in Chapter 4. To motivate this chapter though, consider the condition on energy spread: $\sigma_\gamma < \rho$. ρ is the *Pierce parameter*, a unitless value given by [4]:

$$\rho = \left(\frac{I_e K_0^2 [\mathrm{JJ}]^2}{16 I_A \gamma_0^3 \sigma_x^2 k_u^2} \right)^{1/3}, \tag{3.1}$$

where I_e is the beam current, K_0 is the undulator strength parameter, [JJ] is the Bessel function factor dependent on K_0 (of order unity), I_A is the Alfvén current, γ_0 is the beam Lorentz factor, σ_x is the transverse beam size, and k_u is the undulator wave number. Since FEL gain length scales approximately with the inverse of ρ [4] the having a large Pierce parameter is often desirable. Typical values of ρ in conventional undulators are on the order 10^{-4} to 10^{-3}.

As noted in Chapter 1 though, LPA beams have energy spreads much larger than these ρ values. However, by decompressing the beam, the local energy spread over a coherence length, $\lambda_c = \lambda_r / 4\pi\rho$, can be reduced below ρ, enabling lasing [21]. The BELLA FEL experiment will employ a chicane to stretch the beam by introducing a correlation between the energy and the longitudinal position, i.e. a chirp. Figure 3.1 shows how a short beam with high energy spread can be chirped, resulting in a longer beam with lower current but a smaller local energy spread.

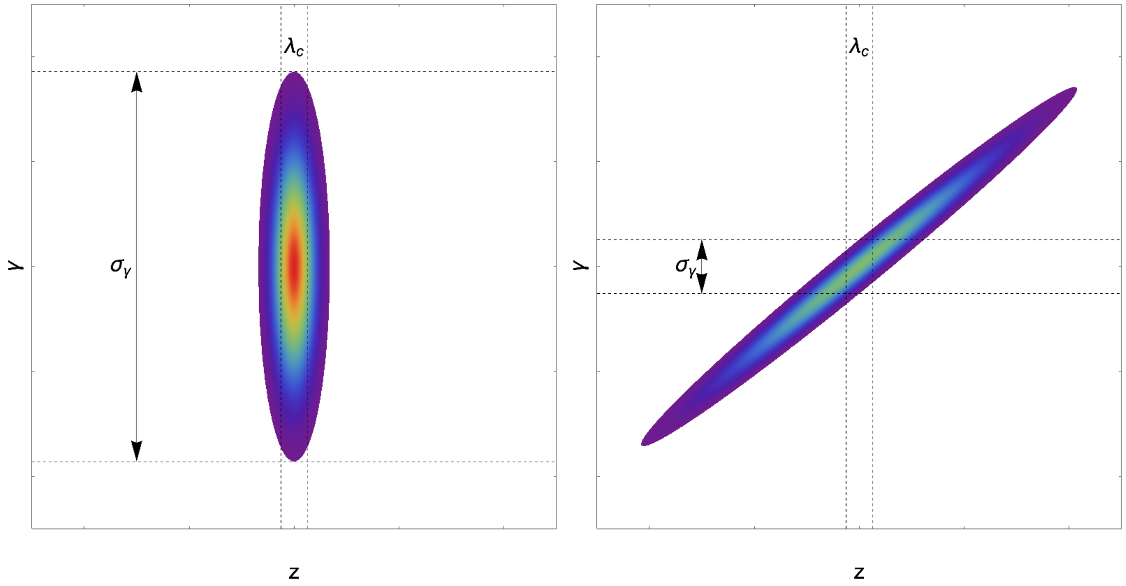

Figure 3.1: A cartoon of longitudinal phase space of an LPA beam before and after being chirped by a chicane. Observe how the local energy spread, σ_γ, over a coherence length, λ_c, is reduced by chirping.

3.2 Chicane fundamentals

3.2.1 Quantifying energy/position correlation

In beam physics, it is typical to express linear transformations of the beam using the 6D $\mathbf{R}$ transfer matrix [56, 57]:

$$\mathbf{R} \equiv \begin{pmatrix} R_{11} & R_{12} & R_{13} & R_{14} & R_{15} & R_{16} \\ R_{21} & R_{22} & R_{23} & R_{24} & R_{25} & R_{26} \\ R_{31} & R_{32} & R_{33} & R_{34} & R_{35} & R_{36} \\ R_{41} & R_{42} & R_{43} & R_{44} & R_{45} & R_{46} \\ R_{51} & R_{52} & R_{53} & R_{54} & R_{55} & R_{56} \\ R_{61} & R_{62} & R_{63} & R_{64} & R_{65} & R_{66} \end{pmatrix} = \begin{pmatrix} \frac{\partial x_f}{\partial x_i} & \frac{\partial x_f}{\partial x'_i} & \frac{\partial x_f}{\partial y_i} & \frac{\partial x_f}{\partial y'_i} & \frac{\partial x_f}{\partial \zeta_i} & \frac{\partial x_f}{\partial \delta_i} \\ \frac{\partial x'_f}{\partial x_i} & \frac{\partial x'_f}{\partial x'_i} & \frac{\partial x'_f}{\partial y_i} & \frac{\partial x'_f}{\partial y'_i} & \frac{\partial x'_f}{\partial \zeta_i} & \frac{\partial x'_f}{\partial \delta_i} \\ \frac{\partial y_f}{\partial x_i} & \frac{\partial y_f}{\partial x'_i} & \frac{\partial y_f}{\partial y_i} & \frac{\partial y_f}{\partial y'_i} & \frac{\partial y_f}{\partial \zeta_i} & \frac{\partial y_f}{\partial \delta_i} \\ \frac{\partial y'_f}{\partial x_i} & \frac{\partial y'_f}{\partial x'_i} & \frac{\partial y'_f}{\partial y_i} & \frac{\partial y'_f}{\partial y'_i} & \frac{\partial y'_f}{\partial \zeta_i} & \frac{\partial y'_f}{\partial \delta_i} \\ \frac{\partial \zeta_f}{\partial x_i} & \frac{\partial \zeta_f}{\partial x'_i} & \frac{\partial \zeta_f}{\partial y_i} & \frac{\partial \zeta_f}{\partial y'_i} & \frac{\partial \zeta_f}{\partial \zeta_i} & \frac{\partial \zeta_f}{\partial \delta_i} \\ \frac{\partial \delta_f}{\partial x_i} & \frac{\partial \delta_f}{\partial x'_i} & \frac{\partial \delta_f}{\partial y_i} & \frac{\partial \delta_f}{\partial y'_i} & \frac{\partial \delta_f}{\partial \zeta_i} & \frac{\partial \delta_f}{\partial \delta_i} \end{pmatrix} \tag{3.2}$$

such that the initial beam state vector $\mathbf{r}_i$ is transformed to the final state $\mathbf{r}_f$:

$$\mathbf{r}_f = \begin{pmatrix} x_f \\ x'_f \\ y_f \\ y'_f \\ \zeta_f \\ \delta_f \end{pmatrix} = \mathbf{R}\,\mathbf{r}_i = \mathbf{R} \begin{pmatrix} x_i \\ x'_i \\ y_i \\ y'_i \\ \zeta_i \\ \delta_i \end{pmatrix} \tag{3.3}$$

where ζ is the longitudinal particle position relative to the design trajectory and $\delta \equiv \Delta\gamma/\gamma_{design}$. The matrix element R_{56} describes introducing a correlation between energy and longitudinal position, specifically a linear chirp. It is the figure of merit in chicane design.

3.2.2 Chicane dynamics

A chicane is a dispersive optic for charged particles, typically comprised of four dipole magnets. Particles are deflected by the magnets, with lower energy particles being deflected more, forcing them to take a longer trajectory. Figure 3.2 illustrates a basic chicane. Observe how the lower energy particles (in green) take a longer path, causing them to lag behind the higher energy particles at the exit of the device.

The motion of electrons through a chicane will be described by the Lorentz force equation [26]:

$$\frac{\mathrm{d}\mathbf{p}}{\mathrm{d}t} = q(\mathbf{E} + \mathbf{v} \times \mathbf{B}), \tag{3.4}$$

where $\mathbf{p}$ is the particle momentum, q is its charge, $\mathbf{E}$ is the electric field, $\mathbf{v}$ is the particle velocity vector, and $\mathbf{B}$ is the magnetic field. In the relativistic case, $\mathbf{p} = \gamma(|\mathbf{v}|)m_0\mathbf{v}$ and in a chicane there is no electric field. Since there are only magnetic fields, the beam energy and therefore γ will remain constant: $\gamma(|\mathbf{v}|) = \gamma_0$. These substitutions give the expression:

$$\frac{\mathrm{d}\mathbf{v}}{\mathrm{d}t} = \frac{q}{\gamma_0 m_0}\mathbf{v} \times \mathbf{B}. \tag{3.5}$$

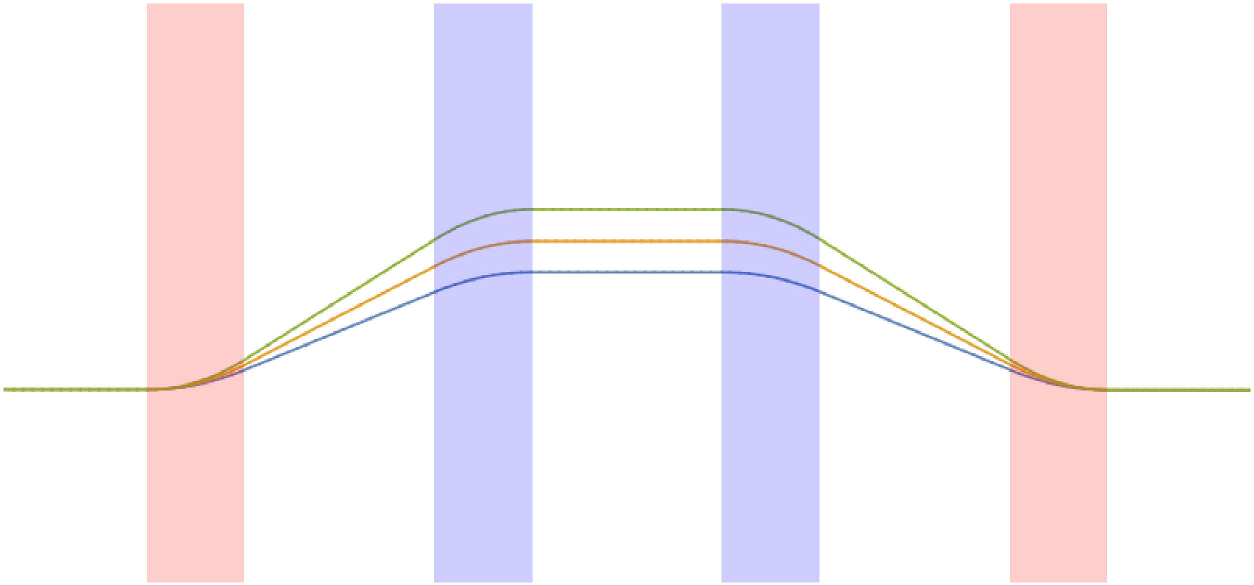

Figure 3.2: A schematic of the trajectories of charged particles within a chicane. The red sections correspond to regions with magnetic field pointing out of the page while the blue regions have magnetic field pointing into the page. The green, orange, and blue lines correspond to the trajectories of negatively charged particles of increasing energies.

By assuming that the magnetic fields that are not in the $\hat{y}$ direction are negligible and that the field is flat in the transverse direction, then $\mathbf{B} \approx B_y(z)\hat{y}$. Finally, assume that the particle motion is overwhelmingly in the initial direction, defined as $\hat{z}$, then $v_z \approx c$. Then a simplified, approximate expression for the equation of motion in x is:

$$\frac{\mathrm{d}v_x}{\mathrm{d}t} = \frac{-qcB_y(z)}{\gamma_0 m_0}. \tag{3.6}$$

For some purposes, it will be easier to use an expression with z as the independent variable instead of t; simply multiply through by $\frac{\mathrm{d}t}{\mathrm{d}z}$ which we have approximated as $1/c$:

$$\frac{\mathrm{d}v_x}{\mathrm{d}t}\frac{\mathrm{d}t}{\mathrm{d}z} = \frac{-qcB_y(z)}{\gamma_0 m_0}\frac{\mathrm{d}t}{\mathrm{d}z}, \tag{3.7}$$

$$\frac{\mathrm{d}v_x}{\mathrm{d}z} = \frac{-qB_y(z)}{\gamma_0 m_0}. \tag{3.8}$$

This expression allows the use of a useful shorthand for real world magnetic systems: magnets can be described in terms of their integrated field, $\int B\,\mathrm{d}z$, defined simply by:

$$\text{Integrated field} = \int B\,\mathrm{d}z \equiv \int_{-\infty}^{\infty} B_y(z)\,\mathrm{d}z \tag{3.9}$$

Manufacturers and magnet designers will often provide this number as a basic specification in units of Tesla-meter or Gauss-cm when discussing beamline magnets, e.g. [58]. Using the integrated field and equation (3.8) the transverse kick induced by a single, idealized dipole magnet is:

$$\Delta v_x = \frac{-q(\int B\,\mathrm{d}z)}{\gamma_0 m_0}. \tag{3.10}$$

In the limit of small deflections, this gives an approximate angular deflection of

$$\theta_x = \frac{-q(\int B\,\mathrm{d}z)}{\gamma_0 m_0 c}, \tag{3.11}$$

or a maximum transverse offset, called the *sagitta*, of

$$x_{\text{sagitta}} = \frac{-L_{\text{out}}q(\int B\,\mathrm{d}z)}{\gamma_0 m_0 c}. \tag{3.12}$$

In these expressions, the actual fields and physical geometry of a bending magnet have been abstracted away. It is now possible to treat a whole magnet as a single delta function impulse according to the integrated field. The chicane from Figure 3.2 has had its magnets replaced with delta function impulses to create Figure 3.3.

In this case, the distance travelled by a particle is given by:

$$L_{tot} = 2L_H + (\text{const}) = 2\frac{L_{out}}{\cos(\theta_x)} + (\text{const}), \tag{3.13}$$

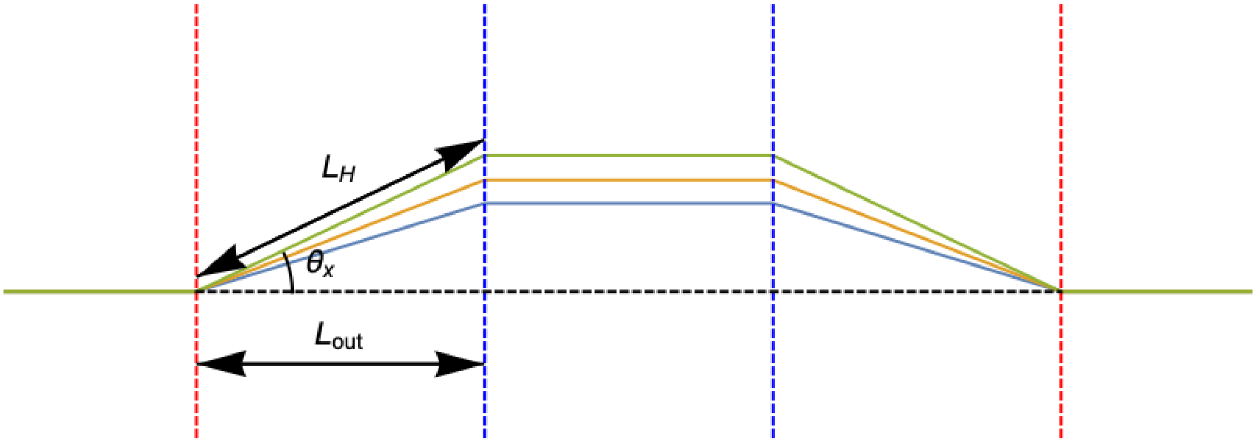

Figure 3.3: A schematic of the trajectories of charged particles within an idealized chicane with impulse magnets. The red and blue dashed lines correspond to positive and negative delta function kicks respectively. As in Figure 3.2, the green, orange, and blue lines correspond to the trajectories of negatively charged particles of increasing energies.

where L_H is the length of the hypotenuse travelled by a particle, L_{out} is the spacing between dipoles 1 and 2 and dipoles 3 and 4 (Shown in Figure 3.3), and θ_x is given by equation (3.11). Using the $\mathbf{R}$ matrix definition in equation (3.2) we can now use equation (3.13) to find the R_{56} of a chicane. First substitute the definition of θ_x from equation (3.11) and replace γ with $\gamma_{\text{design}}(1+\delta)$ where δ is the relative deviation of a particle's energy from the design energy, γ_{design}:

$$L_{tot} = 2\frac{L_{out}}{\cos(\frac{-q(\int B\,\mathrm{dz})}{\gamma_{design}(1+\delta)m_0c})} + (\text{const}). \tag{3.14}$$

Continue to apply the small angle approximation to simplify the cosine:

$$L_{tot} = 2\frac{L_{out}}{1-\frac{1}{2}\left(\frac{q(\int B\,\mathrm{dz})}{\gamma_{design}(1+\delta)m_0c}\right)^2} + (\text{const}). \tag{3.15}$$

Taking the partial derivative with respect to δ gives the definition of R_{56}:

$$R_{56} \equiv \frac{\partial L_{tot}}{\partial \delta} = -\frac{8(\int B\,\mathrm{d}z)^2 c^2 L_{out} m^2 q^2 \gamma_{design}^2 (1+\delta)}{((\int B\,\mathrm{d}z)^2 q^2 - 2c^2 m^2 \gamma_{design}^2 (1+\delta)^2)^2}. \tag{3.16}$$

Finally, to clean up the result, take this expression in the limit of small δ and small deflection, leaving:

$$R_{56} \approx -\frac{2(\int B\,\mathrm{d}z)^2 L_{out} q^2}{c^2 m^2 \gamma_{design}^2} \tag{3.17}$$

Although not necessarily useful in this particular context, this result reduces one step further to a commonly quoted expression (e.g. [59]) by evaluating equation (3.11) at $\gamma_0 = \gamma_{design}$ and calling the result θ_0, giving:

$$R_{56} \approx -2L_{out}\theta_0^2 \tag{3.18}$$

This means that, given a beam energy, γ_{design}, the integrated field of the dipole magnets and/or the dipole magnet spacing can be adjusted to produce a desired R_{56} value.

3.3 Optimization of low aspect ratio, iron dominated dipole magnets

This section is adapted from [60] in accordance with the UCLA's dissertation guidelines, section "Alternate versions of published articles". It describes the optimization of pole faces for low aspect ratio magnets and its results will be used throughout this chapter.

3.3.1 Introduction

Many disciplines employ dipole magnets, often requiring a consistent, flat field over some volume of interest. These include beam [61, 10, 62, 63, 64], plasma [65], and AMO physics [66] as well as myriad applications in chemistry [67, 68], engineering [69], and medicine [70, 71]. A particular subclass of interest is that of iron-dominated magnets, in contrast with coil dominated, *e.g.* superconducting and air cored, wherein the field in the region of interest is shaped by a ferromagnetic yoke and, most importantly, pole face. In these magnets, the high permeability of ferromagnetic materials (typically iron-based) is used to confine, direct, and amplify the magnetic flux from a source, generally coils of wire or permanent magnets. To produce a larger volume of flat field, the most obvious approach is to simply increase the size of the yoke and pole faces. In some applications, this approach (with minor refinements discussed below) is sufficient. This work will discuss the optimization of field quality for a fixed magnet size where the gap between the pole faces is of the same order as the width of the pole face - the case of low aspect ratio. Such magnets are especially useful in the rapidly advancing field of laser plasma accelerators [10, 72, 73, 74] where the width of good field region required might be low but the gap between pole faces needs to be large to accommodate the large beam pipes required for downstream transport of the drive laser.

3.3.2 Theoretical treatment

3.3.2.1 Multipole decomposition

A brief derivation of the multipole convention follows, with a more thorough explanation found in Ref. [61]. Maxwell's equations for magnetostatics in the absence of sources are

$$\begin{aligned} \nabla \times \mathbf{B} &= 0, \\ \nabla \cdot \mathbf{B} &= 0. \end{aligned} \tag{3.19}$$

One may define a vector field $\mathbf{F} = \mathbf{A} + iV$ such that $\mathbf{B} = \nabla \times \mathbf{A} = -\nabla V$. In the 2D, current free case, it can be shown that if $\mathbf{F}$ is written as a function of $z = x + iy$, then $\mathbf{F}$ satisfies the Maxwell conditions by construction. The real part of $\mathbf{F}$ gives the flux lines while the imaginary part gives the equipotentials. One particularly useful definition which expresses $\mathbf{F}$ as $\sum C_n z^n$ is called the *multipole decomposition.* In the multipole decomposition $n = 1$ refers to the dipole component, $n = 2$ is the quadrupole component, $n = 3$ is the sextupole component, and so on. A commonly employed approximation is to treat the iron elements of a system as having infinite permeability. This means that the pole face surface is an equipotential surface and that conformal mapping can transform an infinite pole face and its concomitant perfect, infinite dipole field into the fields of a finite pole [75]. This approximation is generally insufficient for real world magnet design due to the finite permeability of iron, coil fields, saturation, and other considerations. Therefore, it tends to only be a useful starting point for refinement in finite element method (FEM) simulations.

3.3.2.2 Flat and shimmed poles

The most common way to improve the good field region for a given aspect ratio (AR) is by *shimming* the pole face by placing small, numerically optimized bumps at the edges of the face. Expressions of the form

$$\frac{a}{h} = c_1 \ln\left(\frac{\Delta B}{B}\right) + c_2, \tag{3.20}$$

are given in [61], where a is the overhang of the pole face extending beyond the good field region, h is the gap between the magnet mid-plane and the pole face, and $\Delta B/B$ is the maximum allowable, normalized field error. Coefficients c_1 and c_2 for both shimmed and flat cases are provided, giving a relationship between the magnet geometry and the field quality required. We define the term *good field region*, x_{gfr}, as the width on axis of the good field region satisfying *good field quality*, $\mathrm{GFQ} = B/\Delta B$. By writing

$$\mathrm{AR} = \frac{a + x_{\mathrm{gfr}}}{h}, \tag{3.21}$$

equation 3.21 can be rearranged as

$$\begin{aligned}
\mathrm{AR}_{\mathrm{unopt}} &= \frac{x_{\mathrm{gfr}}}{h} - 0.9 - 0.36 \ln\left(\frac{1}{\mathrm{GFQ}}\right) \\
\mathrm{AR}_{\mathrm{opt}} &= \frac{x_{\mathrm{gfr}}}{h} - 0.25 - 0.14 \ln\left(\frac{1}{\mathrm{GFQ}}\right).
\end{aligned} \tag{3.22}$$

with the provided coefficients for the unoptimized flat case and optimized shim case respectively.

Although it was not made explicit by the analysis of Tanabe, these equations break down for magnets where the gap is comparable or large compared to the pole width (detailed below). This divergence motivated the search for improved pole face designs for low AR magnets.

3.3.2.3 Parabolic poles

The symmetry conditions of a particular magnet design will impose boundary conditions which forbid certain multipole components; the remaining, allowed components comprise the *error spectrum*. The symmetry constraint on the n^{th} moment for a N^{th} order magnet is:

$$F_n\left(\theta + \frac{\pi}{N}\right) = -F_n(\theta). \tag{3.23}$$

There is an extended discussion of the application of Eq. 3.23 in Ref. [61] but we will only concern ourselves with the dipole case which has allowed multipole moments $n = 3, 5, 7, 9...$ Therefore, the lowest order error which needs to be counteracted is $n = 3$, or sextupole. In a dipole with finite, flat pole faces, this manifests as a "virtual sextupole" which causes the field lines to bow out, away from the center. This is illustrated in Figure 3.4 for $C_1z + C_3z^3$.

Note that the equipotentials bow towards the center. This can be counteracted by curving the pole face in a manner equal and opposite to this equipotential curve, strengthening the field near the edges to reduce the virtual sextupole. By selecting a parabolic profile with an even greater curvature, intrinsic sextupole focusing can be realized in a linear undulator [76]. The optimization described below uses this approach to seed the final FEM optimization which will account for considerations left out of this approximation.

For example, consider an AR = 1 dipole, shown in Figure 3.5. After a multipole decomposition, normalizing to the dipole coefficient (*i.e.* $C_1 = 1$), the sextupole contribution is $C_3 = 0.035$ inside a 0.5 gap unit radius circle on centerline. The corresponding field lines and equipotentials from only these lowest order components are shown in Figure 3.6.

The equipotential line which is nearest to the pole face is found and is approximated with a parabola, in this case with equation $y = -0.10x^2 - 0.96$. Construct new pole faces

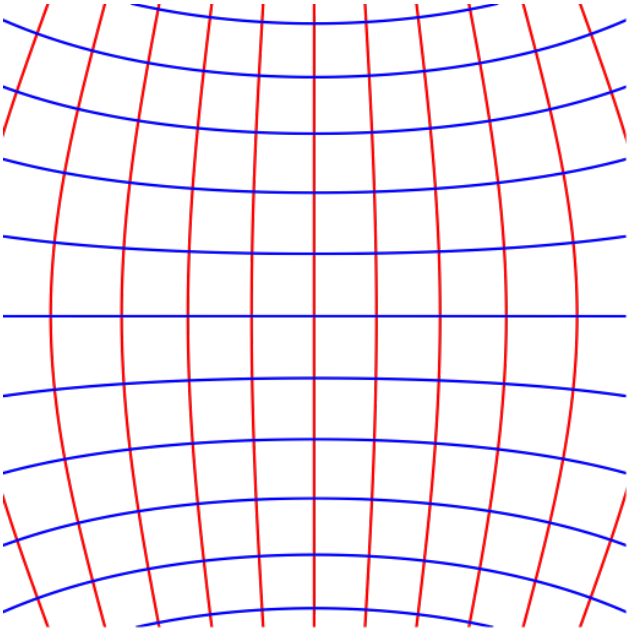

Figure 3.4: Field lines (red) and equipotentials (blue) for a dipole magnet with small virtual sextupole component.

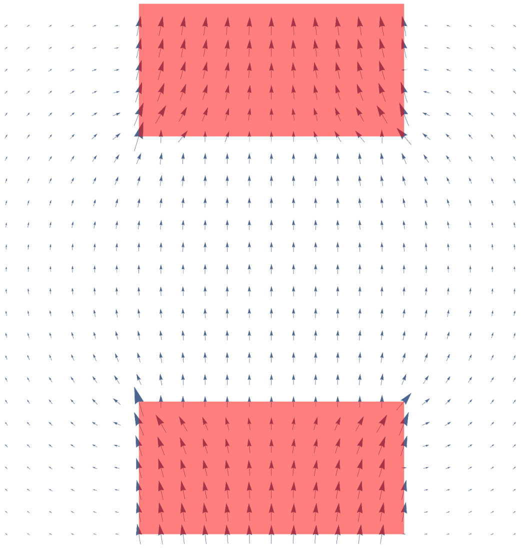

Figure 3.5: AR=1 dipole with flat pole faces (red) with magnetic field vector plot.

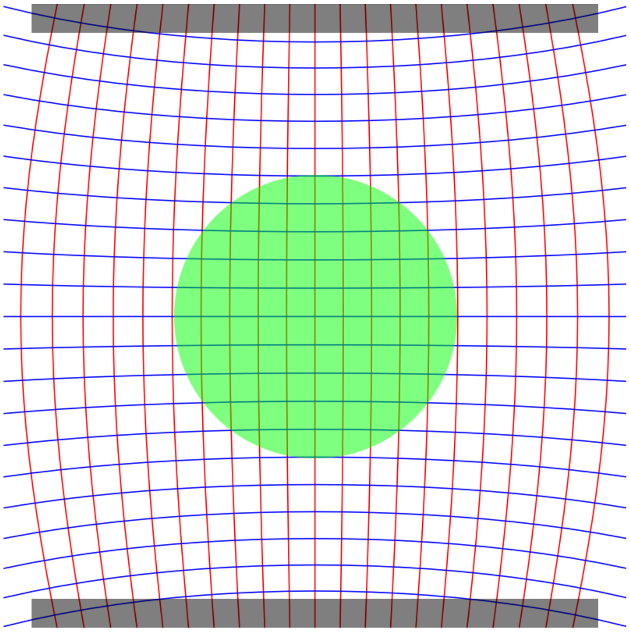

Figure 3.6: Field lines (red) and equipotentials (blue) for a $C_1 = 1$, $C_3 = 0.035$ field. Flat pole faces are shown in grey and the area where the decomposition is calculated is in green.

with parabolic component equal and opposite to this iso-contour curvature (Figure 3.7).

Calculating the multipole components as before, find that C_3 has been reduced by more than an order of magnitude to 0.003. This serves as a very good starting point for final FEM optimization to tune out higher order effects.

3.3.2.4 Splined poles

Using splines to define the pole face permits the creation of poles with arbitrary levels of complexity. Splines have been employed in the optimization of axisymmetric MRI magnets [77, 78]. The details of this current implementation are discussed in the following section.

3.3.3 Simulation methods

The parameter space of magnet design is continuous and multidimensional, so for this work a representative, discrete subset is examined which covers magnets which are both physically relevant and germane to the topic at hand. Specifically, we will consider three aspect ratios

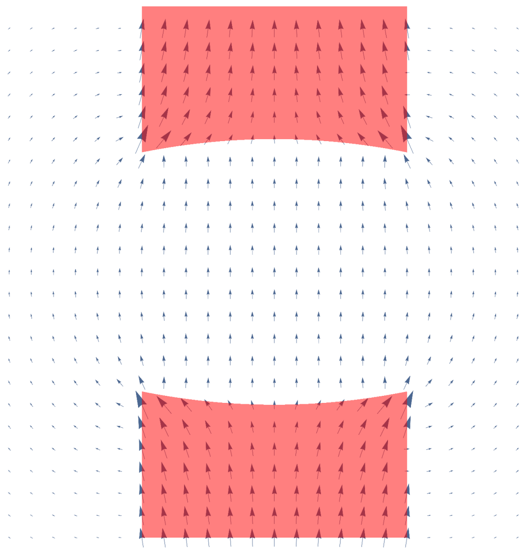

Figure 3.7: AR=1 dipole with parabolic ($\pm 0.1x^2 \mp 0.96$) pole faces (red) with magnetic field vector plot.

(AR): 0.5, 1, and 1.5; three good field requirements (GFQ): 1 in 10^3, 1 in $10^{3.5}$, and 1 in 10^4; and five pole face geometries: flat, shimmed, parabolic, three point spline, and five point spline.

We define here the following terms:

Aspect ratio - the ratio of the pole face gap at the centerline to the width of the pole at its widest;

Good field region - on the horizontal axis, the maximum x_{gfr} value such that

$$\frac{|\mathbf{B}(x,0) - \mathbf{B}(0,0)|}{|\mathbf{B}(0,0)|} < \frac{1}{\text{GFQ}}$$
$$\forall x < x_{\text{gfr}};$$

Shimmed - a semi-circle protrusion with center a distance one radius from the pole edge;

Spline - a cubic spline interpolation on points at $x = 0$, ± 0.5, and ± 1 width units for the three point spline and an interpolation of points at $x = 0$, ± 0.25, ± 0.5, ± 0.75, and ± 1 width units for a five point spline. The point at $x = 0$ has $y = 1$ gap unit and all other points

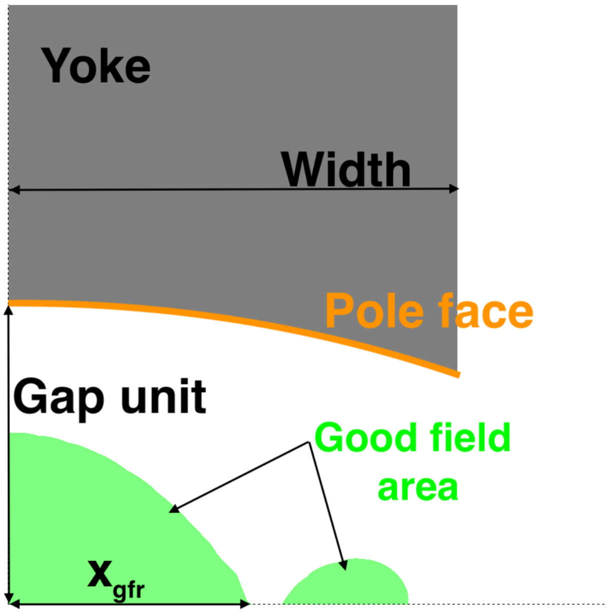

Figure 3.8: Visual aid to definitions of geometric features.

satisfy $y(x) = y(-x)$.

All geometries are subject to the additional constraint that they do not intersect a beam pipe with a radius of 0.9 gap units. In all cases (each AR, GFQ, and geometry) all free variables are adjusted to maximize x_{gfr}. In the shimmed and parabolic cases, each with one free variable, this is done with an exhaustive search. In the three- and five- point spline cases (with two and four free variables, respectively) this procedure is done using particle swarm optimization (PSO) [78, 79]. The 2D FEM simulation is done using the program POISSON [80], simulating a single quadrant of an H-magnet, with a mesh step size of 0.01 gap units. The pole face is taken to be far from the rest of the yoke and coils. It is further assumed that the magnet is operating far from saturation and the yoke is made from low carbon steel acting linearly with relative permeability, μ/μ_0, of 4000. All additional post processing, including the coordination of the particle swarm is done with Mathematica.

3.3.4 Simulation results

The results for x_{gfr} given in gap units follow, broken down by GFQ. Tables 1, 2, and 3 give the best case results for GFQs 10^3, $10^{3.5}$, and 10^4 respectively. Figures 3.9, 3.10, and 3.11 illustrate these results and compare them to theoretical results for shim-optimized and unoptimized pole faces obtained from Eq. 3.22. In these plots, better performance is indicated by points which are lower (smaller AR for given performance requirement) and further to the right (larger good field region for given GFQ and AR). It should be noted that the comparison to Ref [61] is imperfect due to the use of relatively low AR; in the more usual, AR>>1 regime, the "Flat" points should overlap the "Tanabe unoptimized" line and the "Shimmed" points should overlap the "Tanabe optimized" line.

Table 3.1: Optimal x_{gfr} in different geometric configurations with GFQ=10^3.

	AR = 0.5	AR = 1.0	AR = 1.5
Flat	0.05	0.09	0.21
Round shim	0.05	0.46	0.84
Parabolic	0.07	0.47	0.69
3 point spline	0.09	0.67	1.00
5 point spline	0.09	0.71	1.17

Table 3.2: Optimal x_{gfr} in different geometric configurations with GFQ=$10^{3.5}$.

	AR = 0.5	AR = 1.0	AR = 1.5
Flat	0.03	0.05	0.12
Round shim	0.03	0.35	0.68
Parabolic	0.04	0.35	0.53
3 point spline	0.05	0.57	0.83
5 point spline	0.05	0.59	1.00

Table 3.3: Optimal x_{gfr} in different geometric configurations with GFQ=10^4.

	AR = 0.5	AR = 1.0	AR = 1.5
Flat	0.02	0.03	0.06
Round shim	0.02	0.21	0.45
Parabolic	0.02	0.25	0.37
3 point spline	0.03	0.41	0.57
5 point spline	0.03	0.45	0.85

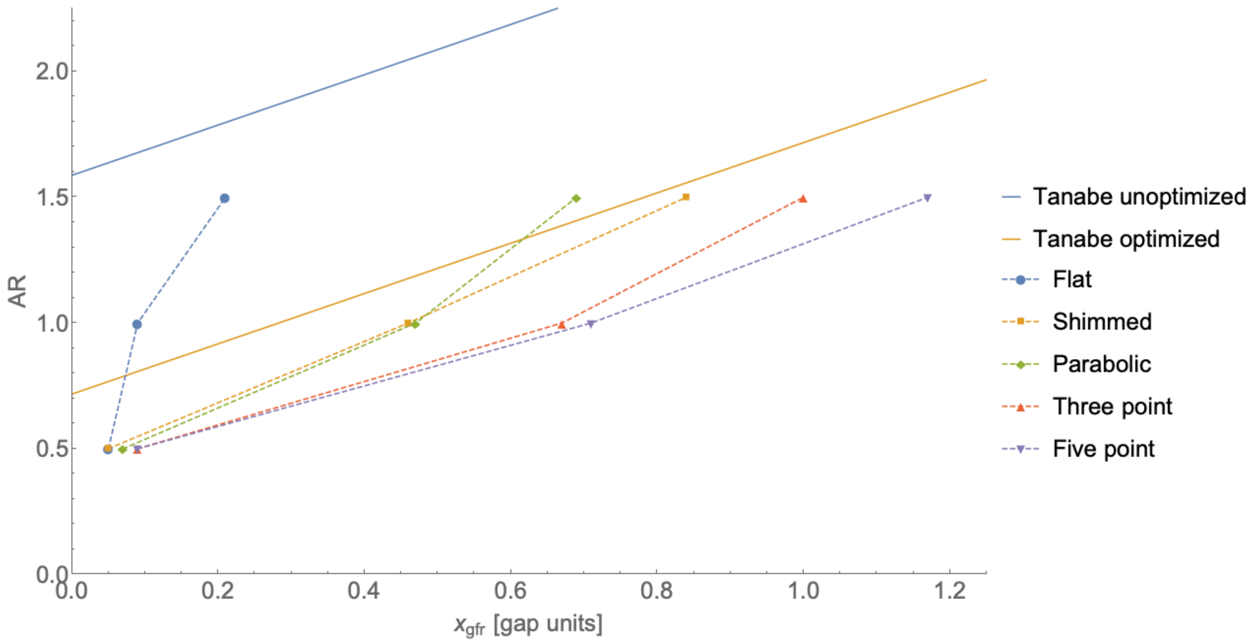

Figure 3.9: Optimized simulation results for GFQ = 10^3 vs [61] estimates. The dashed lines are intended to guide the eye.

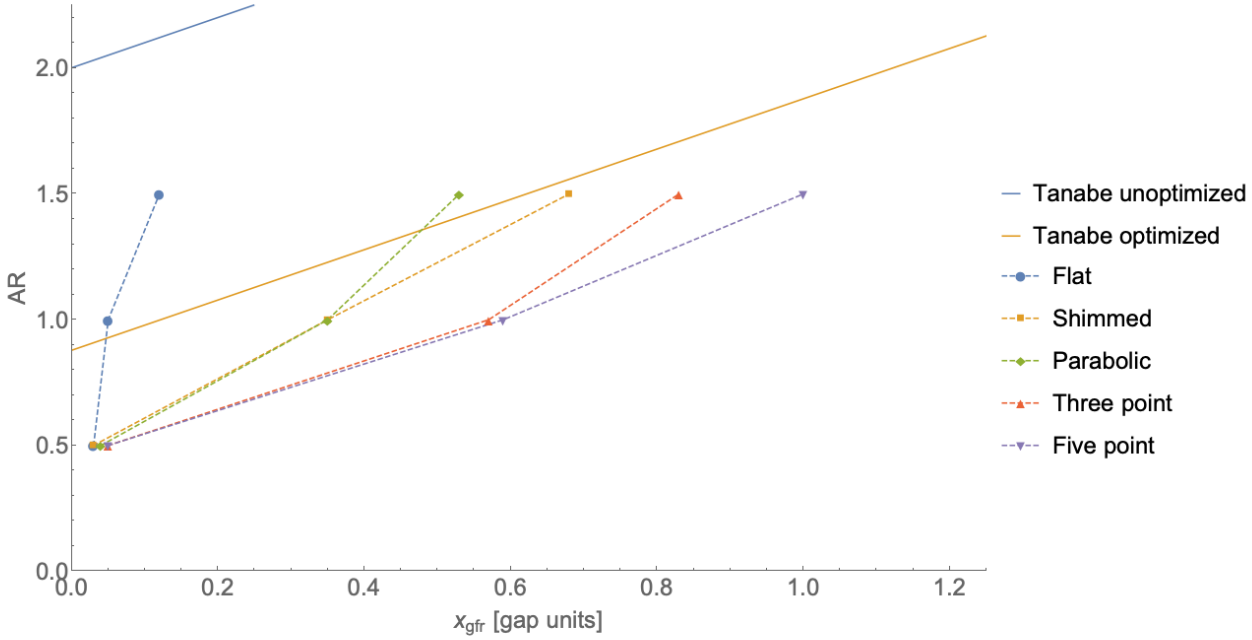

Figure 3.10: Optimized simulation results for GFQ = $10^{3.5}$ vs [61] estimates. The dashed lines are intended to guide the eye.

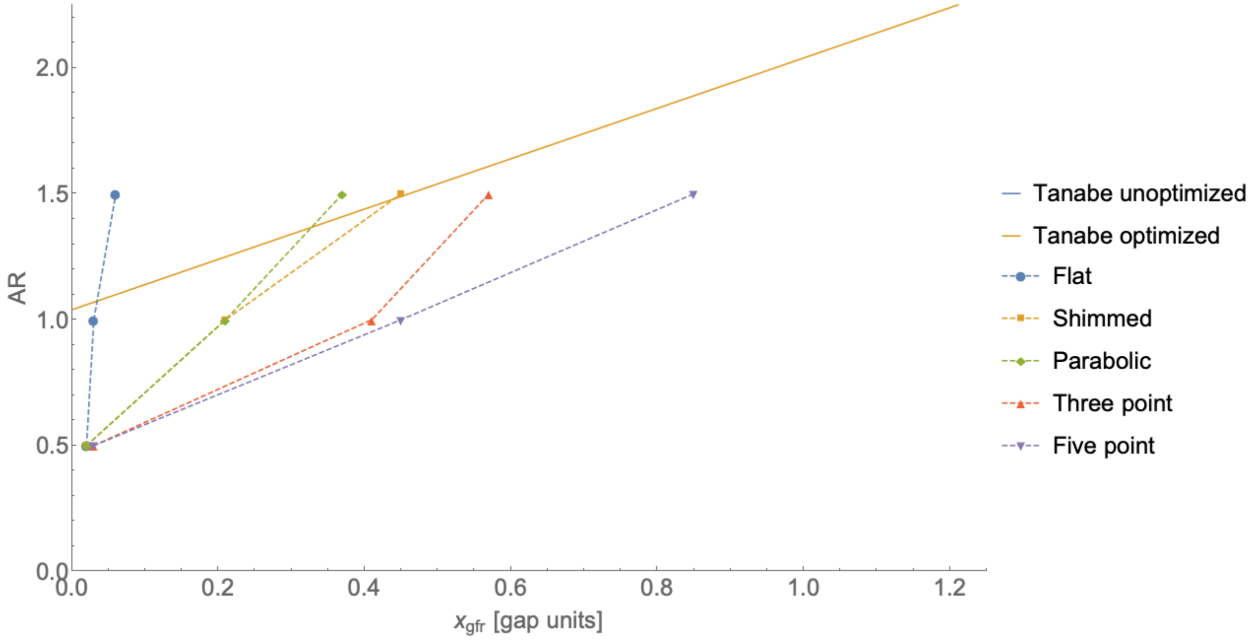

Figure 3.11: Optimized simulation results for GFQ = 10^4 vs [61] estimates. The dashed lines are intended to guide the eye.

In the original paper, a large appendix was included which details the coefficients used *to generate these optimizations as well as figures of all the cases they represent to guide the optimization of future magnets.*

In the cases of flat and shimmed magnets, a clear divergence from the predictions of [61] and equation 3.22 is evident. This breakdown of traditional heuristics in this low aspect ratio regime requires additional care to be taken when designing such magnets. With that said, it should be noted how effective shims are for higher aspect ratio magnets. Between these three GFQ definitions, shimming an AR = 1 or AR = 1.5 magnet tends to improve x_{gfr} by a factor of more than four. However, at AR = 0.5 there is no improvement from shimming. At AR = 1, parabolic faces have nearly identical performance with shims and at AR = 1.5 shims outperform parabolic faces. In all AR and GFQ cases, three point splines are superior to flat, shimmed, and parabolic faces and five point splines are superior to all other geometries. The superiority of the five point spline is expected since all other geometries are effectively (but not strictly) subsets of this geometry. This comes with the caveat that some of the geometries generated here have sharp corners which might readily saturate in some real-world scenarios. This limitation is discussed in greater detail in the next section.

3.4 Design of the UCLA-LBNL chicane

In addition to the two dimensional field quality discussed in the previous section, there are many other considerations when designing physical magnets including: fringe fields, current density in the windings, local and overall heating, mechanical rigidity, and weight. Additionally for this project, there were significant space limitations, the requirement that existing power supplies be used, and, due to the unavailability of preferable steel alloys, the use of suboptimal yoke material.

3.4.1 Magnetic field requirements

The most fundamental design considerations for a chicane are the magnetic field properties; producing these fields is the *raison d'être* of a chicane so every other design decision must support this goal. In this instance, the requirements were calculated during the conception of the experiment to accommodate the highest expected R_{56} value, 1 mm, at the highest expected beam energy, 300 MeV [55]. There is a total of 1.25 meters of space available for the chicane. A vacuum chamber to house a mirror for laser diagnostics and monochromator slits is to be placed between the center dipoles, occupying 30 cm. This leaves 22.5 cm per dipole. To account for coil overhang and to allow some variability in longitudinal positioning, a yoke length of 17.5 cm was selected giving $L_{\text{out}} = 30$ cm. Given the R_{56} requirement, this corresponds (equation 3.18) to a field of 0.26 T. This gives a maximum sagitta (equation 3.12) 12 mm. It was decided [55] that the dipoles should have a GFQ of at least 10^3 over an x_{gfr} of 10 mm.

Since the maximum sagitta is 12 mm and the minimum approaches zero, $x_{\text{sagitta}} = 5$ mm was used as a representative case for optimization. Dipoles 1 and 4 are centered on the beam axis while dipoles 2 and 3 are translated (in the bend plane) by 5 mm. So instead of the unshifted case where beams with x_{sagitta} ranging from 0 to 12 mm being up to 12 mm from any given dipole axis, now beams in this range will never be more than 7 mm from any dipole axis. This enables the more efficient use of the good field region.

3.4.2 Pole face design

In order to accommodate the beam pipe in this LPA experiment, a relatively large dipole aperture is required. The actual pipe exterior dimension was 2 inches but, per the dipole shift mentioned above, the beam pipe must not intersect when shifted 5 mm. With this constraint, as well as the GFQ and x_{gfr} constraints, it is now possible to employ the machinery developed in Section 3.3 to design a pole face which fulfills these requirements while minimizing the width of the magnet. A 7 cm wide pole piece with pole face defined by

$$y = \pm(2.73 - 0.0237x^2), \tag{3.24}$$

with x and y in units of cm, was found to be the best parabolic solution, shown in Figure 3.12 along with the unshifted and 5mm shifted beam pipe locations; there is a minimum of 1.5 mm of clearance to allow for installation and alignment. Although marginally better performance was possible using the spline profiles discussed in the previous section, a parabolic face was chosen to simplify fabrication and avoid any issues of saturation at sharp points, especially relevant given the sub-optimal steel available for yoke fabrication. This design gave a GFQ of $10^{3.3}$ and an $x_{\text{gfr}} = 13.3$ mm. In the bending plane, the GFQ as a function of x is shown in Figure 3.13 and the full 2D relative field error is shown in Figure 3.14.

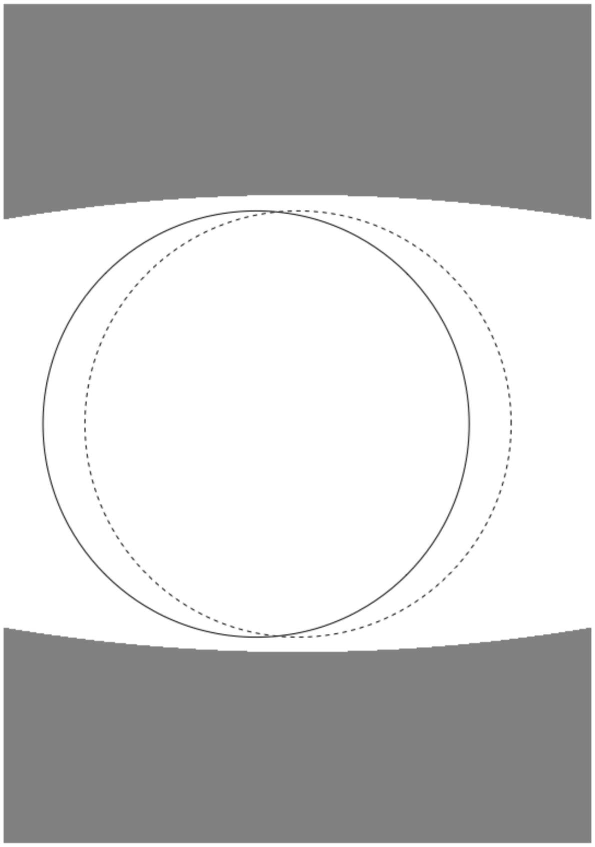

Figure 3.12: Pole faces relative to 5 mm shifted (solid) and unshifted (dashed) 2 inch diameter beam pipes.

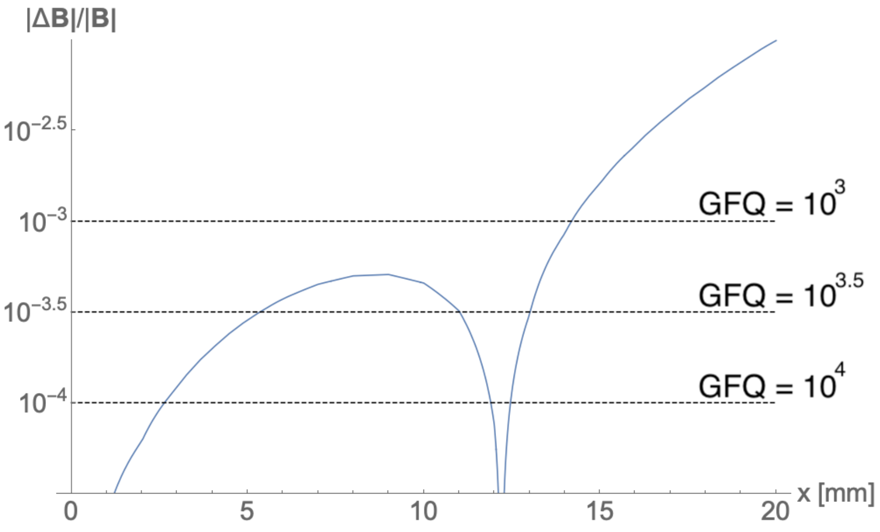

Figure 3.13: UCLA-LBNL chicane dipole, relative field error on axis. GFQ levels from previous section shown as dotted lines.

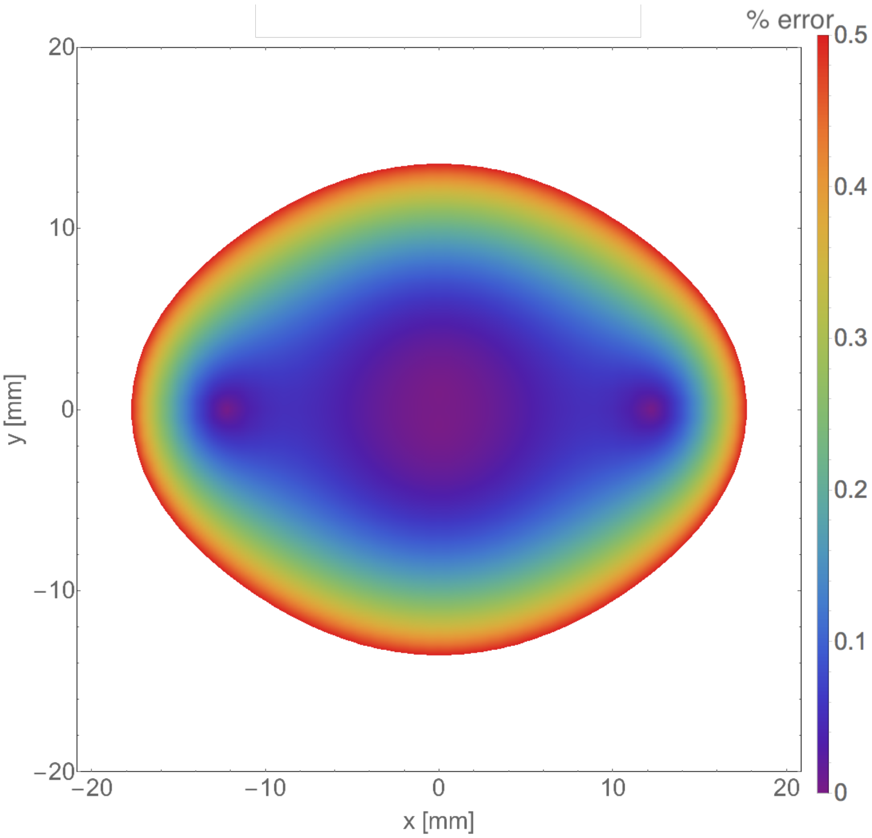

Figure 3.14: UCLA-LBNL chicane dipole, relative field error.

3.4.3 Magnetic circuit analysis

Now that the gap and maximum magnetic field are known, basic magnetic circuit rules [81] can be used to get a first order estimate of the required coil specifications. The magnetomotive force (MMF), $\mathcal{F}$, is defined as

$$\mathcal{F} = \oint \mathbf{H} \cdot \mathrm{d}\mathbf{l}, \tag{3.25}$$

i.e. the integration of $\mathbf{H}$, magnetic field strength, around a loop. If the source of MMF for is a coil of wire then $\mathcal{F} = NI$ where N is the number of turns and I is the current per turn. In analogy to electrical circuits, this can be thought of as a voltage source. Continuing the analogy, *reluctance*, $\mathcal{R}$, is to a magnetic circuit what resistance is to an electrical circuit. Then the equivalent of Ohm's law is

$$\mathcal{F} = \Phi \mathcal{R}, \tag{3.26}$$

where Φ is the magnetic flux defined

$$\Phi = \iint_S \mathbf{B} \cdot \mathrm{d}\mathbf{S}, \tag{3.27}$$

If the flux in a region is oriented perpendicularly to a plane with area A and $B \equiv |\mathbf{B}|$ then $\Phi = BA$. The flux density, $\mathbf{B}$, at any point in the magnetic circuit will be given by

$$\mathbf{B} = \mu \mathbf{H}, \tag{3.28}$$

where μ is the permeability at that point in the circuit.

In parallel to the concept of resistivity in electrical circuits, if the magnetic flux is "flowing" through a volume of constant permeability then the reluctance associated with that region is

$$\mathcal{R} = \frac{l}{\mu A}, \tag{3.29}$$

with l being the length of the element, μ is its permeability, and A is its cross sectional area relative to the flux vector.

Reluctances have the same rules for combining as resistances, i.e. circuit elements in series have their reluctances added while elements in parallel have an inverse reluctance equal to the sum of inverse reluctances. For the dipole magnets, the total circuit reluctance can be thought of as two elements in series: the yoke reluctance, $\mathcal{R}_{\text{yoke}}$, and the gap reluctance $\mathcal{R}_{\text{gap}}$. This gives total reluctance $\mathcal{R}_{\text{total}} = \mathcal{R}_{\text{yoke}} + \mathcal{R}_{\text{gap}}$. For typical yokes, constructed of soft ferromagnetic materials, the permeability of the yoke material will be thousands of times higher than vacuum permeability, μ_0. A standard approximation is therefore that $\mathcal{R}_{\text{total}} \approx \mathcal{R}_{\text{gap}}$. Combining equations 3.25 and 3.26 gives

$$NI = \mathcal{R}\Phi, \tag{3.30}$$

and making substitutions from equations 3.27 and 3.29

$$NI = \frac{l}{\mu A} BA = \frac{lB}{\mu}. \tag{3.31}$$

Plugging in the gap size for l (0.054 m), vacuum permeability μ_0 for μ, and the maximum field for B (0.26 T) gives an estimate of the MMF required to drive this dipole: 11,700 amp-turns.

3.4.4 Coil design

For simplicity, it was decided that these dipoles should be passively air cooled, rather than using water or forced air cooling. Passive cooling requires a current density of less than 150 amps per centimeter squared [82]. Therefore, to achieve $\mathcal{F}$ = 11,700 amp-turns will require approximately 78 cm^2 of coil cross sectional area per dipole. If a symmetric design is used, employing two coils per dipole, this amounts to about 40 cm^2 per coil. Bearing in mind the L_{out} design spec of 30 cm along with the yoke length of 17.5 cm, a coil thickness of 5 cm will leave $L_{\text{out}} - L_{\text{yoke}} - 2 \times L_{\text{coil thickness}} = 2.5$ cm between dipoles for installation and adjustment.

To get the required 40 cm^2 per coil the coils must therefore each be 8 cm tall.

Up until now, only the mechanical features of the coils have been considered. The actual winding of the coils will be contingent on the power supplies as well as manufacturability considerations. For the chicane, two power supplies were already on hand at LBNL, removing that degree of freedom. The power supplies are bipolar with voltage output from -50 to 50 volts and current output of -20 to 20 amps (Kepco BOP 50-20GL [83]). Each supply will drive a pair of dipoles, one for the inner pair and one for the outer pair. To ensure consistency, the four coils in each circuit will be wired in series to ensure every coil passes the same current.

To a first order approximation, the volume of the coil, V_{coil}, will be equal to

$$V_{\text{coil}} = h_{\text{coil}}((l_{\text{pole}} + 2 \times t_{\text{coil}})(w_{\text{pole}} + 2 \times t_{\text{coil}}) - l_{\text{pole}} w_{\text{pole}}), \tag{3.32}$$

where h, l, w, and t correspond to height, length, width, and thickness respectively. The length of the wire per coil will be equal to the coil volume divided by the cross sectional area of the wire A_w. Using the standard equation for resistance, R, and making these substitutions, the resistance per coil can be calculated:

$$R = \frac{\rho l}{A_w} = \frac{\rho V_{\text{coil}}}{A_w^2} \tag{3.33}$$

where ρ is the resistivity of the wire and l is the length. Further, the number of turns, N, will be given by dividing the coil's cross sectional area by the wire's area: $N = A_c/A_w$. By holding $\mathcal{F} = NI$ fixed the current:

$$I = \frac{\mathcal{F}}{N} = \mathcal{F}\frac{A_w}{A_c} \tag{3.34}$$

and voltage (via Ohm's law $V = IR$):

$$V = IR = \left(\mathcal{F}\frac{A_w}{A_c}\right)\left(\frac{\rho V_{\text{coil}}}{A_w^2}\right) = \frac{\mathcal{F}\rho V_{\text{coil}}}{A_c A_w}. \tag{3.35}$$

Until now, all these equations have assumed that the coil's cross section and therefore volume have been completely filled by copper windings. However, this is not a good approximation for practical realizations of coils. Due both to the insulation on the wires and geometric limitations, there is a packing efficiency term, p, that must be applied to improve the approximation. This updates equation 3.34 to

$$I = \mathcal{F}\frac{A_w}{pA_c}. \tag{3.36}$$

Since I is linear with p and V_{coil} goes with the inverse of p, the packing efficiency term cancels out of equation 3.35.

Plugging in the values for these dipoles: $h_{\text{coil}} = 8$ cm, $l_{\text{pole}} = 17.5$ cm, $w_{\text{pole}} = 7$ cm, and $t_{\text{coil}} = 5$ cm, gives V_{coil} equals 2760 cm^3 by equation 3.32. $\mathcal{F}$ is taken to be $11700/2 = 5850$ amp-turns since each of the dipole's two coils will contribute half the MMF. Packing efficiency is estimated at 70% and ρ is set to the resistivity of copper, 1.7E-8 ohm-meter [84]. Equations 3.35 (multiplied by 4 to account for the 4 coils in series per power supply) and 3.36 are plotted in Figure 3.15. The vertical scales correspond to the current and voltage limits of the power supply.

The power supplies will be able to supply any coils comprised of wire with area between 5.5 and 9.6 mm^2. A standard wire gauge, AWG 9, sits near the middle of this range with a cross sectional area of 6.63 mm^2 [85]. According to the above approximations, this wire selection would supply the required MMF with 422 turns at 13.9 amps with a total voltage drop over 4 series coils of 41.4 V.

3.4.5 Thermal considerations

The total thermal power, P, dissipated in the coils is given by:

$$P = IV = \left(\mathcal{F}\frac{A_w}{pA_c}\right)\left(\frac{\mathcal{F}\rho V_{\text{coil}}}{A_c A_w}\right) = \frac{\mathcal{F}^2\rho V_{\text{coil}}}{A_c^2 p}. \tag{3.37}$$

With the values from above, this corresponds to a peak power draw of 143 watts per coil or 286 watts per dipole. Newton's law of cooling gives the rate of convective heat loss from an object to its environment as

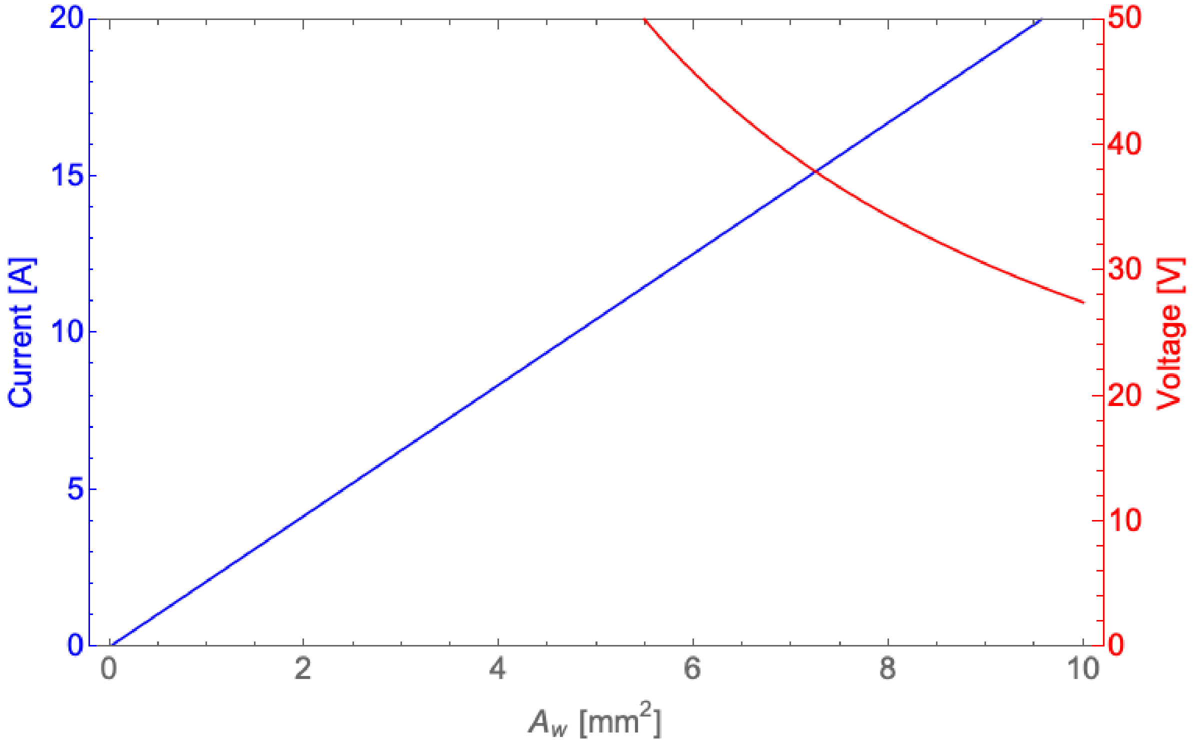

Figure 3.15: Current and voltage curves for four series coils as a function of wire area for UCLA-LBNL dipole parameters.

$$\frac{dQ}{dt} = -hA\Delta T(t), \tag{3.38}$$

where Q is heat, h is the heat transfer coefficient, A is the object's area, and ΔT is the difference in temperature between the object and its environment. In the case of the dipoles, they have a surface area exposed to atmosphere approximately equal to 0.3 m^2. The heat transfer coefficient between steel and non-forced air is approximately 15.8 W/(m^2 K) [86]. This suggests a worst-case, equilibrium ΔT for the dipoles of 60 C. This neglects any natural air currents, radiative heat transfer, and conduction to the base. The time-dependent temperature of the dipole is given by:

$$Q(t) = mCT(t), \tag{3.39}$$

where m is the mass of the object and C is the heat capacity. Therefore

$$mCT'(t) = Q'_{\text{input}}(t) + Q'_{\text{convection}}(t) = p - hA(T(t) - T_0), \tag{3.40}$$

where p is the electrical power and T_0 is both the ambient temperature and the initial temperature of the dipole. This gives

$$T(t) = \frac{p(1 - e^{\frac{-Aht}{Cm}})}{Ah} + T_0. \tag{3.41}$$

Assuming the dipole's heat capacity is approximately equal to mild steel, $C = 510$ J/(kg K), has a mass of approximately 100 kg, and is in a room with an ambient temperature of 23 C, the worst case temperature evolution of a dipole is shown in Figure 3.16. This suggests it takes approximately 10 hours of non-stop use at peak current to reach thermal equlibrium near 80 C.

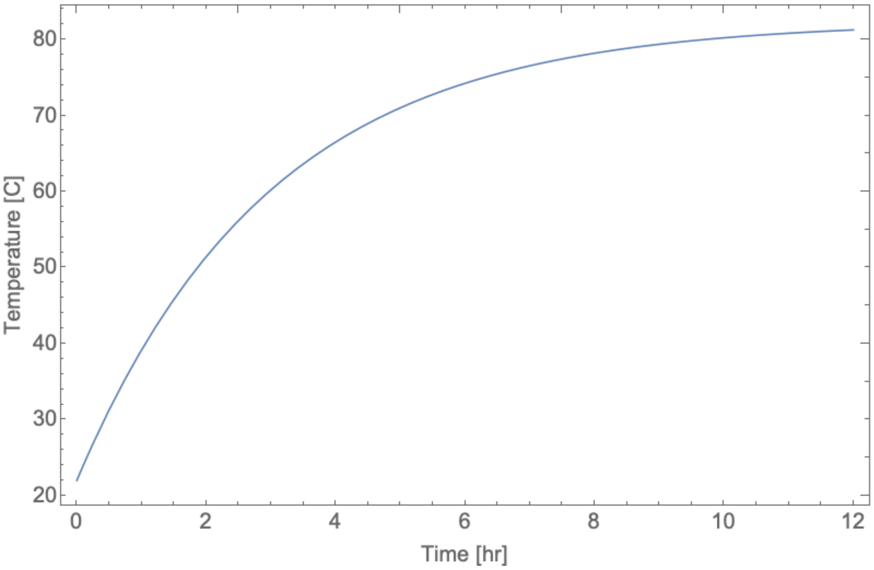

Figure 3.16: Worst case temperature over time of a UCLA-LBNL dipole at peak current.

3.4.6 Yoke magnetic properties

In a linear material, the permeability μ of a material defines the relationship between the induced magnetic flux density, B, by an external magnetic field, H, according to the relationship $B = \mu H = \mu_r \mu_0 H$ where μ_r is the relative permeability (compared to vacuum permeability, μ_0). Typical lists of relative permeability values give the material's performance at near-zero field, a poor approximation for most magnet yoke design. "Mu metal" is a commonly cited example of a very high permeability material, with $\mu_r > 50{,}000$ [87], but this value only holds for low magnetic fields, i.e. it *saturates* at low field and the linear approximation is invalid at higher fields. Therefore it is more instructive to consider μ_r not as a constant for a material but as a function dependent on B (or H).

A good yoke material will have a high μ_r out to a few times the peak gap field (fields in the yoke will generally be somewhat higher than the gap field). For many beamline magnets, a low carbon steel meets this requirement while also being relatively widely available for reasonable prices. Common low carbon alloys are 1008 and 1010 steel (~0.1% carbon content). An attempt was made to procure 1008 or 1010 steel for this project but, due to the dimensions required, no economical source was available. Therefore a somewhat worse material, 1018 steel (also called "mild steel") was investigated. 1018 steel is a very versatile and widely available steel on the consumer market with ~0.18% carbon content. Although it has a similar saturation field to 1008 or 1010 steel, its permeability below approximately 1.5 T is appreciably lower. The μ_r values can be extracted from published B-H curves [87]. The $\mu_r(B)$ curves of 1010 and 1018 steel as well as mu metal are shown in Figure 3.17. Observe the greater permeability of mu metal at low field but the rapid saturation. Over the range relevant for these magnets, approximately up to 1 T, 1010 steel has approximately 2 to 2.5× the permeability of 1018.

A high relative permeability, μ_r, material will permit the use of a lower cross section yoke. Recall in section 3.4.3 that the approximation that $\mathcal{R}_{\text{yoke}} \approx 0$ permitted the easy calculation of the MMF required to drive the required field in the gap. As long as this approximation is satisfied, approximately the same number of amp-turns will be required. Recall that the flux, Φ, from equation 3.27, is taken as constant throughout the elements of the magnetic circuit. Therefore it can be said that

$$\Phi = B_g A_g = B_y A_y \tag{3.42}$$

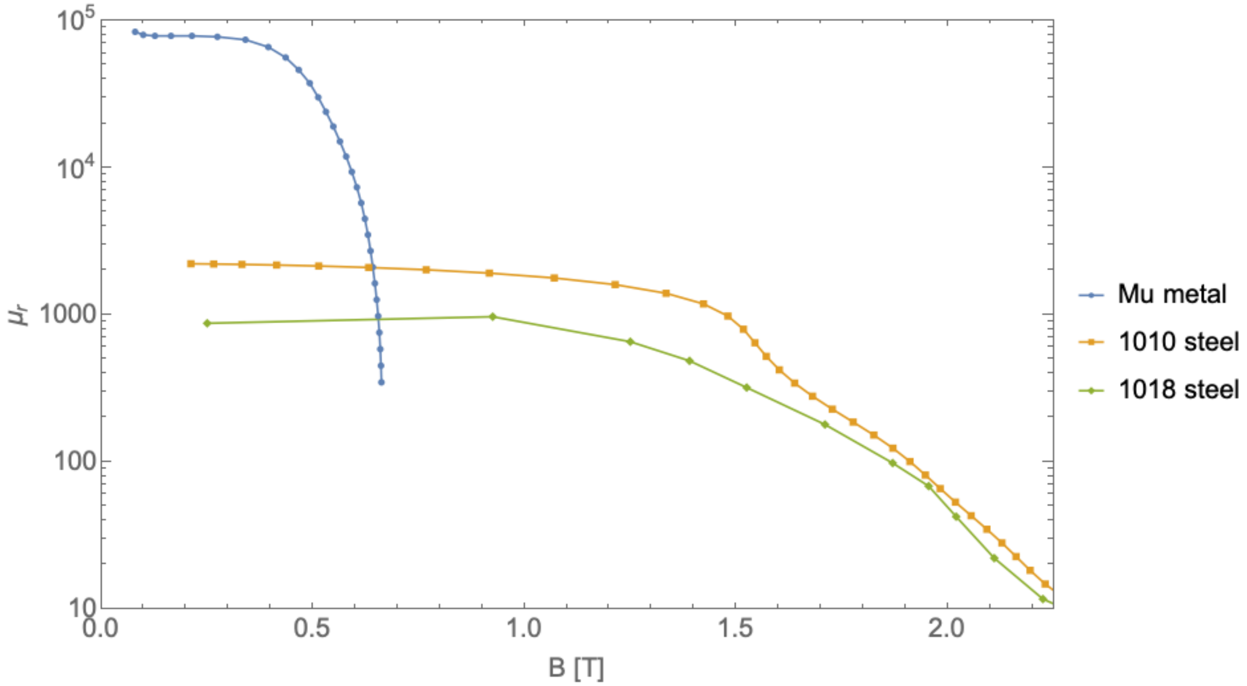

Figure 3.17: Relative permeabilities of mu metal, 1010 steel, and 1018 steel. Data from [87].

where B is the magnetic flux density in an element and A is the cross sectional area of the element, where subscripts g and y correspond to the magnet's gap and yoke respectively. Applying Hopkinson's law (Equation 3.26) and the additivity of reluctances,

$$\mathcal{F} = \Phi \mathcal{R}_T = \Phi(\mathcal{R}_g + \mathcal{R}_y), \tag{3.43}$$

to find the MMF, $\mathcal{F}$, required to achieve a desired magnetic flux given the circuit's total reluctance, $\mathcal{R}_{\mathcal{T}}$. Now apply equation 3.29 to express the reluctances based on the material dimensions and properties,

$$\mathcal{F} = \Phi \left(\frac{l_g}{\mu_0 A_g} + \frac{l_y}{\mu_0 \mu_r(B_y) A_y} \right), \tag{3.44}$$

where l is the length of a given circuit element and $\mu_r(B_y)$ gives the permeability of the yoke material as a function of the magnetic flux density in the yoke, B_y. This is an approximation that assumes the yoke cross sectional area is constant throughout the circuit. Φ will be defined by the required gap field and area, $\Phi = A_g B_g$, and B_y can be calculated based on the conservation of flux, $B_y = \Phi/A_y$:

$$\mathcal{F} = B_g A_g \left(\frac{l_g}{\mu_0 A_g} + \frac{l_y}{\mu_0 \mu_r(\frac{B_g A_g}{A_y}) A_y} \right). \tag{3.45}$$

Using the parameters for the UCLA-LBNL dipoles ($A_g = 7 \times 17.5 = 122.5$ cm^2, $B_g = 0.26$ T, $l_g = 5.4$ cm, $l_y = 65$ cm) the MMF required given the yoke area can be computed given the $\mu_r(B)$ curve of the material. This is shown in Figure 3.18 for 1010 and 1018 steel as well as for an idealized, infinite permeability yoke. A yoke cross section of 43.75 cm^2 was used for the UCLA-LBNL dipoles, requiring an estimated 12,060 amp-turns to drive (3% higher than the 11,700 amp-turns from section 3.4.3 based on an infinitely permeable material). If 1010 steel was used, the cross section of the yoke could be reduced to 28.1 cm with no reduction in magnetic performance. Constructed from 1018 steel, the yoke (excluding pole pieces) per dipole weighs approximately 35 kg (75 lb); using 1010 steel would have reduced the weight to 21 kg (47 lb).

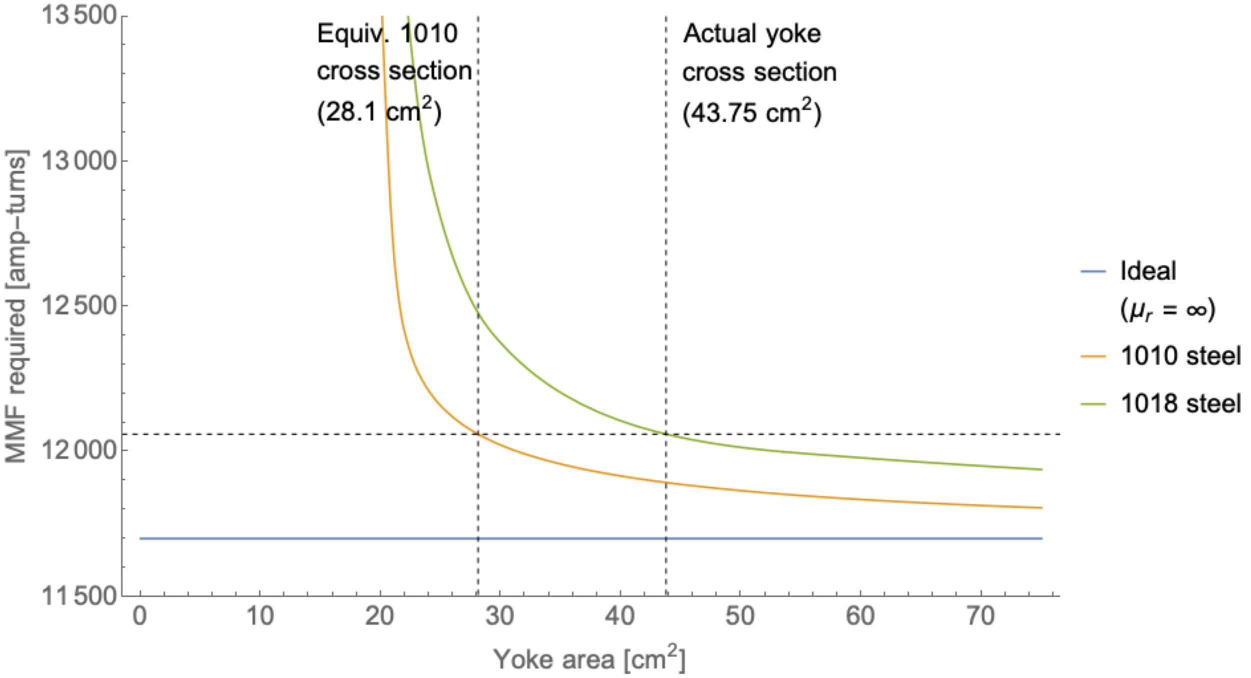

Figure 3.18: Comparing the MMF required to achieve the required magnetic field specs, given the geometry of the UCLA-LBNL dipoles, as a function of yoke cross sectional area.

3.4.7 Mechanical considerations

It is important to have magnets that are physically strong enough to avoid distortion when loaded by the magnetic fields. If fringing fields are ignorable, the approximate pressure, P_{mag}, on the pole tips is given by [26]:

$$P_{\text{mag}} = \frac{B^2}{2\mu_0}. \tag{3.46}$$

So for these magnets, the peak magnetic pressure with $B = 0.26$ T is 28,200 Pa (4.1 PSI). With pole face area equal to 17.5 cm × 7 cm = 122.5 cm^2, this is approximately 345 N (77 lb-f) of attraction between the pole tips. The effect of this force was modeled using finite element analysis (FEA) in Solidworks on a yoke comprised of 1018 steel. The displacement (at a 62,000× exaggerated scale) is illustrated in Figure 3.19. The maximum displacement of any point is less than one micron which is well within the design tolerances.

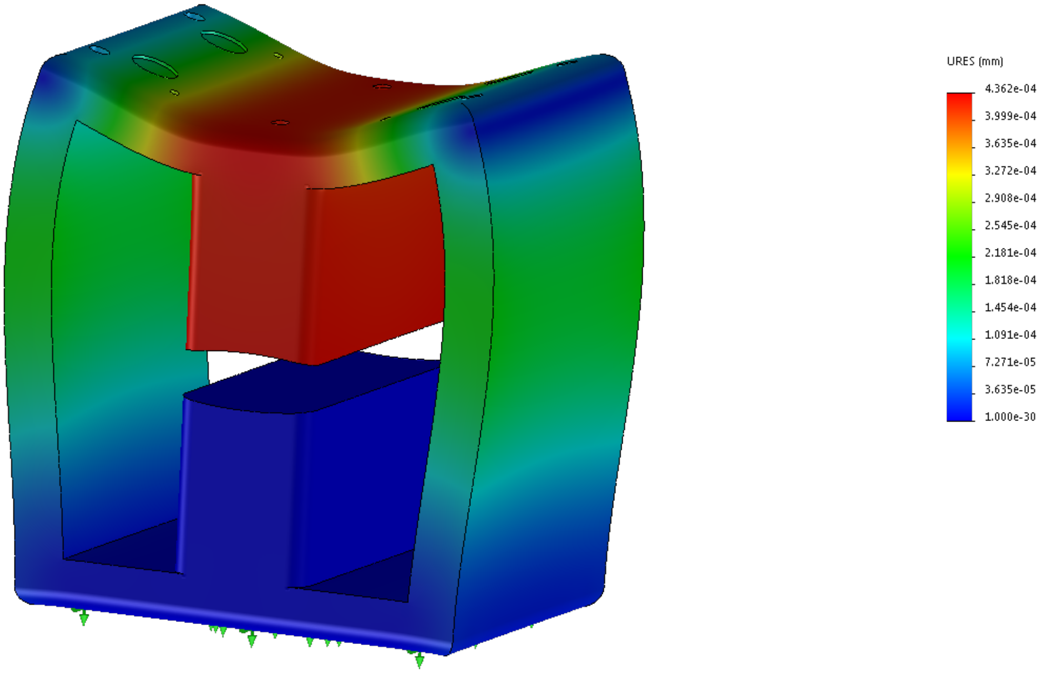

Figure 3.19: FEA model of displacement under peak magnetic pressure load with a 62,000× exaggerated scale. Coils have been omitted for clarity.

3.4.8 Residual dispersion

An important consideration when deciding the tradeoff between pole width and tolerable deviation from an ideal chicane field is the residual dispersion. Due to the non-ideal fields, beam particles with energies higher or lower than the design energy will experience net kicks in both position and angle as a function of this energy spread, termed residual dispersion. Position dispersion, η_x, is defined as $\frac{\Delta x}{\Delta\gamma/\gamma_0}$, and angular dispersion, $\eta_{x'}$, is defined as $\frac{\Delta x'}{\Delta\gamma/\gamma_0}$. These terms can lead to emittance growth, $\Delta\epsilon_{\text{geo},x} = (\sigma_x + |\frac{\sigma_\gamma}{\gamma_0}\eta_x|)(\sigma_{x'} + |\frac{\sigma_\gamma}{\gamma_0}\eta_{x'}|) - \epsilon_{\text{geo},x}$. This impact is minimized when $\sigma_x = \sigma_{x'}$ and $\eta_x = \eta_{x'}$.

In the Radia model, the outer coils were set to a current density and the inner coils were tuned to minimize residual dispersion for design energy beams for a given R_{56} value (typically the inner coil current is equal to the negative of the outer coil current to within less than one part in a thousand). The dispersion curves and associated emittance growth for a beam with a normalized emittance of 100 nm-rad with 1% spread are shown in Figure 3.20. The expected operational R_{56} values are shown for 100 and 250 MeV beams with dipoles 1 and 4 centered on axis; the dispersion has been deemed acceptable [55]. By translating the whole chicane horizontally, the energy of the zero crossing can be changed. Therefore, after operation with the ∼100 MeV jet LPA is complete, the chicane can be moved to minimize the emittance growth at the expected energy.

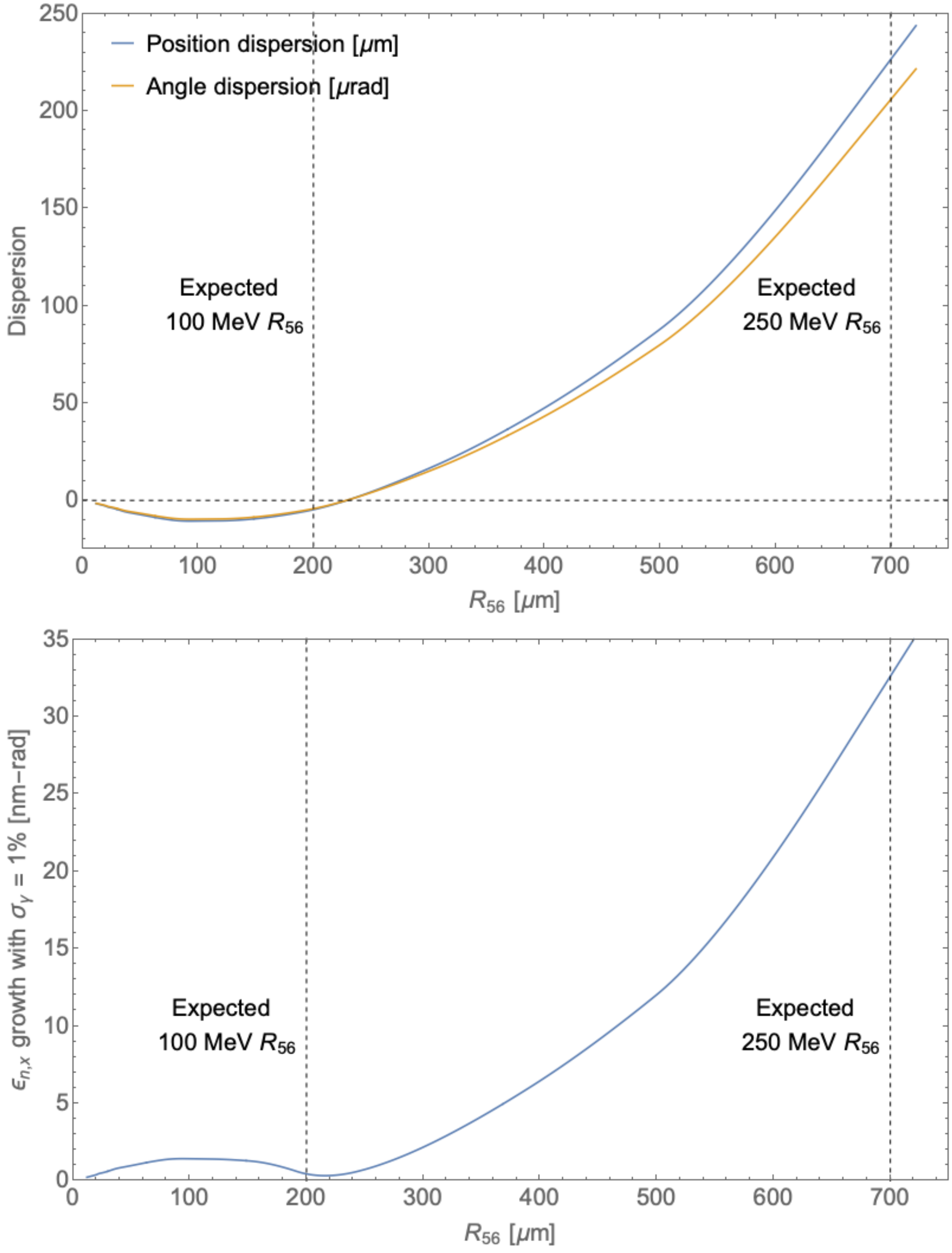

Figure 3.20: Position and angle dispersion curves for the full UCLA-LBNL chicane as a function of R_{56}. Minimized normalized emittance growth for a 100 nm-rad beam with 1% energy spread is also shown as a function of R_{56}.

3.4.9 Design evolution

The earliest design iteration of the UCLA-LBNL chicane considered the use of permanent magnets with a variable gap yoke instead of electromagnetic coils. The benefit of permanent magnets was a significantly smaller footprint, cost savings on power supplies (it was not known at the time that two Kepco 50-20GL supplies would be available for free, saving over \$30,000), and having an entirely *in vacuo* chicane, permitting a smaller magnet gap by removing the need for a beam pipe. Such a design would not be possible to "turn off" though, requiring a way to shift the entire chicane assembly off the beam path for dispersion-free operation. A concept design is rendered in Figure 3.21. Each of the four dipoles has a mechanically adjustable gap, controlled by a stepper motor driven ball screw. The entire chicane can be shifted out of the beam path by two additional ball screws.

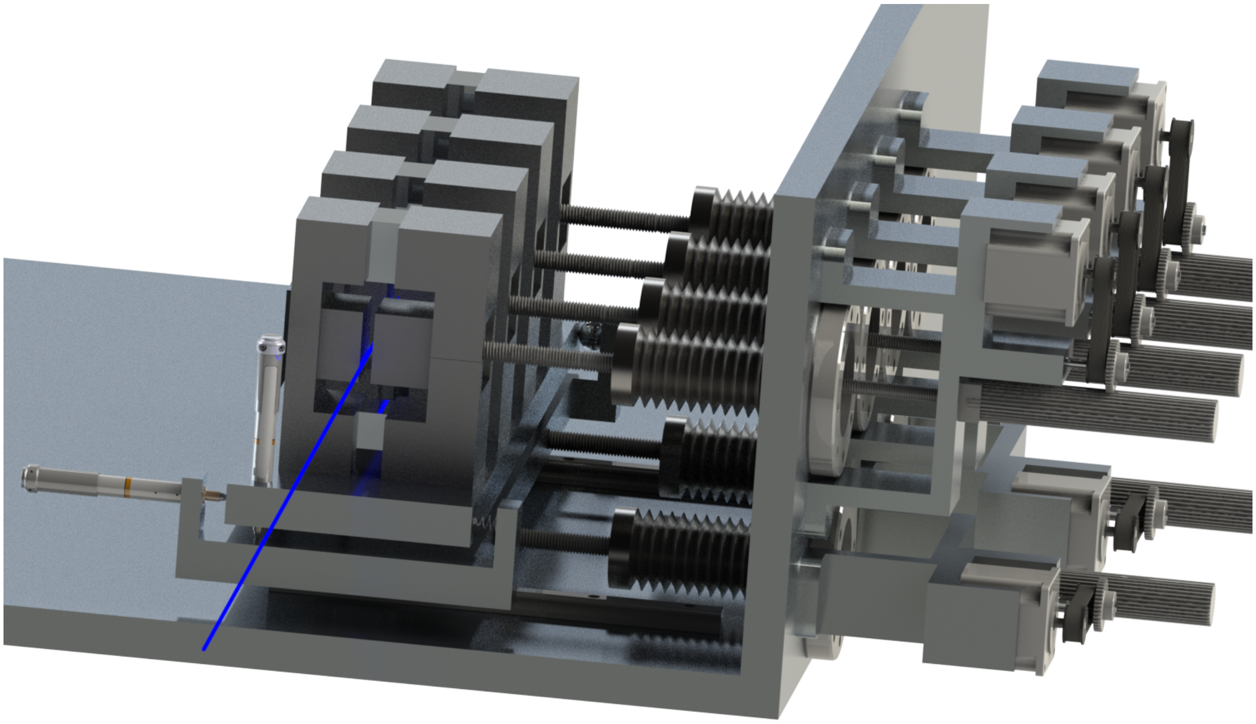

Figure 3.21: A concept design of an early, permanent magnet version of the UCLA-LBNL chicane. The blue line represents the beam axis.

The permanent magnet approach was ultimately abandoned due to the mechanical complexity and a more conventional electromagnetic chicane was considered. The first iteration was a so called C-magnet. This asymmetric design requires a more complicated approach to pole face optimization to counteract multipole modes that would otherwise be forbidden in symmetric magnets. A benefit though is that the open side gives easy access to the gap volume for probing. Additionally, C-magnets can be driven by a single coil, reducing expense. The cantilevered position of the magnetic pressure requires a more rigid mechanical design to avoid deflection. An early version of the C-magnet was optimized up to the quartic term (plus 19^{th} and 20^{th} terms to round the corners); it achieved an average error in a 2 cm wide by 0.4 cm tall rectangle of 0.019%, shown in Figure 3.22. At this point, the pole faces were still quite large compared to the magnet gap (high aspect ratio). The design moved on from C-magnets before more extensive refinement could occur.

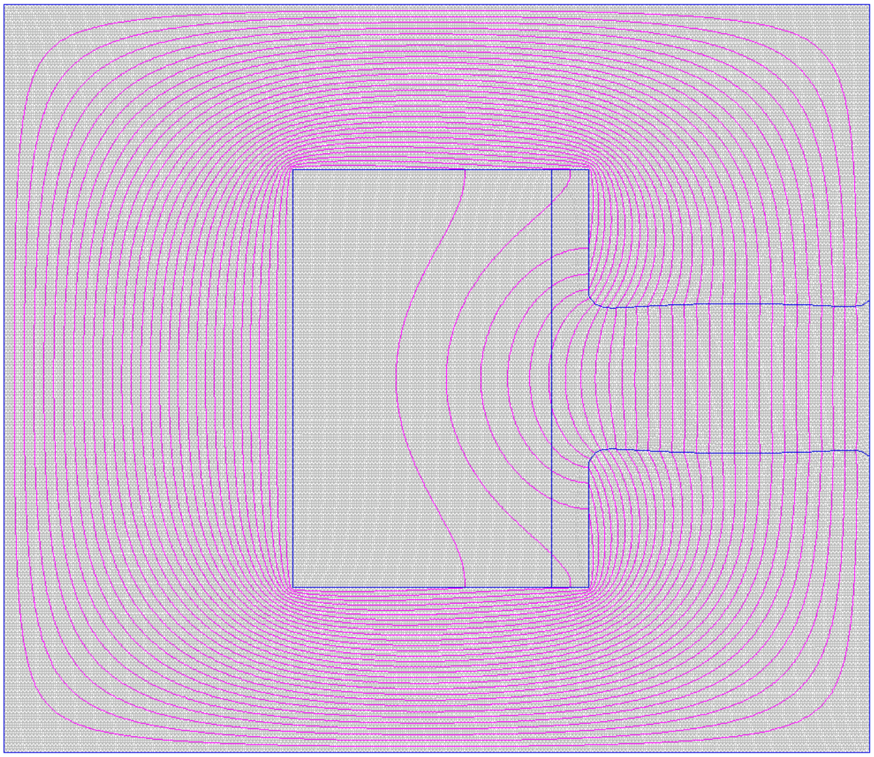

Figure 3.22: A Poisson simulation for a fourth order optimized C-magnet with a high aspect ratio.

The C-magnet design was discarded in favor of a symmetric H-magnet design. The H-magnet requires the use of two coils but has the benefit of having symmetric fields, requiring more straightforward optimization of the pole faces while also permitting the use of thinner pole pieces (lower aspect ratio). It also reduces the contribution of coil fields near the beam axis. A concept design for an H-magnet is rendered in Figure 3.23.

Figure 3.23: A concept design of an H-magnet for the UCLA-LBNL chicane.

The final design was a variant of the initial H-magnet: the stacked H-magnet. Although similar, the stacked H-magnet requires a taller (and heavier) pole piece as well as introducing stronger coil-based fringe fields. However, in the context of this experiment, it has the important benefit of having a smaller footprint. The final design for the chicane, using stacked H-magnets, is shown in Figure 3.24. Table 3.4 is a summary of the pros and cons of the different geometries considered.

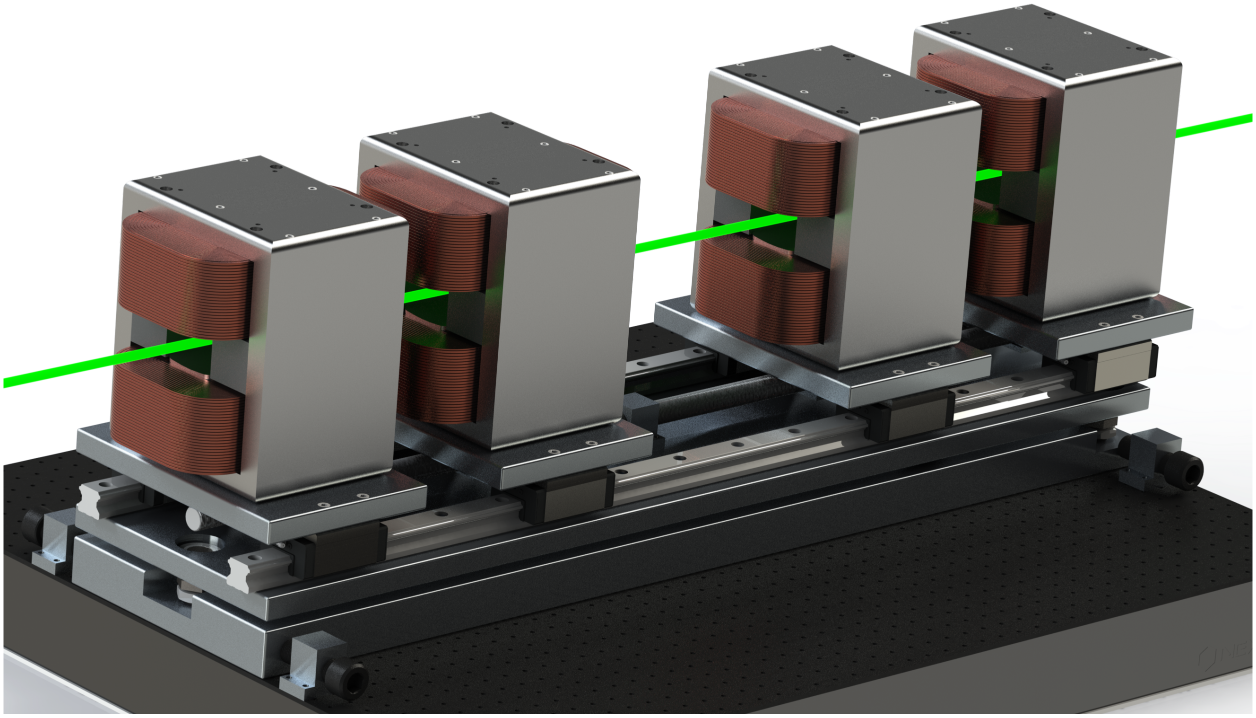

Figure 3.24: The final design for the dipoles, shown as the assembled chicane, including kinematic stage.

Table 3.4: Comparison of the different dipole configurations considered

Geometry	**Pros**	**Cons**
Permanent magnet	Compact footprint Cost savings on power supplies	Mechanical complexity
C-magnet	Easy probe access to gap volume Driven by single coil	Asymmetric pole face Requires more rigid design
H-magnet	Symmetry simplifies design Short pole piece reduces weight Low impact from coil fields	Large per-dipole footprint
Stacked H-magnet	More compact per-dipole footprint	Larger pole piece Greater coil field contribution

3.4.10 Design summary

Table 3.5: Summary of UCLA-LBNL chicane design parameters

Parameter	**Value**
Peak R56	1 mm
Yoke length	17.5 cm
Peak field	0.26 T
Gap aperture	5.4 cm
Field quality (GFQ)	$10^{3.3}$
Field region (x_{gfq})	13.3 mm
MMF (optimal)	11,700 amp-turns
Peak current density	150 A/cm^2
Per coil cross section	40 cm^2
Wire cross section	6.6 mm^2 (AWG 9)
Turns per coil	415
Peak current per coil	13.9 A
Peak voltage per coil	10.4 V
Worst case temperature rise	60 K
Yoke material	1018 steel
Yoke cross section	43.75 cm^2
Force induced deflection	$\leq$0.4 μm

3.5 Chicane fabrication and commissioning

3.5.1 Yokes

The yokes of the magnet were designed in 6 major parts: 2 side plates, 2 pole pieces, a top plate, and a bottom plate. The original, un-edited blueprints used for fabrication are duplicated below:

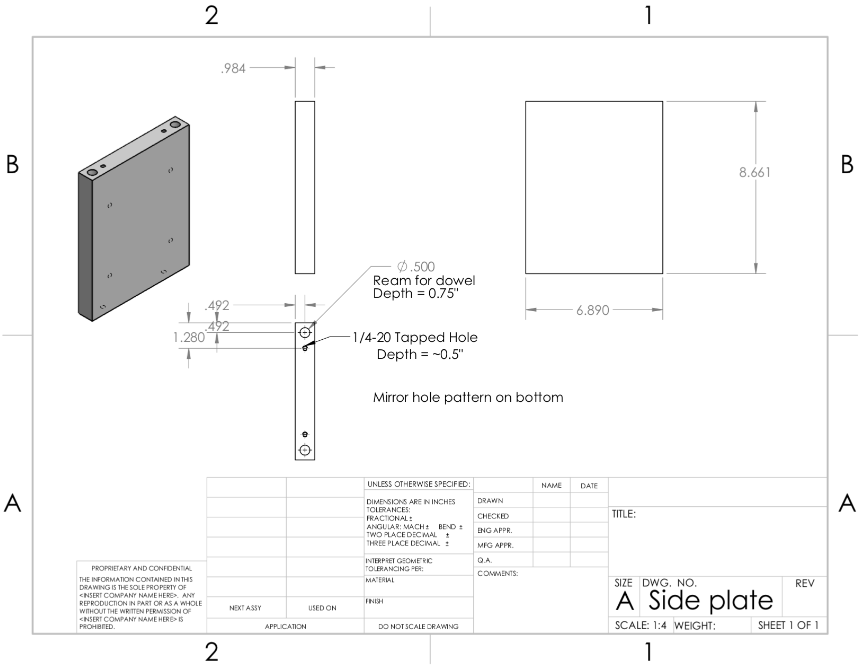

Figure 3.25: Original side plate blueprint for fabrication.

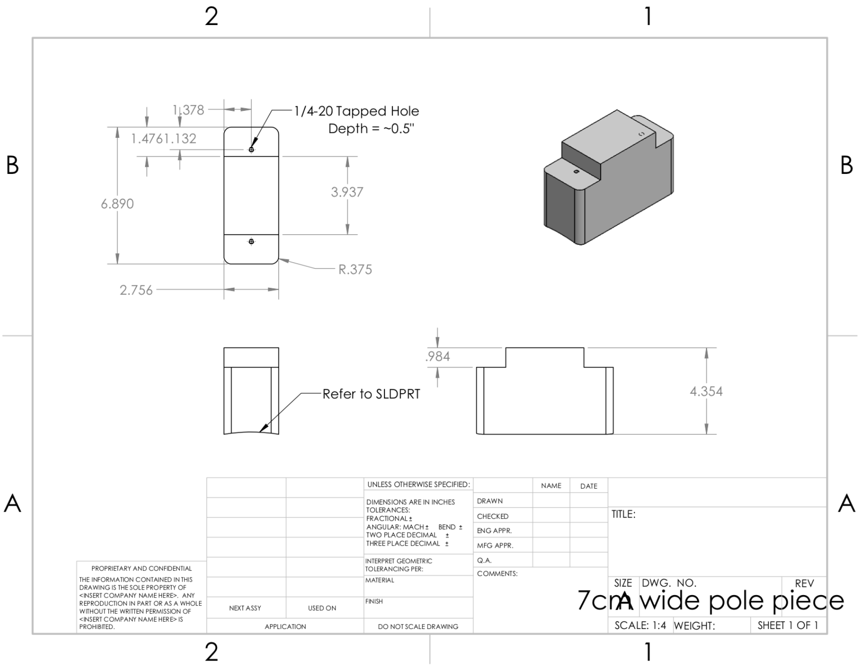

Figure 3.26: Original pole piece blueprint for fabrication.

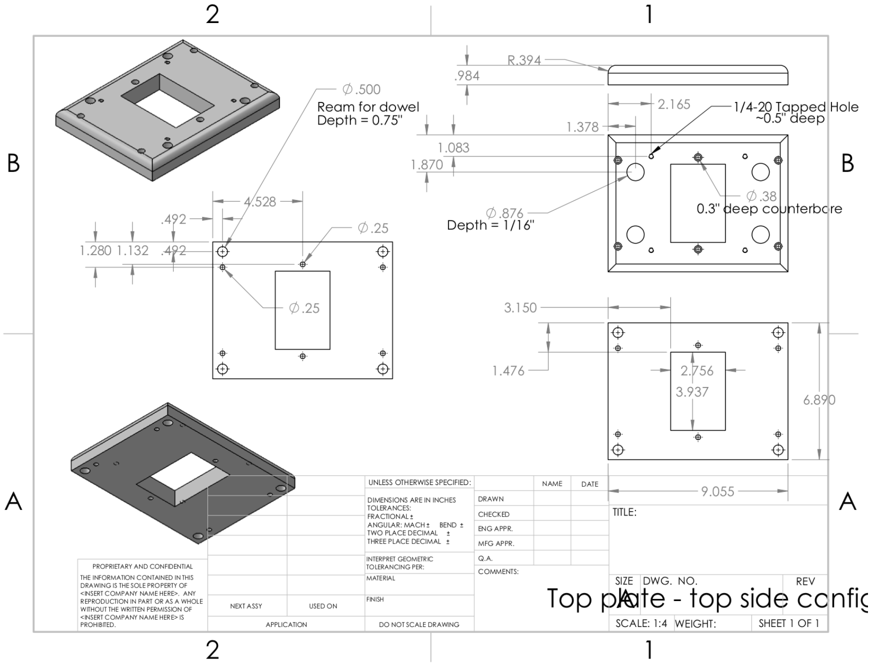

Figure 3.27: Original top plate blueprint for fabrication.

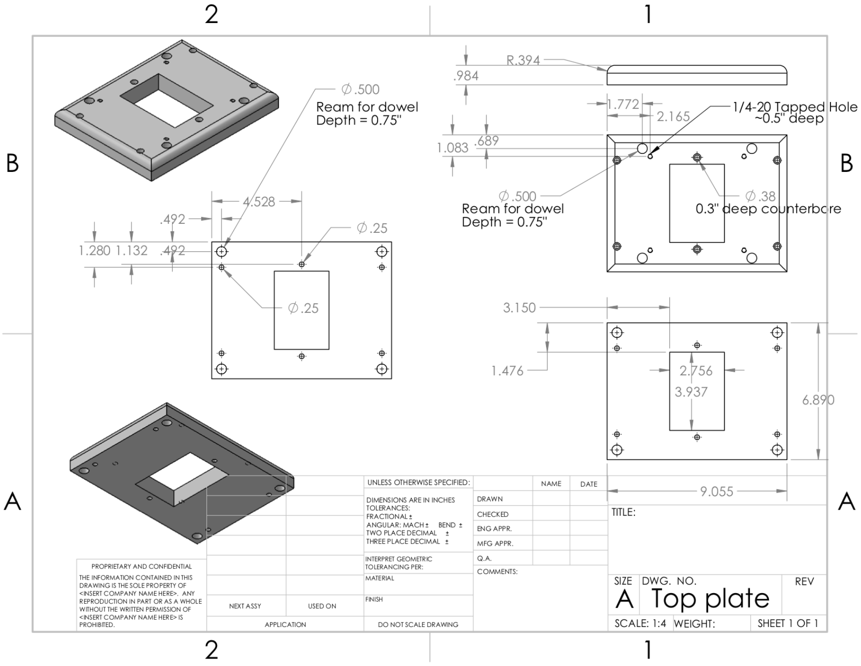

Figure 3.28: Original bottom plate blueprint for fabrication.

All the parts were made from 1018 steel from DiscountSteel.com. For the side, top, and bottom plates blocks with dimensions 1" × 7" × 10" were purchased (16× at \$58.55/ea) while for the pole pieces blocks with dimensions 3" × 5" × 8" (8× at \$104.79/ea) for a total cost of \$1,775.12. These parts were all in a rough cut state and sent to Bourdelais Grinding where they were brought to final dimension to high tolerance (critical dimensions specified to ±0.001") by Blanchard grinding for a total job cost of \$1,608.40. The UCLA Physical Sciences Machine Shop then performed other operations on the pieces:

- Holes were drilled, tapped, and counterbored
- Precision holes for dowels were drilled and reamed on the top, bottom, and side plates
- The top and bottom plates were wire EDM'd to create a highly precise (-0/+0.001") cutout for the pole piece to index into
- Pockets for fiducial nests were milled
- Edges were chamfered

- The pole pieces were CNC machined using a ball nose endmill to create the pole face profile

Along with the fabrication of the kinematic mount (discussed below) the machine shop billed 330 hours for this work at a cost of \$16,915.80. Since 1018 is a non-stainless steel, these parts would rapidly rust if exposed to air, possibly causing the binding of the tightly fit parts. To avoid this, the parts were sent to Barry Avenue Plating to be electroless plated in nickel to a thickness of 0.0003" (8 micron) for a total job cost of \$450.00. This was a compromise between cost while maintaining minimal plating thickness: at only 8 microns thick, the coating should not significantly affect the tolerances of the parts.

3.5.2 Coils

The coils were fabricated by Custom Coils, Inc.. They are constructed from 415 turns of square conductor, 9 AWG copper wire and enclosed in polyimide tape (commonly referred to as its genericized trademark, "Kapton"). The total job cost for the 8 coils was \$13,230.00.

3.5.3 Kinematic mount

A kinematic mount was designed to allow the precision alignment and long term stability of the chicane relative to the beamline (See Figure 3.24). All 6 degrees of freedom (DoF) can be adjusted: X (transverse), Y (vertical), and Z (longitudinal) translation as well as roll, pitch, and yaw rotations. The mount consists of two large aluminum plates 48" × 12" × 1" or 2" thick for the top and bottom plate respectively. Three tapered roller bearings were press fit into the top plate and the lower plate was threaded. Custom threaded adjusters seated into the thrust bearings and threaded into the top plate. This allowed the top plate to be adjusted relative to the bottom plate in Y translation as well as roll and pitch rotations. Onto the top plate a pair of precision linear rails are installed. These rails are for use with linear bearing carriages and are rated to maintain parallelism to within 15 microns over their 4 foot length. Aluminum carrier plates were machined with a hole pattern to register and mount the dipoles with screws and precision dowel pins with connections for a pair of these linear bearings. A long stainless steel threaded rod is fixed above the top aluminum plate and it runs through arms under each carrier plate. This allows the carrier plates, and therefore dipoles, to be independently positioned along the length of the kinematic mount (Z translation). Finally, the entire assembly is placed directly onto an optical table in the beamline. Threaded blocks are mounted to the optical table with transverse screws, pushing on the lower aluminum plate, allowing the entire assembly to be adjusted in the X translation and yaw rotation DoFs. Once aligned, the kinematic mount can be clamped to the optical table and jam nuts can lock the adjustment of the remaining DoFs.

The most expensive material components were: 2 precision rails for \$1,100, 8 linear bearings for \$1,500, and the 2 large aluminum plates cost \$900. These, along with other miscellaneous components brought the material cost of the kinematic mount to approximately \$4,500. As noted above, the combined machining of the dipoles and mount by the UCLA Physical Sciences Machine Shop cost \$16,915.80.

3.5.4 Expense summary

Table 3.6: Summary of expenses for UCLA-LBNL chicane

Item	**Cost**
Dipole steel	\$1,775.12
Blanchard grinding	\$1,608.40
Nickel plating	\$450.00
UCLA Physical Sciences Machine Shop	\$16,915.80
Coils	\$13,230.00
Mount material cost	\$4,500.00
Total	\$38,479.32

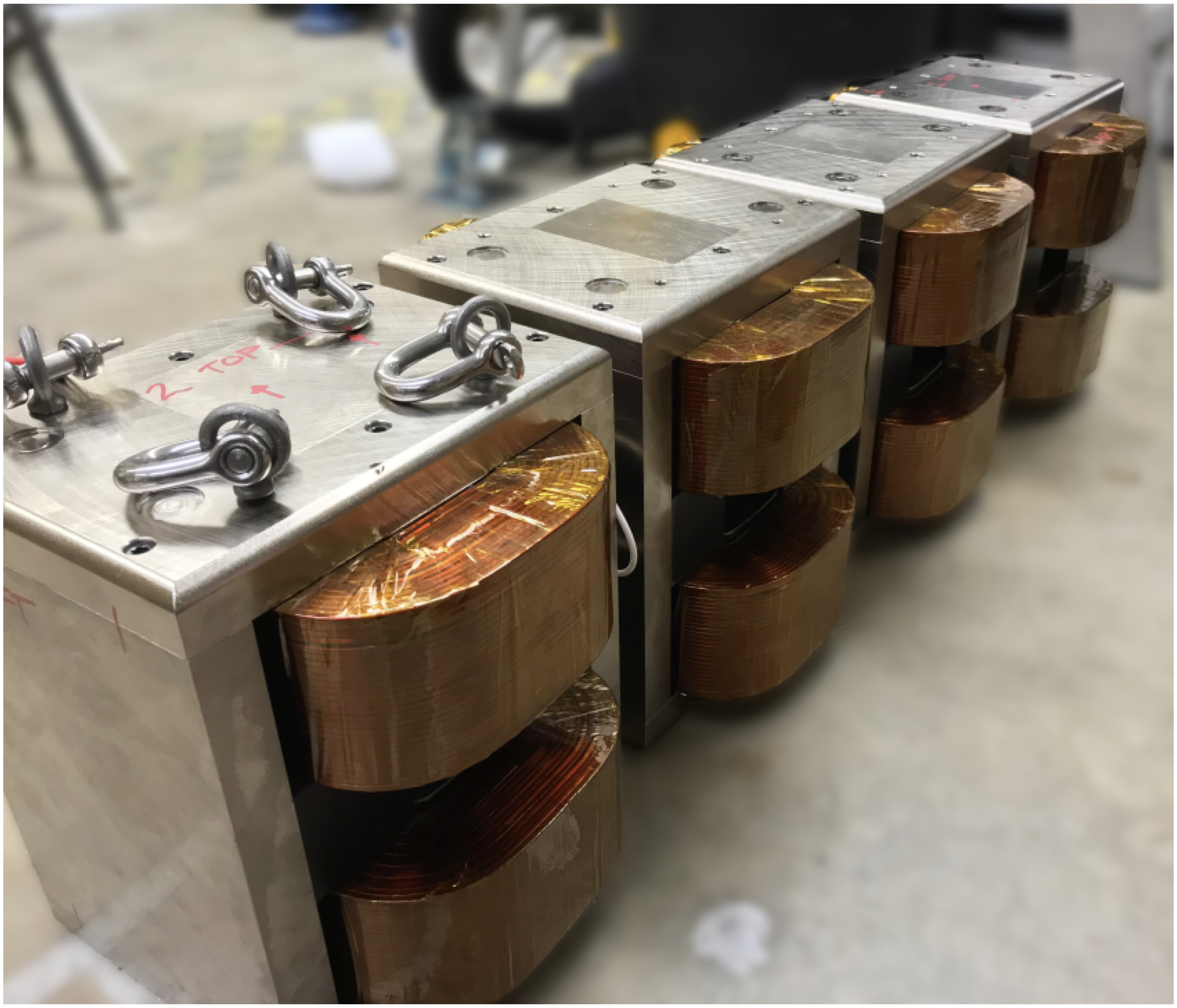

Figure 3.29: Assembled UCLA-LBNL dipoles.

3.5.5 Field quality measurements

The dipoles were assembled at UCLA (Figure 3.29) and their fields were characterized using a MMT-6J08-VG transverse Hall probe and a Lake Shore 421 gaussmeter from Lake Shore Cryotronics Inc., and a purpose built, 3D gantry system. These 3D field maps were compared to Radia [88] simulation fields to ensure agreement. The vertical field of a dipole magnet was measured in a square region with side lengths of 6 mm, over a total length of 375 mm, centered at the dipole center. The step size for this scan was 1 mm. Although the probe gantry was aligned to the dipole to the extent possible, small errors existed so 6 free variables were permitted to transform the gantry coordinate system to the magnet coordinate system to minimize the error between the simulated model and the measured fields. Define the following rotation matrices:

$$\begin{aligned}\mathbf{R}_x(\delta_\alpha) &= \begin{pmatrix} 1 & 0 & 0 \\ 0 & \cos(\delta\alpha) & -\sin(\delta\alpha) \\ 0 & \sin(\delta\alpha) & \cos(\delta\alpha) \end{pmatrix} \\ \mathbf{R}_y(\delta_\beta) &= \begin{pmatrix} \cos(\delta\beta) & 0 & \sin(\delta\beta) \\ 0 & 1 & 0 \\ -\sin(\delta\beta) & 0 & \cos(\delta\beta) \end{pmatrix} \\ \mathbf{R}_z(\delta_\gamma) &= \begin{pmatrix} \cos(\delta\gamma) & -\sin(\delta\gamma) & 0 \\ \sin(\delta\gamma) & \cos(\delta\gamma) & 0 \\ 0 & 0 & 1 \end{pmatrix}.\end{aligned} \tag{3.47}$$

Then the overall coordinate transform employed is:

$$\begin{pmatrix} x_f \\ y_f \\ z_f \end{pmatrix} = \mathbf{R}_z(\delta_\gamma)\mathbf{R}_y(\delta_\beta)\mathbf{R}_x(\delta_\alpha) \begin{pmatrix} x_i \\ y_i \\ z_i \end{pmatrix} + \begin{pmatrix} \delta_x \\ \delta_y \\ \delta_z \end{pmatrix}, \tag{3.48}$$

with fit parameters δ_x, δ_y, δ_z, δ_α, δ_β, and δ_γ. The mean average error (MAE) disagreement between the measured field and the Radia model, after normalizing both fields to their peak value, is minimized with parameters:

$$\begin{aligned} \delta_x &= -0.05\,\mathrm{mm} \\ \delta_y &= 0.86\,\mathrm{mm} \\ \delta_z &= -1.26\,\mathrm{mm} \\ \delta_\alpha &= -5.2\,\mathrm{mrad} \\ \delta_\beta &= 0.0\,\mathrm{mrad} \\ \delta_\gamma &= -15.5\,\mathrm{mrad} \end{aligned}. \tag{3.49}$$

Over the 13,500 mm^3 volume of interest, the MAE is found to be 0.20% of B_{peak}. The probe itself is rated for an accuracy of 0.15%, indicating excellent agreement between the physical dipole fields and the simulated model. Note that only the vertical field needs to be considered since, within the region of interest, the vertical field is over 99.9% of the overall field ($|B_y|/|\mathbf{B}| > 0.999$, $\forall \mathbf{x} \in$ region).

All of the dipoles were measured in this fashion and the on-axis fields are shown in Figure 3.30. The fields are so close as to be indistinguishable on this scale so Figure 3.31 shows the standard deviation of the four dipoles as a function of z, stdev($\{B_{y,1}[z], ..., B_{y,4}[z]\}$). The mean standard deviation over the measured length of the dipoles is $0.0013 \times B_{\text{peak}}$, suggesting a very high degree of uniformity between the four dipoles.

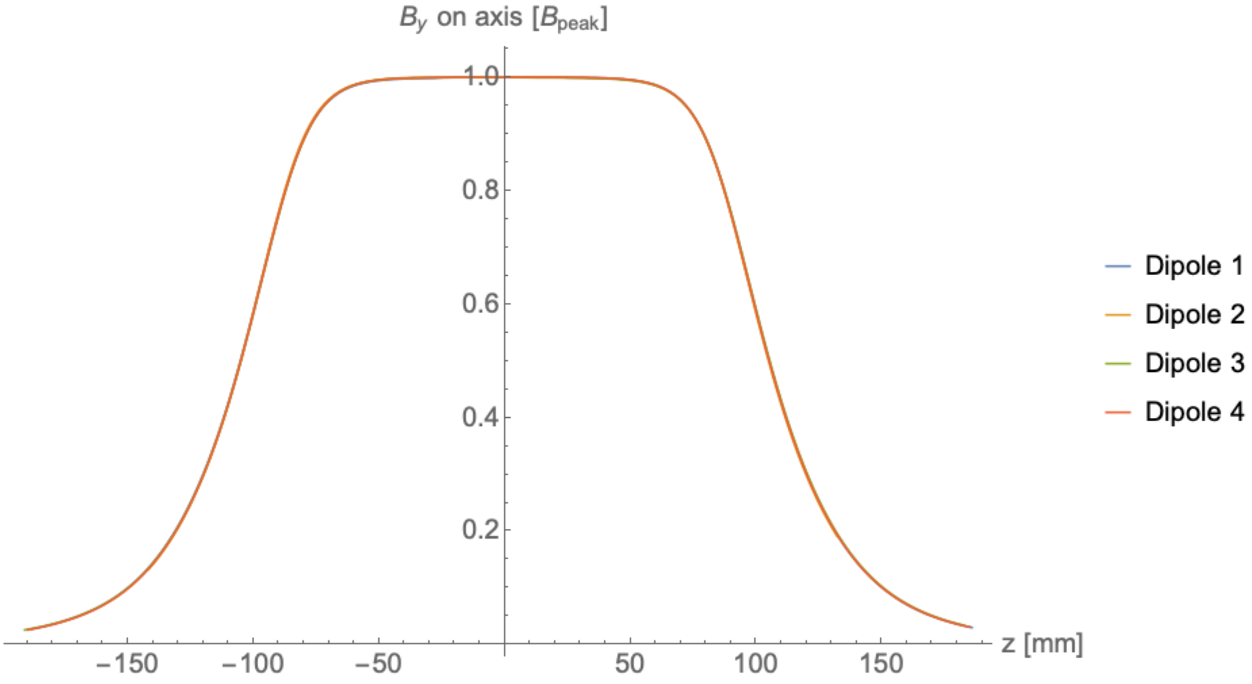

Figure 3.30: Measured on-axis B_y fields for all 4 UCLA-LBNL dipoles normalized to B_{peak}. All four curves are sufficiently similar as to be indistinguishable on this plot.

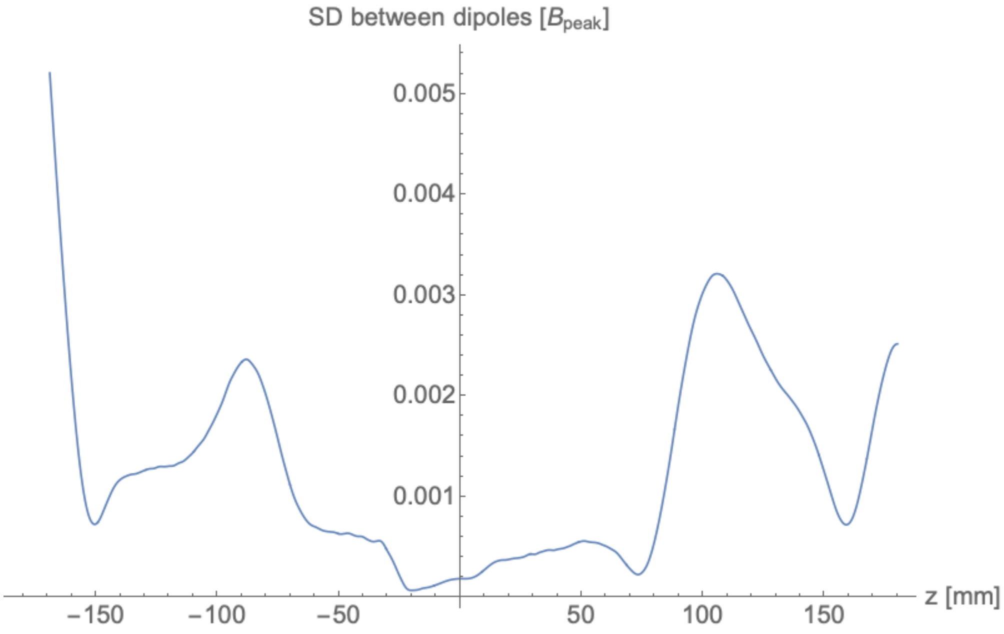

Figure 3.31: Standard deviation of B_y for all four UCLA-LBNL dipoles as a function of longitudinal position.

3.5.6 Current response measurements

The relationship between the supplied current and the magnetic field is also an important parameter to confirm experimentally. Since the dipoles have been designed to operate well below the saturation field of the yoke, the current response should be linear. The transverse Hall probe was centered in the dipole and the current was monotonically increased, starting from a degaussed yoke. The results are shown in Figure 3.32. A linear model with fixed zero intercept is fit via least-squares, giving $B[\text{mT}] = 17.96\, I[\text{A}]$ with an extremely high coefficient of determination, R-squared value, of 0.99994.

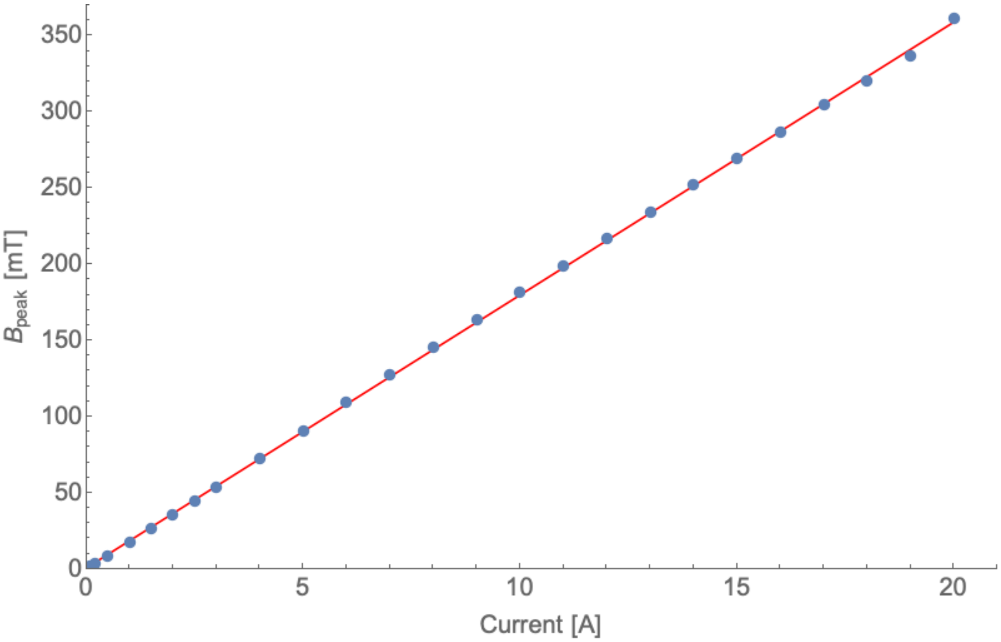

Figure 3.32: The magnetic field in the center of the dipole, B_{peak}, plotted as a function of current. Data in blue and a linear fit in red.

3.5.7 Degaussing

Due to the hysteresis of iron, in order to know the dipole field based only on the current (i.e. without a sensor for an active feedback loop) the magnet's current must be adjusted monotonically from a known magnetization. The easiest way to get to a known magnetization is by *degaussing*: applying a decaying field of alternating polarity. A degaussing profile given by V [volts] $= 25\cos(3.14\,t\,[\mathrm{sec}])\exp(-0.047\,t)$, applied for three minutes, was empirically found to reduce the residual field of the dipoles to less than 0.04 mT (less than the Earth's magnetic field of 0.06 mT).

3.5.8 Installation

The UCLA-LBNL chicane was shipped to LBNL and reassembled. It was surveyed with assistance from the ALS survey crew using a Leica laser scanner, fiducial markers, and an existing 3D model of the lab and beamline. The chicane was centered on the beam axis with a tolerance of less than 200 microns (0.008") (Figure 3.33).

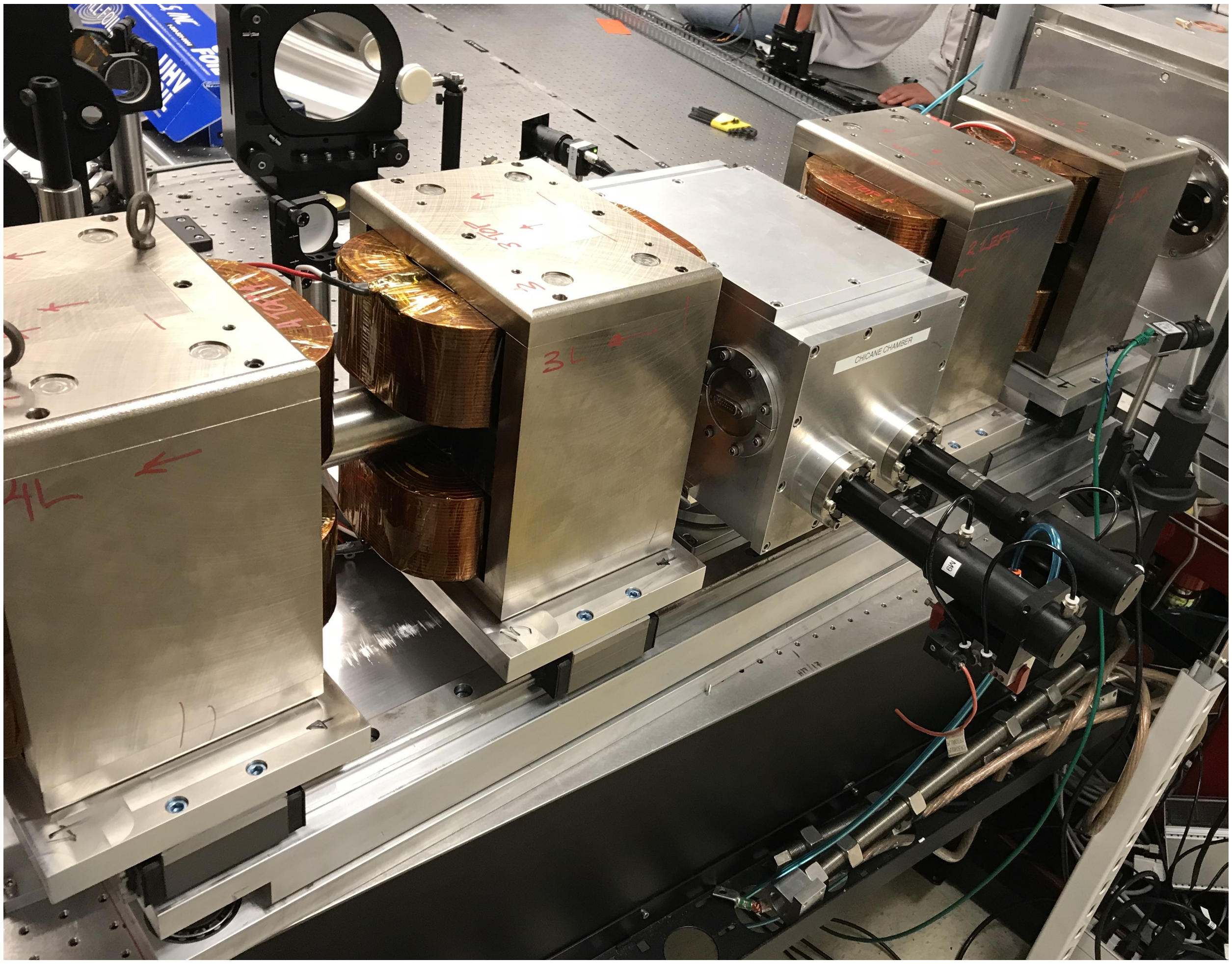

Figure 3.33: Chicane installed on LBNL beamline

CHAPTER 4

LPA driven FELs using advanced undulators

4.1 Overview

This chapter discusses the current state of LPA beams and undulators and the associated challenges with using them to build an LPA driven FEL. First, the conditions for FEL lasing as a function of beam quality and undulator specifications are established on theoretical grounds. Next, options for high gradient and short period undulators, termed “advanced undulators”, are contrasted with conventional undulators. Simulations are conducted of “direct drive” LPA driven FELs with advanced undulators for three representative cases: the BELLA FEL beamline, the current best experimentally realized LPA beams, and a high quality, simulated LPA beam. Finally, fabrication techniques and simulation studies for two advanced undulator concepts are shown.

4.2 Conditions on FEL lasing

Free electron laser physics is an immensely deep and complex subject, most of which is beyond the scope of this chapter. Luckily, there are excellent resources which offer an introduction to the fundamentals of the subject including [4, 3]. For the purposes of this chapter, the most relevant concepts will be those applied to a high gain, non-seeded, x-ray free electron laser with a focus on the FEL functionality based on beam and undulator parameters.

4.2.1 1D FEL fundamentals

In the most basic implementation of a non-seeded, high gain free electron laser, the process of lasing begins with the production of spontaneous synchrotron radiation in an undulator. To lowest order, the magnetic field of the undulator can be expressed as:

$$B_y = B_0 \sin(k_u z), \tag{4.1}$$

where B_0 is the peak magnetic field, k_u is the wavenumber of the undulator, and z is the longitudinal position. The strength of the undulator is characterized by the K_0 value, defined:

$$K_0 = \frac{eB_0}{mck_u} \approx 0.934 B_0[\text{Tesla}]\ \lambda_u[\text{cm}], \tag{4.2}$$

where λ_u is the undulator wavelength. The standard expression for the fundamental wavelength of synchrotron radiation from an undulator on axis is [89]:

$$\lambda_r = \frac{\lambda_u}{2\gamma_0^2}\left(1 + \frac{K_0^2}{2}\right). \tag{4.3}$$

The free electron laser mechanism, in the high gain regime, is the result of a resonant self-interaction between an electron bunch and an electromagnetic field that it is generating. In free space, there is no sustained interaction because the synchrotron radiation will continuously slip off the bunch. However, if the synchrotron radiation slips forward by exactly one period per undulator period, a resonant interaction becomes possible. Neglecting all effects except the subluminal speed of the electron bunch and the path length increase due to the electrons' sinusoidal motion, this resonant condition is satisfied by radiation with wavelength given in equation 4.3.

Within each of these slices separated by λ_r, electrons either gain or lose energy to the EM field, depending on their phase within the “ponderomotive bucket”. Over time, these energy differences result in ballistic bunching whereby the electrons which were near the tail of the bunch which have gained energy catch up to the electrons which were near the head that lost energy. This periodic current modulation is called “microbunching” (See Figure 4.1).

These microbunches, spaced as they are at the EM field's wavelength, are able to radiate coherently by continuing to transfer electron kinetic energy into the EM field, leading to the massive brightness gain over incoherent sources of x-rays. This process is described to first order by the *FEL pendulum equations* [4] which relate the electrons' phase relative to the EM wave, θ, to their relative energy error from the design energy $\eta = (\gamma - \gamma_0)/\gamma_0$ according to:

$$\frac{\mathrm{d}\theta}{\mathrm{d}z} = 2k_u\eta \tag{4.4}$$

$$\frac{\mathrm{d}\eta}{\mathrm{d}z} = \frac{eK_0[\mathrm{JJ}]E_0}{2\gamma_0^2 mc^2}\cos(\theta + \psi_0), \tag{4.5}$$

where [JJ] is the Bessel function factor dependent on K_0 (of order unity) and E_0 and ψ_0 are the amplitude and phase of the electric field respectively.

This gain process is characterized by the *Pierce parameter*, ρ, which was mentioned previously but reproduced here:

$$\rho = \left(\frac{I_e K_0^2[\mathrm{JJ}]^2}{16 I_A \gamma_0^3 \sigma_x^2 k_u^2}\right)^{1/3}, \tag{4.6}$$

where I_e is the beam current, I_A is the Alfvén current, and σ_x is the transverse beam size. In this idealized regime, sometimes also called the 1D regime, the gain length is given as

$$L_{G0} = \frac{\lambda_u}{4\pi\sqrt{3}\rho}, \tag{4.7}$$

where each L_{G0} of undulator the beam traverses corresponds to one e-folding in power, i.e. an increase of $\sim 2.72\times$. This exponential gain in power continues until *saturation*, which occurs when the resonant condition is no longer satisfied, typically because enough kinetic energy has been extracted from the beam to appreciably change the slippage length from λ_r. At saturation the radiation power is approximately equal to ρ times the beam power.

Real world FELs must contend with more issues than those outlined in this idealized, 1D model. These will be discussed qualitatively and also given as quantified, scaled parameters

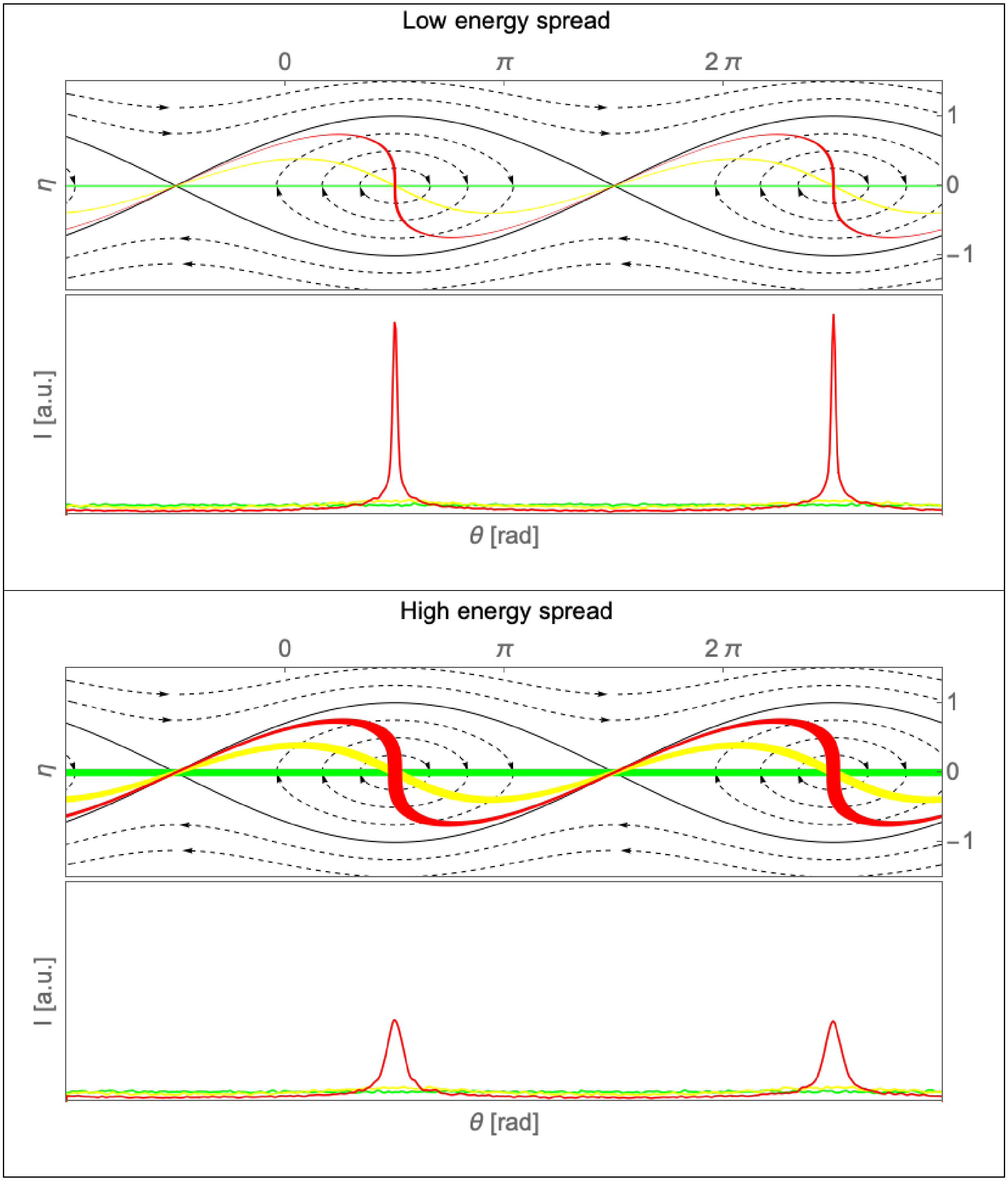

Figure 4.1: Schematic of microbunching in the ponderomotive bucket for a low energy spread (top) and high energy spread (bottom) cases. The beam's initial state is in green, fully microbunched state is in red, and an intermediate state in yellow. A plot showing the beams' current profile is also included, with the same scale for each, showing the current spike narrowing and increasing.

in the following subsections.

4.2.2 3D error - energy spread

First among these issues is that of energy spread, described by [4]: “Since the FEL interaction is a resonant energy exchange between the electron and the radiation field, the evolution of the electrons’ phase may affect the FEL performance critically. [...] an initial energy spread can cause a phase spread [...] that degrades the microbunching process.” For illustrative purposes, this can be understood by considering a rigid beam distribution in phase/energy trace space in the ponderomotive bucket described before. A beam with a small energy spread ends up covering a very thin region of phase, on the other hand, a beam with a large spread ends up spread over a larger region of phase, reducing the coherence of its contribution to the EM field. This is shown by the broader and lower current spike in Figure 4.1 for the higher energy spread beam.

The scaled parameter for this error is:

$$\eta_\gamma = \frac{4\pi L_{G0}\sigma_\eta}{\lambda_u}, \tag{4.8}$$

where σ_η is the rms value of $\eta = (\gamma - \gamma_0)/\gamma_0$.

4.2.3 3D error - emittance

The next issue encountered by real world FELs is that of finite emittance. Different particles with different amplitude trajectories due to natural undulator focusing and/or a strong focusing lattice will have slightly different path lengths than the nominal path length induced just by the undulator field. This effect is evident by examining the average longitudinal velocity of an electron as a function of its transverse actions [4]:

$$\frac{\bar{v}_z}{c} = 1 - \frac{1 + K_0^2/2}{2\gamma} - \frac{J_x + J_y}{\beta}, \tag{4.9}$$

where the transverse actions are defined:

$$J_{\{x,y\}} = \frac{\beta}{2}\left(k_\beta^2\{x,y\}^2 + p_{\{x,y\}}^2\right), \tag{4.10}$$

and where β and k_β are the focusing beta function and wave number respectively. The path length difference resulting from this reduced average longitudinal velocity means that particles with higher actions will slip further behind the EM field than design trajectory particles, also leading to dilution of the microbunching, reduced coherence, and worse gain. The ensemble mean particle actions are equal to the beam's emittance, $\langle J_{\{x,y\}}\rangle = \epsilon_{\{x,y\}}$.

The scaled parameter for this error is:

$$\eta_\epsilon = \frac{4\pi k_\beta L_{G0}\epsilon}{\lambda_r}. \tag{4.11}$$

4.2.4 3D error - diffraction

The last issue that will be considered here is that of diffraction. The radiation generated by the electron beam will naturally diverge, with a lower bound given by a *diffraction limited* beam. For a diffraction limited beam, the spot size will double over a Rayleigh length, $Z_R \equiv 4\pi\sigma_x^2/\lambda_r$. This expansion will cause there to be less power density within the transverse spot size of the electron beam, reducing coupling. This effect is mitigated if the Rayleigh length is long relative to the gain length, i.e. energy is being coupled in from the electron beam's kinetic energy faster than it is being lost to the divergence of radiation.

The scaled parameter for this error is:

$$\eta_d = \frac{L_{G0}\lambda_r}{4\pi\sigma_x^2}. \tag{4.12}$$

4.2.5 3D FEL fitting

Ming Xie developed a fitting formula [90, 91] which gives an estimate for the 3D performance of an FEL as a function of its 1D performance and the scaled parameters from above: η_γ, η_ϵ, and η_d. The *gain length degradation factor*, Δ, is approximated by the expression:

$$\begin{aligned}\Delta = a_1\eta_d^{a_2} + a_3\eta_\epsilon^{a_4} + a_5\eta_\gamma^{a_6} + a_7\eta_\epsilon^{a_8}\eta_\gamma^{a_9} + \\ a_{10}\eta_d^{a_{11}}\eta_\gamma^{a_{12}} + a_{13}\eta_d^{a_{14}}\eta_\epsilon^{a_{15}} + a_{16}\eta_d^{a_{17}}\eta_\epsilon^{a_{18}}\eta_\gamma^{a_{19}},\end{aligned} \tag{4.13}$$

with the coefficients

$$\begin{aligned}&a_1 = 0.45,\ a_2 = 0.57,\ a_3 = 0.55,\ a_4 = 1.6,\ a_5 = 3,\ a_6 = 2,\\ &a_7 = 0.35,\ a_8 = 2.9,\ a_9 = 2.4,\ a_{10} = 51,\ a_{11} = 0.95,\ a_{12} = 3,\\ &a_{13} = 5.4,\ a_{14} = 0.7,\ a_{15} = 1.9,\ a_{16} = 1140,\\ &a_{17} = 2.2,\ a_{18} = 2.9,\ a_{19} = 3.2.\end{aligned} \tag{4.14}$$

This Δ factor can be used to approximate the 3D gain length:

$$L_G \approx L_{G0}(1+\Delta), \tag{4.15}$$

the saturation power:

$$P_{\text{sat}} \approx \frac{1.6}{(1+\Delta)^2}\rho P_{\text{beam}}, \tag{4.16}$$

and the saturation length:

$$\frac{z_{\text{sat}}}{L_G} \approx \ln\left(\frac{20 I_e t_c}{e}\right), \tag{4.17}$$

where t_c is the coherence time, which depends on the FEL bandwidth σ_ω according to $t_c = \sqrt{\pi}/\sigma_\omega$. For most FELs though, this value $\frac{z_{\text{sat}}}{L_G}$, "typically varies little from 18 to 20" [4].

4.3 Current approaches to a LPA driven FEL

Since the earliest demonstration of a bubble regime LPA in 2002 with its low energy (<200 MeV peak) and large energy spread (>100%), the techniques and technologies used in LPAs have dramatically evolved. Beams in a variety of operational regimes have been produced, including energies up to 8 GeV [11], currents over 10 kA [12], normalized transverse emittances below 60 nm-rad [13], and sub-% energy spreads [13, 14]. Generally though, there is a trade-off between beam parameters. Although an individual LPA experiment might deliver high energy, high current, low emittance, or (relatively) low energy spread, no group has demonstrated an LPA which can achieve all these results simultaneously, in the manner that a modern linac can. Generally, the energy spread is the limiting factor since, at the ∼% level, they are still too large to direct drive lase with a conventional undulator. Referring back to the expression for the energy spread parameter, equation 4.18, and substituting in for L_{G0} from equation 4.7:

$$\eta_\gamma = \frac{4\pi L_{G0}\sigma_\eta}{\lambda_u} = \frac{\sigma_\eta}{\sqrt{3}\rho}. \tag{4.18}$$

Since the equation for the degradation factor Δ is comprised of terms with η_γ to powers over 1, a rule of thumb for maintaining an acceptably low degree of degradation is to hold $\eta_\gamma \ll 1$, i.e. $\sigma_\eta \ll \rho$. For typical FEL undulators, ρ ranges from 10^{-4} to 10^{-3} which corresponds to roughly requiring an energy spread of less than 0.1% to 0.01%, several orders of magnitude lower than the current ∼% values. Therefore, all current LPA driven FEL experiments employ techniques to skirt these constraints while using conventional accelerators. There are two main approaches in use.

4.3.1 Transverse gradient undulator

The transverse gradient undulator (TGU) approach [3, 15, 16, 17] employs an undulator where the field strength is scaled according with the function $1+f(x)$, i.e. varying magnitude in the transverse direction. Recalling that K_0 is proportional to B_0 and that the resonant condition from equation 4.3 depends on this, arrive at a new expression for the resonant wavelength which depends on x:

$$\lambda_r = \frac{\lambda_u}{2\gamma^2}\left(1 + \frac{((1+f(x))K_0)^2}{2}\right). \tag{4.19}$$

But if a matching correlation in γ and x is introduced, it is possible that the whole beam might satisfy the resonant condition simultaneously, with each part of the beam transversely having an acceptably small energy spread. Such a solution is far from ideal though since TGUs have worse gain than a typical undulator, larger spot sizes leading to worse coherence, and they require beam optics for injecting a dispersed beam into the TGU [3].

4.3.2 Beam decompression

The other major approach for an LPA driven FEL under investigation is to decompress the beam using a chicane before injecting it into the undulator [18, 19, 20, 21]. Although the energy spread over the whole beam remains at the few-% level, the energy spread over a coherence length, $\lambda_c = \lambda_r/4\pi\rho$, is reduced below ρ, satisfying the condition from equation 4.18 (A more complete discussion of this approach is found in Chapter 3 including an illustration in Figure 3.1, reproduced here as Figure 4.2). This comes at the cost of current though, and $\rho \propto I_e^{1/3}$ so selecting the appropriate amount of decompression is an optimization problem, balancing the lost current versus the improved local energy spread. There are additional disadvantages to the decompression approach over a direct-drive system: coherent synchrotron radiation (CSR) generated in the chicane required for decompression can degrade the beam and a longer and more complex beamline is required to facilitate the decompression. Unlike the TGU approach though, beam decompression allows for the use of a conventional undulator which is especially appealing if an undulator is already available for use, as was the case at BELLA FEL.

4.4 Advanced undulators

Broadly speaking, the term *advanced undulators*, encompasses any undulator design which is not a pure permanent magnet (PPM) or hybrid Halbach with a few-cm λ_u which forms the basis of all extant XFELs. The undulators of all operating XFELs at time of writing [92, 93], are summarized in Table 4.1. There is an enormous breadth of research into advanced undulators including designs based on: superconducting wire [94, 95, 96], bulk superconductors

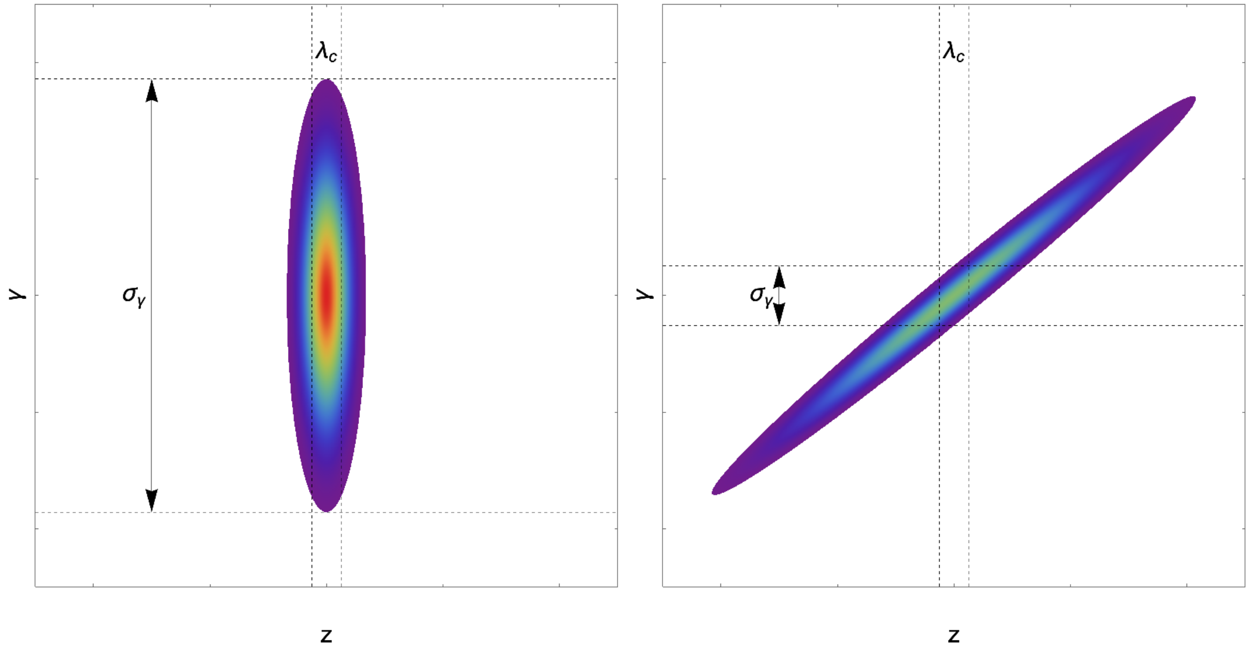

Figure 4.2: (Figure 3.1 reproduced here) The longitudinal phase space of an LPA beam before and after being chirped by a dispersing element. Observe how the energy spread, σ_γ, over a coherence length, λ_c, is reduced by chirping.

[97, 98, 99], field redistribution [100, 101], MEMS electromagnets [102], microundulators [103, 104, 105], RF [106, 107, 108], cryogenic magnets [109, 110, 111], crystals [112, 113], laser driven bifilar [114], and plasma channels [115, 116, 117]. For this chapter though, the two primary innovations considered will be the use of cryogenic magnets and techniques for microundulator fabrication, which can be used with cryogenic magnets.

Cooling praseodymium doped NdFeB magnets to cryogenic temperatures (∼30 K) dramatically enhances the magnetic performance in terms of residual magnetization B_r, coercivity H_c, and energy product (See Figure 4.3). This effect was studied in [109], wherein a short period period undulator (9 mm) was selected with a B_{peak} of 2.2 T. Such an undulator has nearly twice the field of any undulator in Table 4.1 while also having only a fraction of the period. For the following simulations, this work will serve as the reference point for undulator performance. Although they selected a particular λ_u and gap value, a smaller gap or a change in geometry would increase the field further: $B_{\text{peak}} = 3.0$ T is taken as the

Name	λ_u [mm]	Array type	B_{peak} [T]	K_0
LCLS [5]	30	Hybrid	1.3	3.7
SACLA [118]	18	Hybrid	1.3	2.2
European XFEL (SASE 1) [119]	36	Hybrid	1.0	3.3
European XFEL (SASE 2) [119]	48	Hybrid	0.6	2.8
European XFEL (SASE 3) [119]	80	Hybrid	0.4	3.3
PAL-XFEL (HXU) [120]	26	Hybrid	0.8	2.0
PAL-XFEL (SXU) [120]	35	Hybrid	1.0	3.3
Swiss XFEL [121]	15	Hybrid	0.9	1.2
FLASH [122]	27	PPM	0.5	1.2
Fermi FEL-1 [123]	65	PPM, APPLE-II	0.9	4.0
Fermi FEL-2 [123]	50	PPM, APPLE-II	0.9	2.8

Table 4.1: Undulator period, type, peak field, and K_0 value for all operational XFELs. (An APPLE-II undulator is a type of helical, variable polarization, PPM undulator)

maximum in this section.

4.5 Advanced undulator LPA-FEL simulations

Simulations using the venerable GENESIS code [124] are conducted for direct drive LPA driven FELs with advanced undulators. For these "direct drive" systems, it is assumed that the beam is matched into the FEL from the LPA using a single focusing element, e.g. a PMQ triplet or active plasma lens, with no other beam optics. Three representative cases are considered: the BELLA FEL beamline, the current best experimentally realized LPA beams, and simulated LPA beams. For the BELLA FEL case, the relaxation in the σ_γ requirement facilitated by an advanced undulator is explored. For best experimental LPA case, it is shown that pairing an advanced undulator with a demonstrated, real-world LPA beam could facilitate the demonstration of a direct drive FEL with significant power enhancement over the spontaneous synchrotron radiation. Finally, an LPA beam described

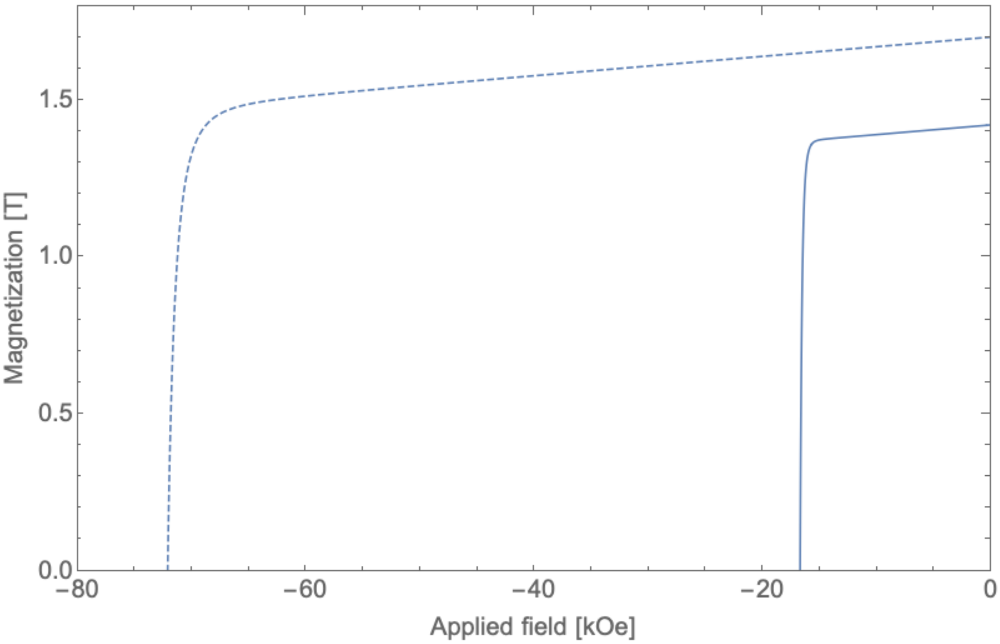

Figure 4.3: Performance of praseodymium doped neodymium magnets at 30 K (dashed) and 300 K (solid). Data from [109].

by a computational paper is paired with an advanced undulator to simulate an x-ray water window FEL with high power output.

4.5.1 BELLA FEL beamline driver

4.5.1.1 TREX beam

In the original proposal for the BELLA FEL experiment by PI Jeroen van Tilborg [21], a preliminary case was laid out for a decompression based LPA driven FEL predicated on a capillary LPA beam, previously demonstrated at BELLA TREX [12]. The beam used for their GENESIS simulation had a central energy of 250 MeV with a charge of 100 pC at a 10% rms energy spread (corresponding to a peak spectral charge density of 1.7 pC/MeV) with an rms bunch length of 1 μm corresponding to a peak current of 12.8 kA with a normalized emittance of 100 nm-rad. The beam was subsequently decompressed in a chicane by a factor of 64, reducing the peak current to 0.2 kA, the instantaneous energy spread to 0.16% and increasing the rms bunch length to 64 μm. This beam was matched (with chromatic effects accounted for but not coherent synchrotron radiation) to the VISA undulator [125] with its period of 1.8 cm and K_0 value of 1.26, corresponding to a B_{peak} of 0.75 T. They calculate that this configuration will yield approximately a peak power of 0.1 MW at $\lambda_r = 67$ nm. This is approximately two orders of magnitude of enhancement in power over the spontaneous synchrotron radiation.

This will be the first case considered for the application of a cryoundulator to a direct drive FEL; supposing all of the above beam and undulator parameters are held constant, FEL performance as a function of σ_γ and B_{peak} is explored. Recall that the Pierce parameter, ρ, scales approximately with $B_{\text{peak}}^{2/3}$, and that the scaled energy spread parameter η_γ scales with the inverse of ρ. Therefore, the deterioration in FEL performance due to energy spread can be mitigated by employing higher magnetic field strengths.

In Figure 4.4 over 1,800 time dependent simulations were conducted in GENESIS. The plot shows the coherent power enhancement, i.e. $P(z = L_u)/P_{\text{spontaneous}}$. In this case, the length of the undulator, L_u, is selected based on the slippage of the radiation off the beam; for these extremely short, 1 μm long, beams it is not feasible to demonstrate high gain FEL operation at optical or longer wavelengths since the beam will demonstrate superradiant lasing spontaneously. With this in mind, L_u is set based on a slippage of 8 σ_z, i.e. $L_u = \frac{8\sigma_z\lambda_u}{\lambda_r}$. L_u and λ_r calculated using equation 4.3 are shown in Figure 4.5. This result shows that an equal enhancement in power over spontaneous power can be achieved with a cryoundulator with a beam that has twice the energy spread as compared to the VISA undulator. However, due to the short beams, there is an upper bound on increasing K_0 at around $B_{\text{peak}} = 2.0$ T; beyond this point, the reduced interaction length from the shorter undulator begins to overwhelm the improved performance due to reduced η_γ. Therefore, based on the TREX beams, moving to a cryoundulator is not a compelling option since the maximal allowed energy spread for $> 100\times$ coherent enhancement is around 2%, five times higher than the actual observed values near 10%.

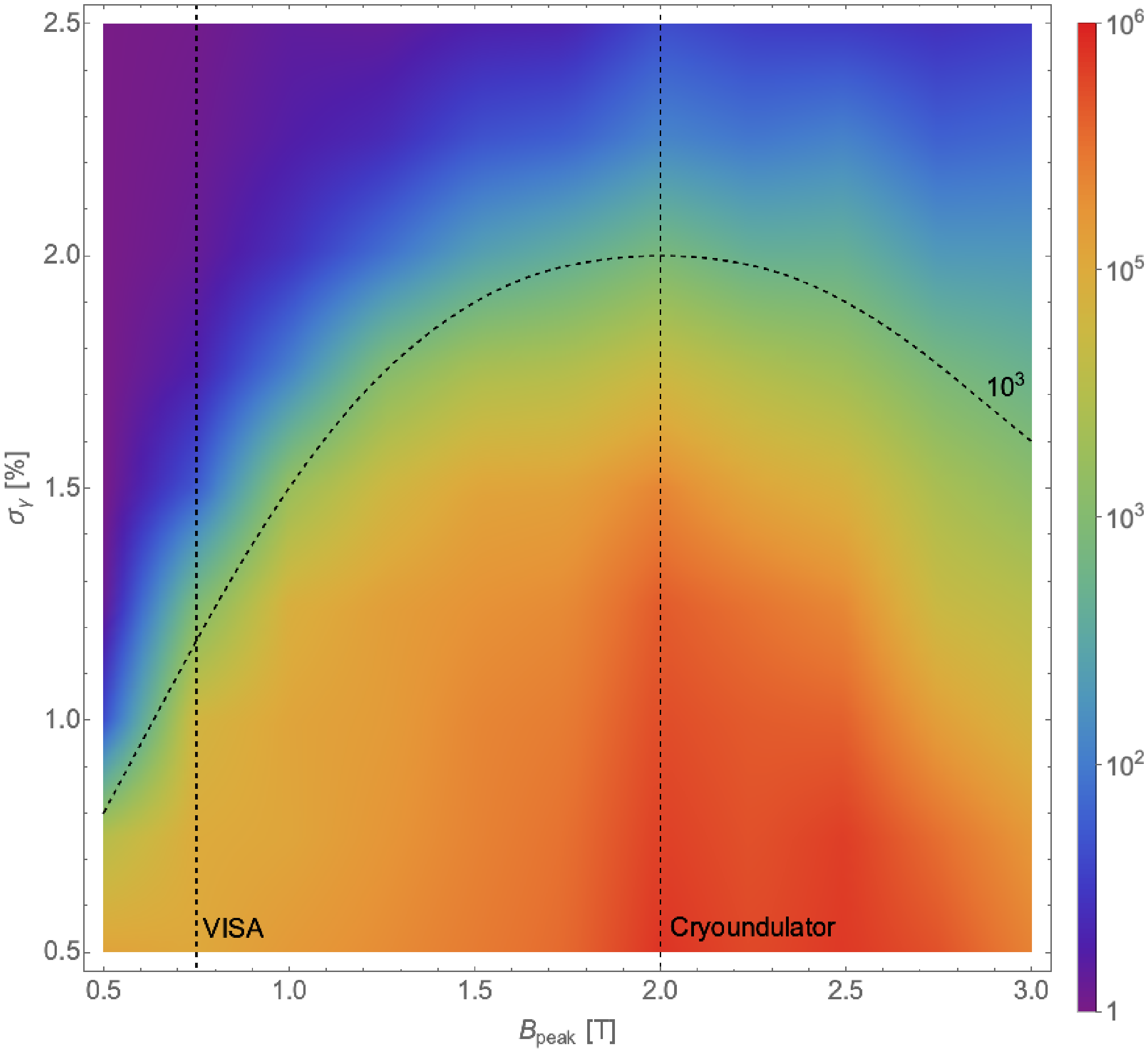

Figure 4.4: The power enhancement over the spontaneous synchrotron radiation ($P(z = L_u)/P_{\text{spontaneous}}$) is shown as a function of B_{peak} and σ_γ while otherwise assuming BELLA beam parameters and VISA undulator λ_u. The 10^3 enhancement isocontour is highlighted, and the B_{peak} values corresponding to VISA and an optimized cryoundulator are shown.

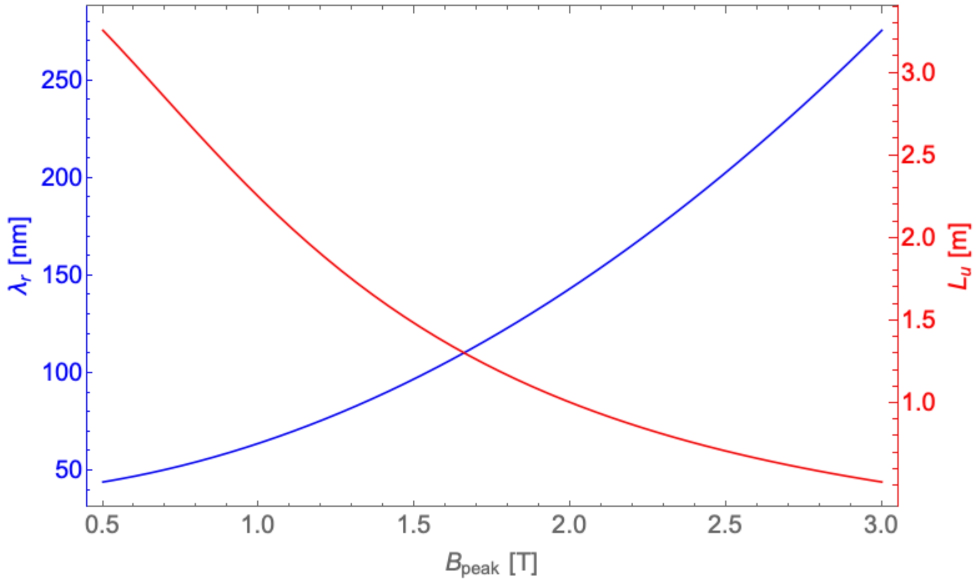

Figure 4.5: The undulator length, L_u, and fundamental radiation wavelength, λ_r, as a function of the peak undulator magnetic field, B_{peak}, for the TREX-style LPA driven FELs simulated in Figure 4.4.

4.5.1.2 Optimized BELLA beams

The beams described above are the most conservative estimate (having been previously demonstrated) and served in the proposal [21] to illustrate the flexibility of the decompression scheme, even to significantly suboptimal beams. A later paper by van Tilborg, *et al.* [126], conducts GENESIS simulations predicated on a capillary LPA beam optimized for FEL operation. This beam has a lower charge, 25 pC, lower energy, 220 MeV, and worse normalized emittance, 300 nm-rad, but crucially has an improved energy spread of 1%. This 1 μm, 3.2 kA beam is decompressed by only 4.5× to 4.5 μm and 0.7 kA. After passing through the 4 meters of VISA undulator, they simulate an output of 100 MW at $\lambda_r = 87$ nm, approximately three orders of magnitude over the spontaneous synchrotron radiation. For this case, the application of a cryoundulator is extremely compelling.

In Figure 4.6 8,800 time dependent simulations were conducted in GENESIS. The beam described in [126] was used directly to drive a cryoundulator with variable λ_u and B_{peak}. These results show that in only 0.5 m of cryoundulator, a peak power output of nearly a gigawatt is possible, corresponding to an enhancement of four orders of magnitude over the spontaneous synchrotron radiation. With 1.0 m of cryoundulator, a peak power of nearly five gigawatts is possible. Contrast these results with the proposed decompression experiment using the same beam: even though the beamline is more complex and the undulator is 4 meters long, the simulated peak power is only 100 MW. Further, since the power outputs described can be achieved at a range of radiation wavelengths depending on the undulator parameters, over a gigawatt can be produced with a meter of undulator for wavelengths from 45 nm and up. Note that simulations where the situation is superradiant, rather than high gain, i.e. the assumption that $\lambda_r \ll \sigma_z$ is violated, are omitted since GENESIS is not capable of handling such cases. Although these cases will output high power, they are outside the scope of this discussion since the spontaneous radiation is functionally the same.

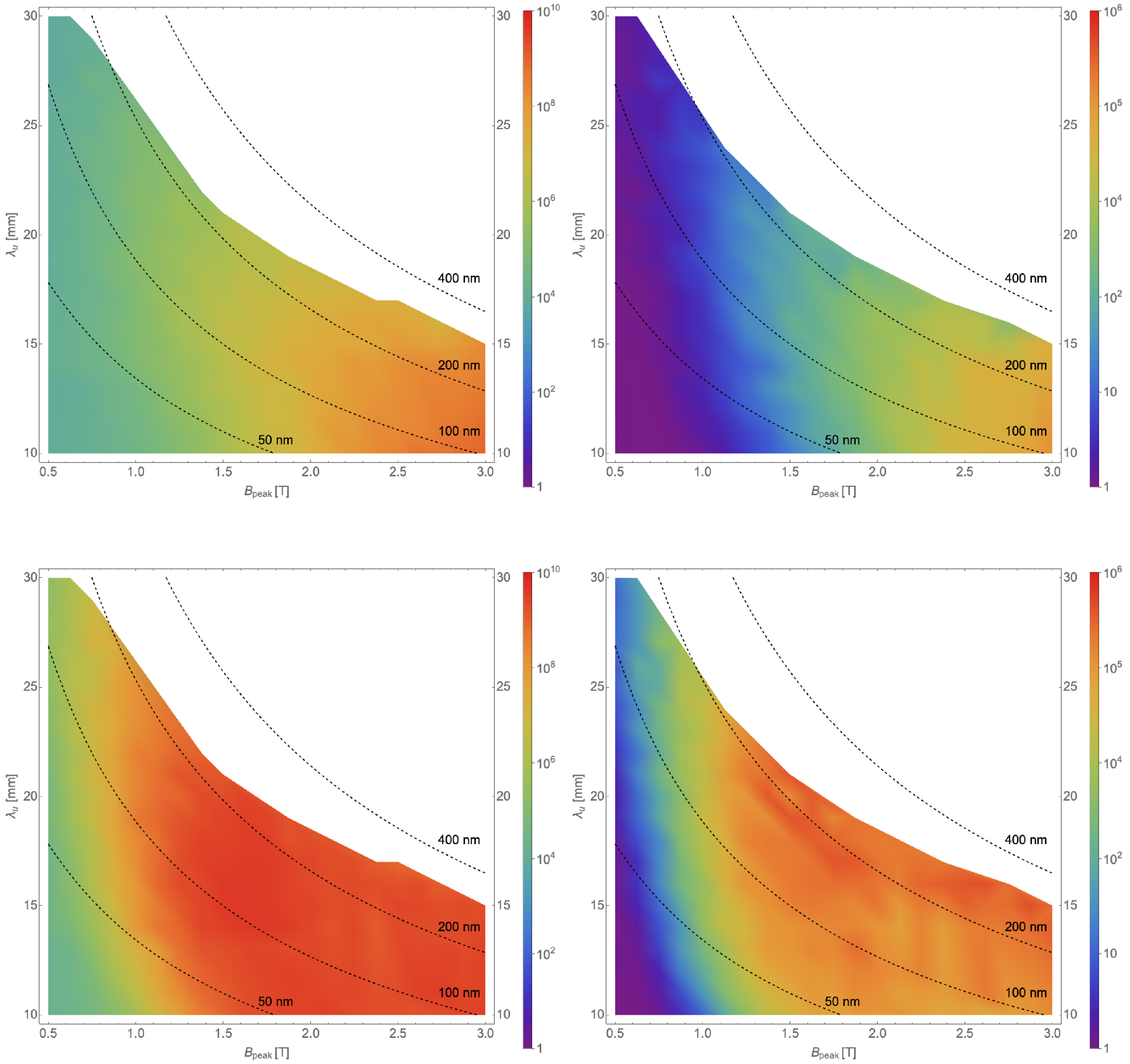

Figure 4.6: Plots of the absolute (left) and relative power, $P(z = L_u)/P_{\text{spontaneous}}$, (right) as a function of B_{peak} and λ_u for the optimized BELLA LPA beams described in [126] based on SASE averaged GENESIS simulations. Undulator lengths, L_u, of 0.5 m (top) and 1.0 m (bottom) are considered. The isocontours for different λ_r values are included. Superradiant cases, i.e. when the assumption that $\lambda_r \ll \sigma_z$ is violated, are omitted

4.5.2 Best experimentally demonstrated LPA driver

This section considers an advanced undulator based LPA-FEL using an experimentally demonstrated driver beam, the goal being to show that, by employing an advanced undulator, an LPA driven high gain FEL could be demonstrated using LPA beams available today. Table 4.2 includes a summary of the parameters relevant for FEL operation for a variety of demonstrated and simulated LPA beams including charge, energy, length (as a proxy for current), energy spread, and emittance. Also shown are a few other examples of non-LPA drivers such as the LCLS photoinjector and linac and a plasma wakefield accelerated plasma photocathode beam, termed "trojan horse". From these, the beam from [14] has been selected as a driver for GENESIS simulations with parameters: 80 pC, 600 MeV, 3 μm, 0.4% spread, and 1400 nm-rad emittance.

In the previous section, the issue of external focusing was ignorable due to the very low emittances and short undulator lengths; relying solely on the natural focusing of the undulator was sufficient [3]. For this scenario however, applying a focusing lattice can marginally improve FEL performance. It will be assumed that there is an integral FODO focusing lattice in the undulator, rather than having quads between undulator sections. A discussion of the implementation of such focusing is beyond the scope of this document but might include a basic bar magnet approach like the VISA undulator [125] or a novel implementation of Panofsky quadrupoles [82]. Quadrupole gradient values of 33 T/m have been demonstrated in the VISA undulator and simple scaling laws readily extend this to ~100 T/m. Figure 4.7 shows the effect of quadrupole focusing fields up to 200 T/m to illustrate the diminishing return from going to greater gradients. This case uses an undulator with $\lambda_u = 20$ mm, $B_{\text{peak}} = 2.2$ T, quadrupole lengths of 8 periods (8×20 mm $= 160$ mm), and zero length intra-quad drifts. For this case, some marginal enhancement occurs by focusing using an external lattice; focusing down from a natural spot size around 20 μm to 18.2 μm using 70 T/m gradients enhances the average, saturation peak power by about 50% (This is $\ll$ the shot to shot variation due to SASE startup though) beyond 130 T/m or so though, the focusing is excessive and the power begins to drop again. This is not in clear agreement with

Reference	Type	Charge [pC]	Energy [MeV]	Length [μm]	Spread [%]	Normalized emittance [nm-rad]
[12]	LPA - demonstrated	100	250	1	10	100
[14]	LPA - demonstrated	80	600	3	0.4	1400
[127]	LPA - demonstrated	0.4	460	0.3	2.8	100
[128]	LPA - demonstrated	15	300	1.4	6	70
[129]	LPA - demonstrated	45	450		4.5	
[130]	LPA - simulated and demonstrated	20	90	0.27	5	2000
[13]	LPA - simulated and demonstrated	15	360		0.4	56
[131]	LPA - simulated	4.5	784	0.18	0.2	80
[132]	LPA - simulated	30	150	1	0.5	30
[126]	LPA - proposed	25	220	1	1	300
[133]	Plasma photocathode	2	300	2	3	30
[5]	Conventional RF	1000	14350	23	0.06	1200

Table 4.2: Overview of demonstrated and simulated LPA beams. The most critical parameters for FEL performance: charge, energy, length (as a proxy for current), energy spread, and emittance are included where possible. If a reference included a range of values, the best one is shown. Rows for other acceleration techniques proposed or used as FEL drivers are also included: a conventional photoinjector and linac and a plasma wakefield accelerated plasma photocathode beam.

the expected optimal spot size [3]:

$$\sigma_x = \sqrt{\frac{L_G}{\lambda_r/4\pi}\frac{\epsilon_n}{\gamma_0}}, \tag{4.20}$$

which gives the optimum spot size as 7 μm. This disagreement is due to the relatively high beam emittance compared to the radiation emittance, $\epsilon_r \equiv \lambda_r/4\pi$.

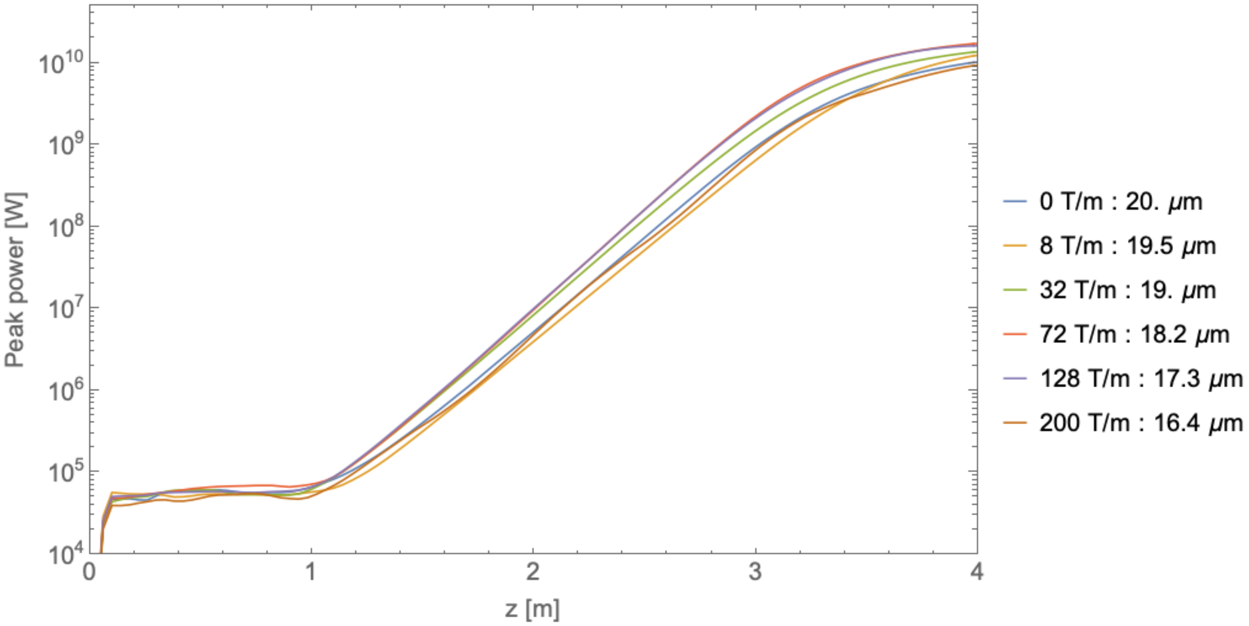

Figure 4.7: Peak power vs location along undulator for [14] beams paired with $\lambda_u = 20$ mm, $B_{\text{peak}} = 2.2$ T undulator with integral focusing with quads length 160 mm. Cases broken out by quadrupole gradient and mean spot size with 10 SASE averaged runs per case.

With a moderate focusing lattice applied, 75 T/m, corresponding to a matched, average spot size of 18.2 μm, the FEL performance as a function of λ_u with constant $B_{\text{peak}} = 2.2$ T will be considered. A summary of the results are shown in Figure 4.8 (10 SASE averaged runs per case) where λ_u is swept from 10 to 30 mm. The 10 mm case is very similar to the undulator demonstrated in [109] with its 9 mm period at $B_{\text{peak}} = 2.2$ T. This case operates right at the edge of soft x-ray and EUV with $\lambda_r = 11$ nm. At this wavelength, the beam barely demonstrates high gain, but gives a peak power output of 100 MW after 4 meters, corresponding to approximately two orders of magnitude in enhancement over the spontaneous radiation. For cases with λ_u between 15 and 30 mm the enhancement is more significant with a peak power output over 10 GW.

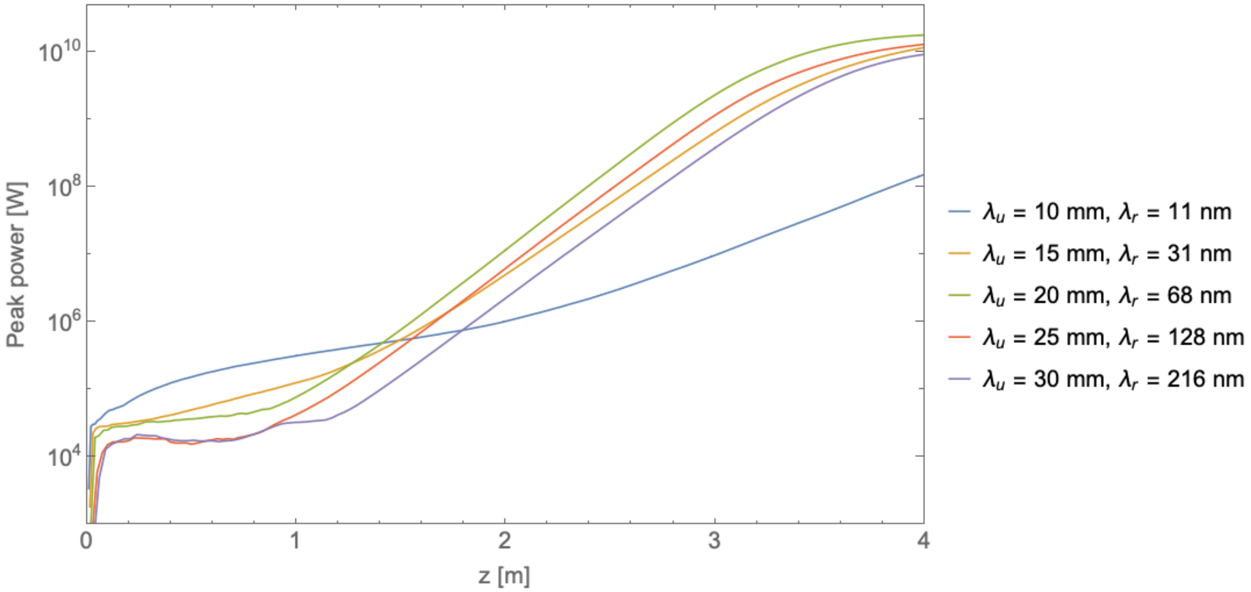

Figure 4.8: Peak power vs location along undulator for [14] beams with matched, average spot size of 18.2 μm, in undulators with $B_{\text{peak}} = 2.2$ T. Cases are broken out for different λ_u values with 10 SASE averaged runs per case.

4.5.3 PIC simulated LPA driver

For this final scenario, an LPA driver generated by a particle-in-cell (PIC) simulation is used. Referring back to Table 4.2, the entry for [131] will be used: 4.5 pC, 784 MeV, σ_z = 180 nm, 0.2% energy spread, and a normalized emittance of 80 nm-rad. This extremely bright beam can drive an FEL deep into the x-ray spectrum when paired with an advanced undulator, capable of demonstrating high gain at the x-ray water window and even higher photon energies of 1 keV.

As in Section 4.5.1, this beam is of such low emittance that the effect of focusing on FEL performance is negligible; relying on natural focusing alone gives a mean spot size of $\sim$4 μm. As in the previous section, assuming a fixed B_{peak} of 2.2 T, selecting a λ_u of 8 mm (very similar to the [109] undulator) gives $\lambda_r = 4.0$ nm. This wavelength is in the “x-ray water window", a region of spectrum between the K-edge of oxygen (2.3 nm) and the K-edge of carbon (4.4 nm) with relatively high transmission of x-rays, making it useful for the study of biological materials. Selecting a λ_u of 4 mm gives $\lambda_r = 1.1$ nm, giving a photon energy of > 1 keV.

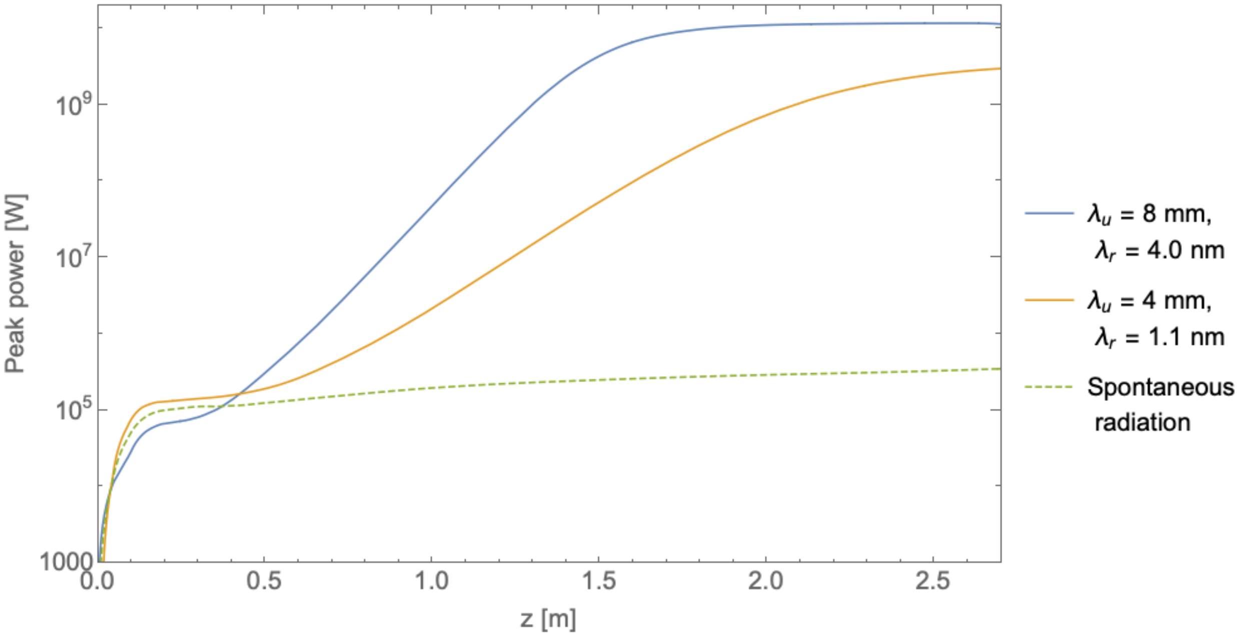

Figure 4.9: Peak power vs location along undulator for [131] beams with matched, average spot size of 4 μm, in undulators with $B_{\text{peak}} = 2.2$ T. Two cases are shown: one with a $\lambda_u =$ 8 mm undulator lasing in the x-ray water window and another with $\lambda_u = 4$ mm, lasing with a photon energy > 1 keV.

The results of 20 SASE averaged runs for each undulator configuration, 8 mm and 4 mm, are shown in Figure 4.9. Each case is capable of producing over a gigawatt of x-ray power in less than 3 meters of undulator, corresponding to 4 or 5 orders of magnitude of enhancement over the spontaneous radiation power. This scenario is illustrative of what a next generation LPA driven x-ray free electron laser might be capable as LPA beam quality continues to improve.

4.6 Design of Comb Fabricated Halbach Undulators

This section is adapted from [104] in accordance with the UCLA's dissertation guidelines, section "Alternate versions of published articles". It discusses a fabrication technique for short period "milliundulators" for both PPM and hybrid Halbach arrays. This is one potential way of realizing the undulators employed in the GENESIS simulations.

4.6.1 Introduction

An idealized Halbach array of permanent magnets, originally described by Klaus Halbach in 1980 [134, 135] for use in multipole magnets and undulators, consists of regions of permanent magnet with smoothly rotating residual fields. The benefit of this configuration is the establishment of a "strong" and "weak" side to the array, enhancing the magnetic field on the strong side and attenuating it on the weak side. This leads to more efficient use of the available magnetic flux, giving stronger fields than other magnetization configurations. Practical realizations of Halbach arrays consist of discrete magnets, each with a unique, constant magnetization vector, arranged to approximate the idealized case. Halbach arrays have been used extensively in beamline magnets including the construction of permanent magnet wigglers and undulators [136, 137, 125, 138] and multipole magnets including dipoles [139] and quadrupoles [140]. In addition to the pure permanent magnet (PPM) arrays, hybrid arrays consisting of both hard and soft ferromagnetic materials are also used [109, 141, 142]. The most common practical implementation of these hybrid arrays to realization of undulators involves magnets with alternating polarities with their magnetization vectors oriented in the longitudinal direction, interspersed with high-saturation soft ferromagnets. Such undulators are capable of achieving gap fields significantly higher than PPM undulators, for reasons that will be discussed below.

There is growing interest in the development and use of short period undulators (or *micro-undulators*) [143, 142, 144, 103, 145, 146], facilitated by MEMS (microelectromechanical systems) and other modern, non-conventional machining techniques. Decreasing the undulator period length decreases free-electron laser (FEL) or light source length while also producing harder radiation from lower energy electrons which may be produced by a shorter accelerator. Comb fabrication is one approach for facilitating fabrication of micro-undulators which has been demonstrated before for simple up-down ($M' = 2$ in the terminology of [134]) style undulators [103]. However, here we are interested in higher order, M', Halbach arrays, as they offer superior magnetic field performance. If the minimum feature size of the manufacturing process is at least 4 times smaller than the required period, either $M' = 4$ or hybrid arrays can be used. Otherwise, isosceles triangle based arrays can provide the same period length as an $M' = 2$ for a given feature size but with improved field strength [105].

4.6.2 Methods

Comb fabrication relies on the cutting of multiple "teeth" out of a single piece of material, all of which will have the same magnetization vector. Thus this approach gives a straightforward path in both mechanical fabrication and magnetization of the machined combs. These combs are designed in such a way that they may be slotted together to form the complete Halbach array of a single undulator jaw. One additional constraint to the design of these combs is that they must be manufacturable using only through-bulk cutting, as opposed to a depth controllable process such as milling. This is due to the limited selection of machining processes conducive both to machining rare earth magnets, which are brittle and hard, and capable of operating at such small length scales. Two non-conventional machining processes in particular are well suited to this task, laser machining and wire electrical discharge machining (EDM), and both are through-bulk processes. A total of four geometry types will be considered: up-down ($M' = 2$), isosceles triangle, $M' = 4$, and hybrid arrays. The idealized cross sections of each of these geometries in the two-dimensional limit, as well as example combs for each, are shown in Figure 4.13.

The $M' = 2$ array is the simplest case and comb fabrication has been previously demonstrated [103]. An array based on isosceles triangles, with the same volume of magnetic material per period and same minimum feature size, produces integrated fields approximately 20% higher than the $M' = 2$ case [105]. The $M' = 4$ case offers a higher field than either of these but requires four feature lengths per period, making it unsuitable for undulators with especially short periods. An expression from [136] gives the peak field strength for PPM, rectangle magnet Halbach arrays:

$$B_{\text{peak}} = 2B_r \frac{\sin(\pi/M')}{\pi/M'} \left(1 - e^{-2\pi h/\lambda_u}\right) e^{-\pi g/\lambda_u}, \tag{4.21}$$

where B_{peak} is the maximum magnetic field in the gap, B_r is the residual magnetization of the permanent magnets, M' is the number of magnets per period, h is the height of the magnets, g is the gap size, and λ_u is the undulator period. This suggests that, all else held equal, an $M' = 4$ array will have 0.90 times the peak field of an idealized ($M' \to \infty$) Halbach array while an $M' = 2$ array will have 0.64 times the ideal case. This result, combined with the findings of [105] indicates that the isosceles case will have 0.76 times the field of the ideal case. The performance of the hybrid case depends on additional factors, outlined below.

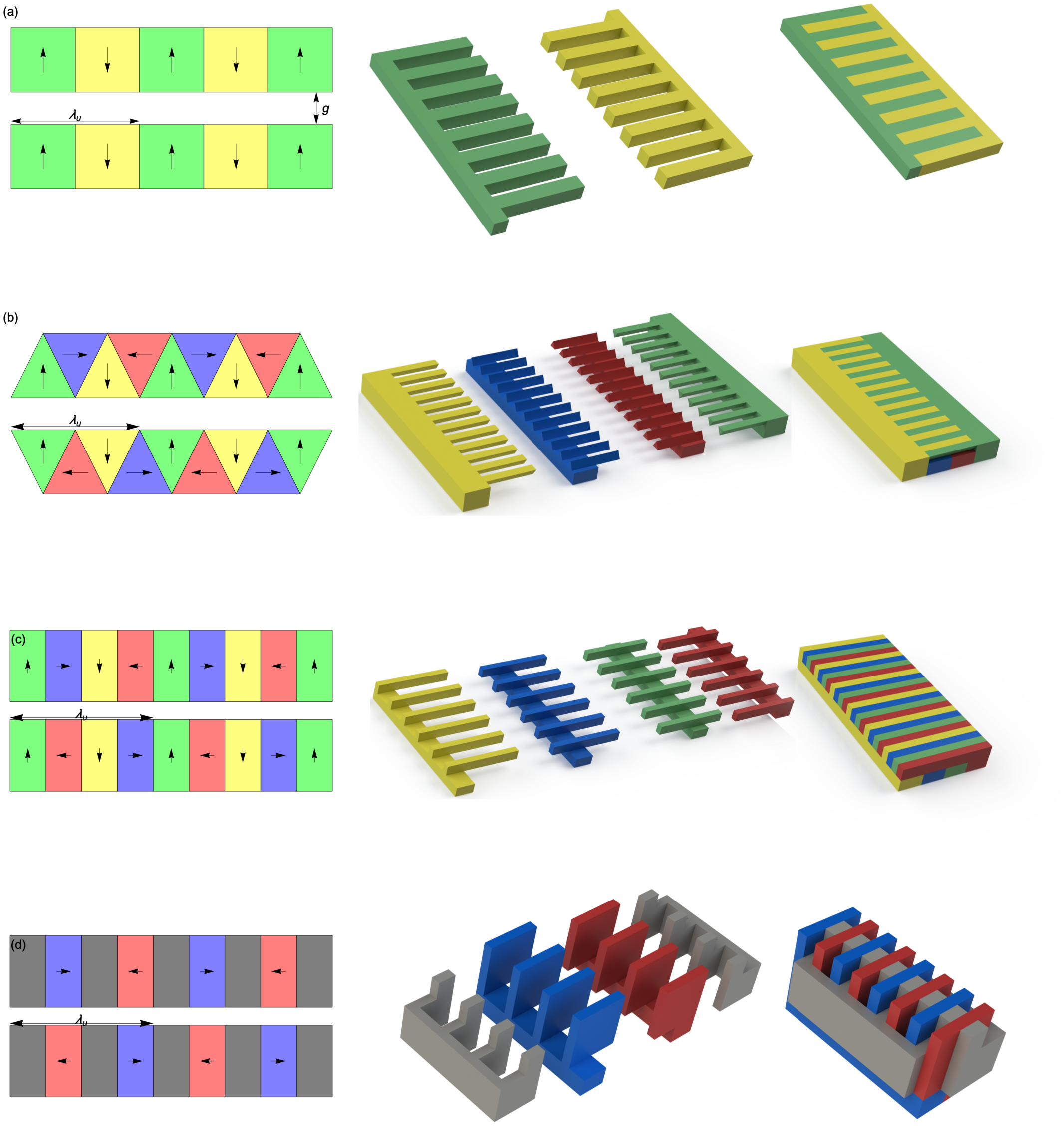

Figure 4.10: Examples of the simulated undulator configurations. The left column shows an idealized, 2D cross section omitting connecting parts. The center column shows the constituent parts of the lower jaw in a pre-assembly state. The right column shows the assembled state of the lower jaw array. By row: (a) $M' = 2$ array, (b) isosceles triangle array, (c) $M' = 4$ array, and (d) hybrid array. Green and yellow correspond to vertical magnetization vectors, blue and red correspond to longitudinal magnetization vectors, and grey corresponds to a high-saturation, soft ferromagnetic material.

Consider a magnetic circuit that is simply a “loop” of constant cross sectional area permanent magnet with an air gap. Further assume that the B-H curve can be approximated as linear with intercepts at B_r, the residual magnetization, and H_c, the coercivity:

$$B = B_r(1 + H/H_c). \tag{4.22}$$

Typical values for B_r and H_c for high quality neodymium magnets are 1.2 T and 10^6 amp/meter respectively [88]. Assuming negligible fringing fields, there is constant magnetic flux, Φ, in both the magnet and gap:

$$\Phi = A_m B_m = A_g B_g, \tag{4.23}$$

where A is the cross sectional area (normal to the flux), B is the magnitude of the magnetic flux density, and the subscripts m and g refer to the magnet and gap, respectively. Since there is no exciting current the net magnetomotive force, $\mathcal{F}$, is zero:

$$\mathcal{F} = 0 = H_g g + H_m l_m, \tag{4.24}$$

where H is the magnitude of the magnetic field $\mathbf{H}$ and g and l_m are the lengths of the flux path in the gap and magnet respectively. Using equations 4.22, 4.23, and 4.24 along with $B_g = \mu_0 H_g$, find the field in the gap to be:

$$B_g = \frac{A_m B_r H_c l_m \mu_0}{A_m B_r g + A_g H_c l_m \mu_0}. \tag{4.25}$$

Since it was assumed that the PM loop was of constant area, $A_g = A_m$, so B_g is maximized as $g \rightarrow 0$ and $B_g \rightarrow B_r$. This result is a reasonably good approximation for the PPM undulator cases as confirmed by simulation.

Now consider a magnet that is coupled to a gap by an infinite permeability yoke; the yoke will perfectly confine the flux allowing $A_g \neq A_m$. This approximates the case of the hybrid undulator where l_m is the thickness of the longitudinally magnetized PMs and A_m is their area normal to this. A_m can become large without affecting the period of the undulator so consider equation 4.25 in the limit $A_m \to \infty$:

$$B_g = \frac{H_c l_m \mu_0}{g}. \tag{4.26}$$

This result suggests that the field can become arbitrarily large as $l_m/g \to \infty$. However, this approximation is only reasonable until the yoke material saturates, violating the "infinite permeability" assertion. Since high saturation materials like vanadium permendur [88] offer saturation fields over 2.3 T, compared to the B_r of the best available permanent magnets of around 1.2 T, hybrid Halbach undulators can provide peak fields about twice as high as a PPM array.

An important caveat for these hybrid comb designs is that, to prevent leakage between the two soft ferromagnetic yoke pieces, the sections interspersed with the magnets do not cover the whole area of the magnet, A_m. In the particular case simulated, the yoke piece is only exposed to an effective area $A_{\mathrm{m,eff}} \approx A_m/2$ (See Figure 4.13(d)). This suggests magnets of approximately twice the area are required to get the same performance as would be possible if $A_m = A_{\mathrm{m,eff}}$; if non-magnetic side connecting pieces were brazed to the yoke material before machining, this might be achievable.

4.6.3 Results

The performance of Halbach comb arrays are simulated in Radia [88] over a range of gap sizes, g, and with several cases of the hybrid geometry shown with varying magnet areas (in terms of λ_u^2). The magnets are taken to be a neodymium (NdFeB alloy) with $B_r = 1.2$ T. The soft ferromagnetic yoke material is simulated as a vanadium permendur alloy with a saturation of 2.3 T and peak relative permeability of 7,000. In all the cases shown, the magnet height, h, is held constant relative to λ_u for all PPM cases; this means that $M' = 2$ has square magnets while $M' = 4$ magnets are rectangular. This keeps the volume of magnetic material per period constant as M' is varied for the most meaningful comparison. Additionally, the transverse dimension of the magnet is taken to be large relative to λ_u.

To compare between the strengths of the different configurations, it is typical to characterize undulators and wigglers in terms of a unitless parameter termed the K-value, sometimes also termed the *strength parameter*. K is defined [89]:

$$\left.\frac{\mathrm{d}x}{\mathrm{d}s}\right|_{\mathrm{max}} = \frac{1}{2}\int_0^{\lambda_u/2} \frac{e}{\gamma m_e c} B_y(s)\,\mathrm{d}s \equiv \frac{K}{\gamma}. \tag{4.27}$$

where $(\mathrm{d}x/\mathrm{d}s)_{\mathrm{max}}$ is the maximum deflection angle of the electron beam in the undulator, e is the electron charge, m_e is the electron mass, c is the speed of light, and $B_y(s)$ is the vertical field along the undulator. To compare the strengths of undulators independent of λ_u the mean absolute field, $\langle|B_y|\rangle$, can be used instead:

$$\begin{aligned} \langle|B_y|\rangle &\equiv \frac{1}{\lambda_u}\int_0^{\lambda_u} |B_y(s)|\,\mathrm{d}s \\ K &= \frac{e\lambda_u}{4m_e c}\langle|B_y|\rangle. \end{aligned} \tag{4.28}$$

$\langle|B_y|\rangle$ will be derived from the simulated fields.

Referring to Figure 4.11, the $M' = 2$ case, although the simplest to fabricate, also gives the worst performance. For typical gap sizes on the order of $\lambda_u/4$, $M' = 2$ arrays offer a $\langle|B_y|\rangle$ value of only 0.42 T while the isosceles case, despite having the same minimum feature size, has $\langle|B_y|\rangle = 0.52$ T (24% enhancement) and the $M' = 4$ array has $\langle|B_y|\rangle = 0.58$ T (38% enhancement). The hybrid cases, on the other hand, shine at particularly low g values where they can offer $\langle|B_y|\rangle$ values over 80% higher than $M' = 2$ cases.

Both the isosceles and $M' = 4$ cases appear to be converging to the residual magnet field, $\langle|B_y|\rangle \to B_r = 1.2$ T in the $g \to 0$ limit as predicted by equation 4.25, suggesting that with four magnets per period, the flux in a loop is reasonably well approximated as normal to the loop cross section. The $M' = 2$ case however is not converging to B_r, since with only two magnets per period, this approximation is significantly worse. Finally, looking at the hybrid cases, it appears that the approximation from equation 4.26 that $A_m \to \infty$ is reasonably well satisfied at values of $A_m \geq (4\lambda_u)^2$ and that there are negligible returns to increasing the cross sectional area of the magnet any further. Despite being in the large A_m limit, $\langle|B_y|\rangle$ in the $g \to 0$ limit does not appear to be the saturation field of the yoke material. This

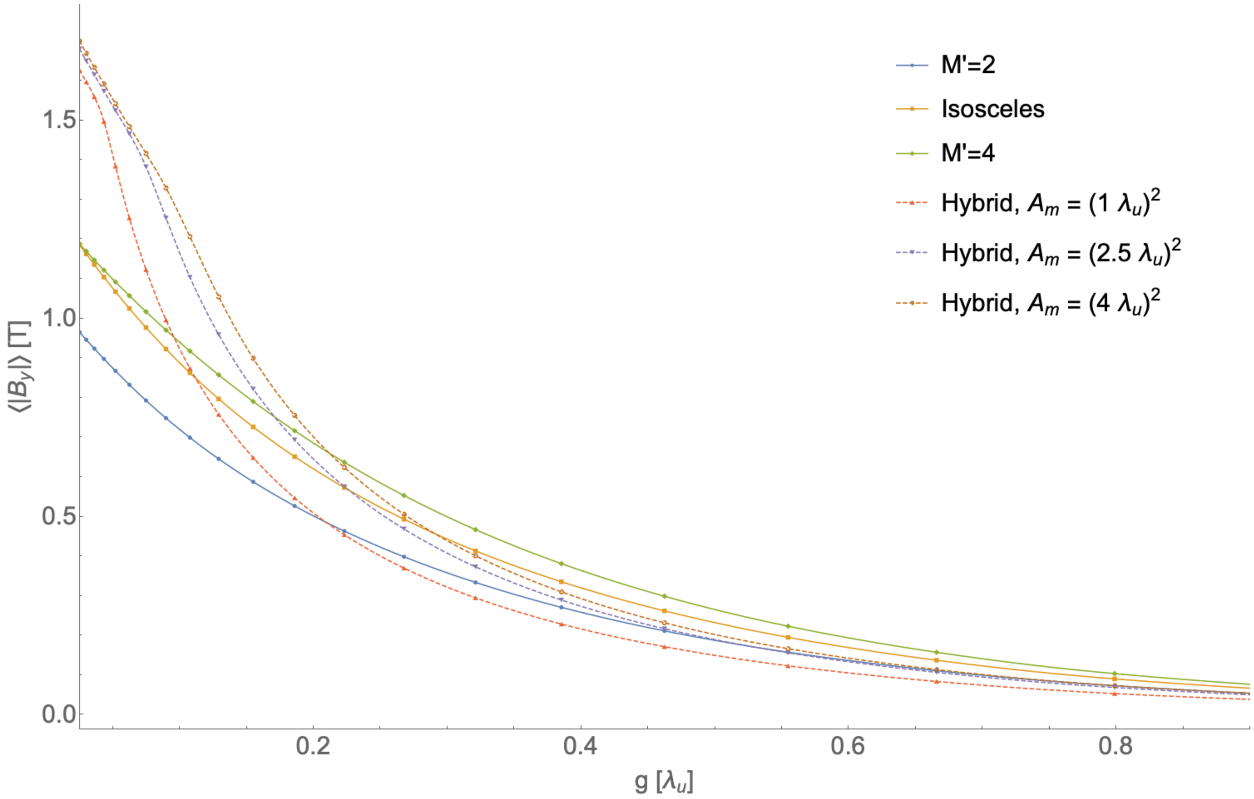

Figure 4.11: Mean, absolute fields, $\langle|B_y|\rangle$, for different Halbach geometries as a function of gap size, normalized to λ_u, based on Radia simulations.

is due to significant flux leakage between the yokes and fringing fields. Further geometry optimization may reduce this effect.

In addition to considering the field strength, the deviation of the field compared to non-comb (no non-tooth connecting pieces) Halbach arrays should be examined. For the PPM geometries, determining this effect is especially straightforward since simply taking a linear superposition of all the magnet fields is a reasonably good approximation: it is stated in Ref. [147] that "[rare earth magnets behave] magnetically very nearly like a vacuum with an impressed current. This makes it straightforward to predict analytically the field that will result from almost any configuration of blocks" . Since adjacent connecting pieces can be selected to have opposing polarization, far field errors are reduced. Further, any application particularly sensitive to such error fields can employ thicker teeth to increase the separation between the connecting magnets and the beam axis. Consider a concrete example of a $M' = 4$

undulator with $g = \lambda_u/4$ and $h = \lambda_u/2$, giving a peak field, B_{peak}, of 0.78 T. Within a square region on axis, with side length equal to $\lambda_u/8$, averaged over a period, the field from an array with connecting pieces has a mean absolute error (MAE) of 0.0029 T (0.37% of B_{peak}) when compared to the same configuration without connecting pieces. Any integrated effects can be mitigated by alternating the polarities of the connecting pieces between adjacent combs.

As mentioned before, the connecting pieces are especially impactful for the hybrid case, reducing the effective magnet area by approximately half compared to the actual magnet area and also limiting the maximum achievable gap field due to flux leakage and fringing. Despite these challenges, the hybrid arrays can offer higher $\langle |B_y| \rangle$ values than any PPM array.

4.6.4 Conclusions and future work

A technique for fabricating Halbach arrays for micro-undulators using comb elements has been discussed. This approach obviates the need for magnet-by-magnet fabrication and improves the accuracy achievable by relying on the intrinsic indexing of the comb teeth relative to each other. Example combs for a variety of Halbach configurations including $M' = 2$, $M' = 4$, isosceles triangle, and hybrid are illustrated, all of which rely only on through-bulk, non-conventional machining processes. These combs are simulated and compared over a wide range of gap sizes using the magnetostatics code Radia. Finally, the impact of the connecting pieces on the field quality has been discussed. Further work will include determining optimal wire EDM parameters for samarium cobalt machining (previous studies for neodymium magnets have been conducted [148, 149]), fabrication of proof-of-principle comb Halbach arrays, and field characterization. This work may prove to be a key component of the current UCLA effort to realize an ultra-compact X-ray free-electron laser [150].

4.7 Halbach undulators using right triangular magnets

This section is adapted from [105] in accordance with the UCLA's dissertation guidelines, section "Alternate versions of published articles". It discusses a fabrication technique for *short period "milliundulators" for both PPM Halbach arrays. This is another potential way of realizing the undulators employed in the GENESIS simulations.*

4.7.1 Introduction

The Halbach array of magnets, described in [134, 135] by the eponymous Klaus Halbach, consist of arrays of magnets with smoothly rotating residual field orientations for the construction of multipole magnets and undulators. In the intervening decades, Halbach arrays have been used extensively in the construction of permanent magnet (PM) wigglers and undulators [125, 138, 136, 137], enhanced multipole magnets including dipoles [139] and quadrupoles [140], in addition to use in motor design [151, 152] and other engineering applications [153]. The benefit of this configuration is the establishment of a "strong" and "weak" side to the array, whereby the field is enhanced on the strong side and attenuated on the weak side. This leads to more efficient use of the available magnetic flux, giving stronger fields than other configurations. Many variations exist, most notably the hybrid-Halbach which includes both hard and soft ferromagnetic material [141, 142], which is capable of producing stronger fields through the use of high saturation yoke material. Despite this, the pure PM Halbach consisting only of hard ferromagnets is still commonly used.

There is growing interest in short period undulators (*micro-undulators*) [144, 143, 142, 103], facilitated by MEMS (microelectromechanical systems) and other modern fabrication techniques, with researchers seeking to decrease the period length to achieve concomitant reductions in free-electron laser (FEL) or light source size. In this context though, conventional Halbach undulators suffer from a distinct disadvantage: for a given feature size achievable by a particular machining or fabrication process, a conventional Halbach array will have twice the period of a simple up-down lattice ($M' = 2$ in the terminology of [134]). This limitation motivates this exploration of triangle based Halbach arrays. The triangle Halbach involves less magnetic material per period than an $M' = 4$ undulator so lower fields are achieved, with the advantage that for a given feature size the undulator period is halved. Existing triangular-magnet Halbach arrays have relied on isosceles triangle geometries [154, 155, 156], leading to intrinsic symmetries.

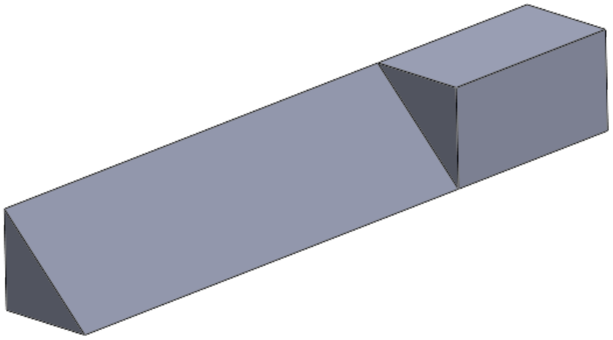

Figure 4.12: An example right angle triangle magnet.

Unfortunately, such arrays are difficult to fabricate, especially at micro-undulator length scales. To mitigate such challenges, simplification of the component magnets and their assembly must be re-examined. As such, here we discuss Halbach arrays based on right triangles, which feature easier fabrication while maintaining comparable performance to the isosceles case and superior performance to $M' = 2$ arrays. Fabrication might begin with bar magnets, manufactured to a high degree of accuracy, parallelism, and perpendicularity using standard, scalable machining processes like surface grinding. By using a through-bulk cutting technique like electrical discharge machining or laser machining along the hypotenuse a right angle triangle prism can be produced that is intrinsically indexed to the remaining, square section (Figure 4.12). These square parts can be indexed to each other and to flat surfaces very accurately, without relying on the non-ground hypotenuse surfaces.

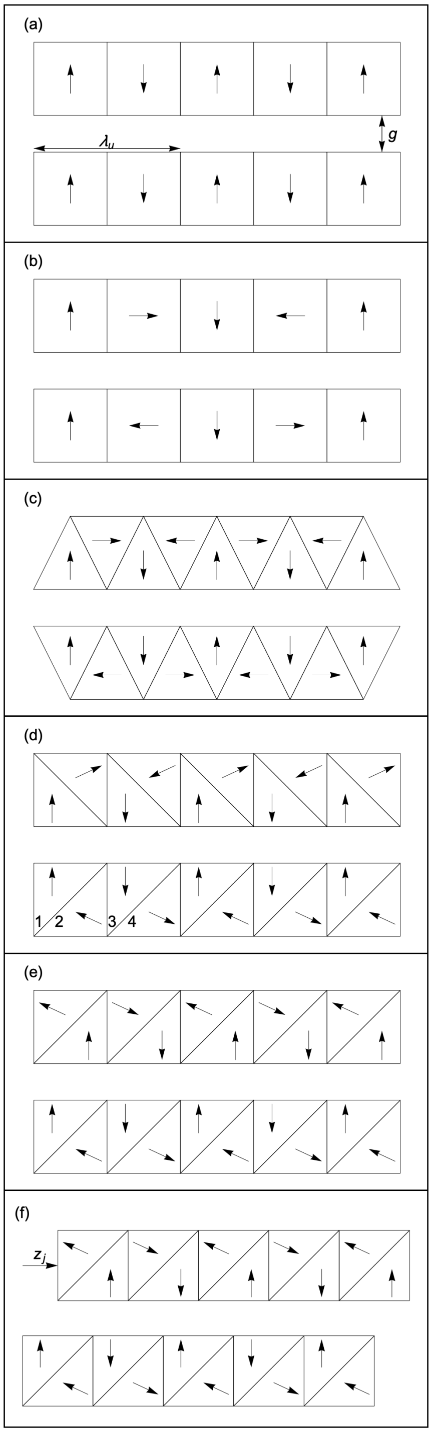

Figure 4.13: Examples of the undulator configurations. (a) $M' = 2$ array, (b) $M' = 4$ array, (c) isosceles triangles, (d) reflection symmetric right triangles, (e) rotationally symmetric right triangles, and (f) rotationally symmetric right triangles with jaw translation (positive z_j is illustrated but negative is typically used).

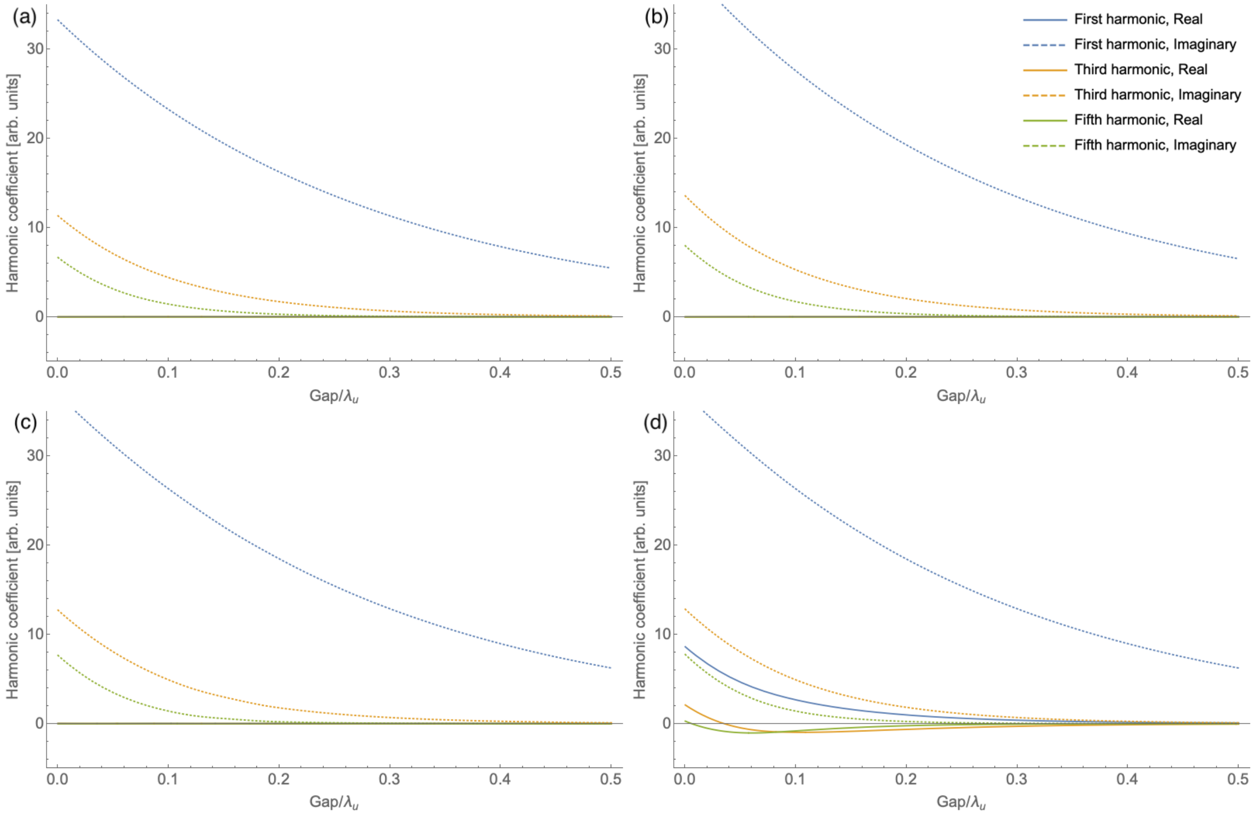

Figure 4.14: Harmonic coefficients of the on axis field for (a) $M' = 2$, (b) isosceles triangle, (c) rotation symmetric right triangle, and (d) reflection symmetric right triangle.

4.7.2 Simulation setup

4.7.2.1 Overview

Four configurations of magnets will be considered: the $M' = 2$ (up-down) array, isosceles triangles, reflection symmetric right triangles, and rotationally symmetric right triangles. Each case has an undulator period, λ_u, equal to twice the minimum feature size, and all cases have an equal volume of magnetic material per period, specifically each magnet has a height equal to half a period. These cases are shown in Figure 4.13 along with the $M' = 4$ configuration, which has λ_u equal to four times the minimum feature size. All simulations are performed using the magnetostatics code, RADIA [88] with the material properties of neodymium magnets.

4.7.2.2 Magnetization vector

The ideal magnetization vector as a function of longitudinal position, z, for a Halbach array [135] is simply $\hat{m} = e^{izk_z}$ where $k_z = 2\pi/\lambda_u$. In the case of undulators in actual experimental realization, however, the magnets are discrete elements, each with a discrete, constant magnetization. With M' square magnets per period each magnet's magnetization vector is rotated by a fixed amount from the previous one, meaning that the magnetization of the n^{th} magnet is given by $e^{i2\pi n/M'}$. This rule extends to the isosceles case, which exhibits the same rotation as $M' = 4$ arrays. However, applying this constant rotation to right angle arrays leads to sub-optimal fields. Instead, the ideal vector field described by

$$\hat{m}(z, y) = e^{i(zk_z+\phi)}, \tag{4.29}$$

where ϕ is a variable utilized to independently control the phase, is averaged over the region of each discrete magnet and normalized to one. For magnet $n = 1$ (see Figure 4.13d) this average vector is

$$\langle \vec{m} \rangle_{n=1} = \frac{\int_0^{\lambda_u/2} \int_z^{\lambda_u/2} \hat{m}(z, y)\, \mathrm{d}y\, \mathrm{d}z}{\lambda_u^2/8}, \tag{4.30}$$

which normalizes to the unit vector

$$\langle \hat{m} \rangle_{n=1} = \frac{\langle \vec{m} \rangle_{n=1}}{|\langle \vec{m} \rangle_{n=1}|} = \frac{(2\cos\phi - \pi\sin\phi)\hat{z} + (\pi\cos\phi + 2\sin\phi)\hat{y}}{\sqrt{4+\pi^2}}, \tag{4.31}$$

The same approach for magnet $n = 2$ yields

$$\langle \hat{m} \rangle_{n=2} = \frac{-(2\cos\phi + \pi\sin\phi)\hat{z} + (\pi\cos\phi - 2\sin\phi)\hat{y}}{\sqrt{4+\pi^2}}. \tag{4.32}$$

The angle between these vectors is independent of ϕ and equal to $\pi - 2\tan^{-1}(\pi/2) \approx 64.96°$. Magnets 3 and 4 have magnetization vectors $\langle \hat{m} \rangle_{n=3} = -\langle \hat{m} \rangle_{n=1}$ and $\langle \hat{m} \rangle_{n=4} = -\langle \hat{m} \rangle_{n=2}$ respectively. Using the angles from this approach enhances the performance over the use of naive, 90° rotations and is discussed in later sections. This approach can be extended to permit the calculation of the rms deviation between the discrete magnet's magnetization and the ideal field of equation (4.29), with these results shown in Table 4.3 (the rms deviation is independent of ϕ). As will be shown later, this deviation is a predictor of the undulator strength.

Geometry	RMS deviation
$M' = 2$	0.109
Right angle (90°)	0.096
Right angle (optimized)	0.093
Isosceles	0.083
$M' = 4$	0.062
$M' \to \infty$	$\to 0$

Table 4.3: RMS deviation between ideal Halbach magnetization and discrete magnet vector, by geometry

4.7.2.3 Impact of jaw translation

The length scale is normalized to the period of the undulator, λ_u, leaving two free variables for each configuration: the gap, g, and the longitudinal translation between the jaws, z_j. The jaw gap is a commonly manipulated parameter for real world undulators: increasing the gap reduces the field on axis and also decreases the relative contributions of higher harmonics. Longitudinal translation is not often considered in the context of linear undulators, though it is employed in some adjustable helical undulators [89, 157, 137]). For existing undulators which are symmetric (i.e. $M' = 2$, $M' = 4$, and isosceles triangle) translations can serve to reduce the field strength at the cost of introducing errors [158]. As will be demonstrated below, however, for right triangle arrays, adjusting this parameter can be used to optimize the undulator's magnetic performance. All reflection symmetric cases maximize vertical field and minimize longitudinal fields at zero translation, but rotation symmetric undulators are optimized with a different, non-vanishing z_j, dependent on gap. Based on this study, a heuristic guide for the optimized translation is given by

$$z_j\,[\lambda_u] \approx -0.025\ln(g\,[\lambda_u]) - 0.14. \tag{4.33}$$

This approximation gives a coefficient of determination (R^2 value) of 0.9996 for values of g ranging from 0.02 λ_u to 0.5 λ_u.

4.7.3 Results

4.7.3.1 Strength comparison

To compare between the different configurations, both the magnitude and quality of the on-axis fields will be considered. It is typical to characterize the strength of undulators and wigglers in terms of a unitless parameter called the K-value, sometimes also termed the *strength parameter*. This parameter is the normalized (to $m_e c$) vector potential, and thus is also equal in amplitude to the largest transverse momentum due to undulator-derived deflections. In this way, one sees that K may be calculated by finding the maximum deflection angle induced by the undulator multiplied by the Lorentz factor, γ. Using the small angle approximation and neglecting non-vertical fields as in [89], the equation of motion for an electron in the oscillation plane is:

$$\frac{d^2x}{ds^2} = \frac{e}{\gamma m_e c} B_y(s), \tag{4.34}$$

where e is the electron charge, m_e is the electron mass, c is the speed of light, and $B_y(s)$ is the vertical field along the undulator. The maximum deflection angle and therefore the K-value is given by:

$$\left.\frac{dx}{ds}\right|_{\max} = \frac{1}{2}\int_0^{\lambda_u/2} \frac{e}{\gamma m_e c} B_y(s)\,\mathrm{d}s \equiv \frac{K}{\gamma}. \tag{4.35}$$

For the idealized case of an undulator with a perfectly sinusoidal field, $B_y(s) = -B_0 \sin(2\pi s/\lambda_u)$, the K-value is

$$K = \frac{B_0 e \lambda_u}{2\pi m_e c} \approx 93.36 B_0\,[T]\,\lambda_u[m]. \tag{4.36}$$

Equation 4.35 will be used to calculate the relative strengths of different undulator configurations. However, K depends on the magnetic material selected and λ_u in absolute units so, to avoid confusion, K will not be directly utilized in absolute scale, but instead the configurations will be compared in relative terms.

Over gap values ranging from 0.02 λ_u to 0.5 λ_u an isosceles array gives integrated fields approximately 19% higher than a $M' = 2$ array while optimized right triangle arrays (of both rotation and reflection symmetries) give integrated fields approximately 13% higher than an $M' = 2$ array. Using an unoptimized, 90° magnetization vector rotation yields a 10% enhancement over $M' = 2$. This hierarchy of strength is consistent the rms deviations between the magnetization vector as compared with the ideal configuration detailed in Table 4.3.

4.7.3.2 Quality comparison

The quality of the on-axis undulator field is sometimes described by taking a Fourier decomposition [159, 160, 161] and inspecting the harmonic components. In typical undulators, the even harmonics are negligible and the coefficients of the harmonics are only for the sine contribution. In the case of right-triangle arrays though, symmetries have been broken so, although the integrated field per period will always be zero (*i.e.* no net deflection of a beam) and while there are still no even harmonics, there may be non-negligible complex components. The coefficients for the first, third, and fifth harmonics are shown for $M' = 2$, isosceles triangle, rotation symmetric right triangle, and reflection symmetric right triangle arrays as functions of the gap in Figure 4.14. It can be observed that, as noted, the first harmonic dominates at larger gap sizes at the cost of total field.

Such harmonics are not necessarily destructive and may perhaps even be valuable; previous research has used undulator harmonics to adjust the radiated spectrum [160] and to employ the inverse free-electron laser (IFEL) mechanism [162] at lower energy. With these issues in mind, z_j was then varied to maximize higher harmonics rather than the fundamental. The results are similar to that of the fundamental, with the third and fifth harmonics of the isosceles array approximately 20% higher than the $M' = 2$ array and right triangle arrays approximately 14% higher than the $M' = 2$ array.

4.7.4 Conclusions

A new variant of the Halbach array undulator comprised of right triangle magnets has been described and compared to existing options including isosceles triangle arrays and up-down ($M' = 2$) arrays. Such devices can offer integrated magnetic field strengths 13% higher than $M' = 2$ arrays with no increase in undulator period while remaining easier to fabricate than isosceles triangle arrays, which offer a 19% enhancement over $M' = 2$. These arrays lack some of the symmetries found in more conventional Halbach undulators, requiring the optimization of longitudinal jaw translation and introducing previously forbidden harmonic components. The use of these harmonics to tune the radiated spectrum or drive the IFEL mechanism means, in some cases, that higher harmonic content is desirable; these right triangle arrays similarly outperform standard $M' = 2$ arrays at the third order. These new configurations may be fabricated by today's MEMS manufacturing techniques to be used in the construction of the next generation of compact light sources [150].

REFERENCES

[1] J. M. J. Madey. Stimulated emission of bremsstrahlung in a periodic magnetic field. *Journal of Applied Physics*, 42(5):1906–1913, 1971.

[2] D. A. G. Deacon, L. R. Elias, J. M. J. Madey, G. J. Ramian, H. A. Schwettman, and T. I. Smith. First Operation of a Free-Electron Laser. *Physical Review Letters*, 38(16), 1977.

[3] K.-J. Kim, Z. Huang, and R. Lindberg. *Synchrotron Radiation and Free-Electron Lasers*. Cambridge University Press, Cambridge, UK, 2017.

[4] Z. Huang and K.-J. Kim. Review of x-ray free-electron laser theory. *Physical Review Special Topics - Accelerators and Beams*, 10(3):1–26, 2007.

[5] J. Arthur, P. Anfinrud, P Audebert, K. Bane, I. Ben-Zvi, V. Bharadwaj, R. Bionta, and P. Bolton. Linac Coherent Light Source (LCLS) Conceptual Design Report. *SLAC-R-593*, 2002.

[6] T. Tajima and J. M. Dawson. Laser Electron Accelerator. *Physical Review Letters*, 43(4):267–270, 1979.

[7] V. Malka, S. Fritzler, E. Lefebvre, M. M. Aleonard, F. Burgy, J. P. Chambaret, J. F. Chemin, K. Krushelnick, G. Malka, S. P.D. Mangles, Z. Najmudin, M. Pittman, J. P. Rousseau, J. N. Scheurer, B. Walton, and A. E. Dangor. Electron acceleration by a wake field forced by an intense ultrashort laser pulse. *Science*, 298(5598):1596–1600, 2002.

[8] S. P. D. Mangles, C. D. Murphy, Z. Najmudin, A. G. R. Thomas, J. L. Collier, A. E. Dangor, E. J. Divall, P. S. Foster, J. G. Gallacher, C. J. Hooker, D. A. Jaroszynski, A. J. Langley, W. B. Mori, P. A. Norreys, F. S. Tsung, R. Viskup, B. R. Walton, and K. Krushelnick. Monoenergetic beams of relativistic electrons from intense laser-plasma interactions. *Nature*, 431(September):535–538, 2004.

[9] J. Faure, Y. Glinec, A. Pukhov, S. Kiselev, S. Gordienko, E. Lefebvre, J.-P. Rousseau, F. Burgy, and V. Malka. A laser plasma accelerator producing monoenergetic electron beams. *Nature*, 431(September):541–544, 2004.

[10] C. G. R. Geddes, Cs. Toth, J. van Tilborg, E. Esarey, C. B. Schroeder, D Bruhwiler, C Nieter, J Cary, and W. P. Leemans. High-quality electron beams from a laser

wakefield accelerator using plasma-channel guiding. *Nature*, 431(September):541–544, 2004.

[11] A. J. Gonsalves, K. Nakamura, J. Daniels, C. Benedetti, C. Pieronek, T. C.H. De Raadt, S. Steinke, J. H. Bin, S. S. Bulanov, J. Van Tilborg, C. G.R. Geddes, C. B. Schroeder, Cs Tóth, E. Esarey, K. Swanson, L. Fan-Chiang, G. Bagdasarov, N. Bobrova, V. Gasilov, G. Korn, P. Sasorov, and W. P. Leemans. Petawatt Laser Guiding and Electron Beam Acceleration to 8 GeV in a Laser-Heated Capillary Discharge Waveguide. *Physical Review Letters*, 122(8):84801, 2019.

[12] W. P. Leemans, B. Nagler, A. J. Gonsalves, Cs Tóth, K. Nakamura, C. G.R. Geddes, E. Esarey, C. B. Schroeder, and S. M. Hooker. GeV electron beams from a centimetre-scale accelerator. *Nature Physics*, 2(10):696–699, 2006.

[13] Z. Qin, C. Yu, W. Wang, J. Liu, W. Li, R. Qi, Z. Zhang, J. Liu, M. Fang, K. Feng, Y. Wu, L. Ke, Y. Chen, Y. Xu, Y. Leng, C. Wang, R. Li, and Z. Xu. Ultralow-emittance measurement of high-quality electron beams from a laser wakefield accelerator. *Physics of Plasmas*, 25(2), 2018.

[14] W. T. Wang, W. T. Li, J. S. Liu, Z. J. Zhang, R. Qi, C. H. Yu, J. Q. Liu, M. Fang, Z. Y. Qin, C. Wang, Y. Xu, F. X. Wu, Y. X. Leng, R. X. Li, and Z. Z. Xu. High-Brightness High-Energy Electron Beams from a Laser Wakefield Accelerator via Energy Chirp Control. *Physical Review Letters*, 117(12), 2016.

[15] Z. Huang, Y. Ding, and C. B. Schroeder. Compact X-ray free-electron laser from a laser-plasma accelerator using a transverse-gradient undulator. *Physical Review Letters*, 109(20):1–5, 2012.

[16] T. Liu, T. Zhang, B. Liu, D. Wang, Z. Huang, and J. Liu. Beam transport line of the LPA-FEL facility based on transverse gradient undulator. *IPAC 2016 - Proceedings of the 7th International Particle Accelerator Conference*, pages 3287–3290, 2016.

[17] T.-Y. Lee. Storage ring based x-ray FEL oscillator. *AIP Conference Proceedings*, 2054(January), 2019.

[18] A. R. Maier, A. Meseck, S. Reiche, C. B. Schroeder, T. Seggebrock, and F. Gruner. Demonstration scheme for a laser-plasma-driven free-electron laser. *Physical Review X*, 2(3):1–7, 2012.

[19] C. B. Schroeder, E. Esarey, W. P. Leemans, J. Van Tilborg, F. J. Uner, A. R. Maier,

Y. Ding, and Z. Huang. Free-electron lasers driven by laser-plasma accelerators using decompression or dispersion. *FEL 2013: Proceedings of the 35th International Free-Electron Laser Conference*, 0(2):117–121, 2013.

[20] T. Seggebrock, A. R. Maier, I. Dornmair, and F. Grüner. Bunch decompression for laser-plasma driven free-electron laser demonstration schemes. *Physical Review Special Topics - Accelerators and Beams*, 16(7):1–9, 2013.

[21] J. van Tilborg. A compact laser-plasma-accelerator-based FEL for ultra-fast hyper-spectral experiments. *DOE BES Early Career Research Proposal*, 2015.

[22] M. Geitz. Bunch Length Measurements. *Proc. DIPAC 1999*, pages 1–5, 1999.

[23] C. Martínez. *Determination of Longitudinal Electron Bunch Lengths on Picosecond Time Scales*. Phd thesis, Universitat Politecnica de Catalunya, 1999.

[24] M. C. Downer and R. Zgadzaj. Diagnostics for plasma-based electron accelerators. *Reviews of Modern Physics*, 90(3):35002, 2018.

[25] V. Ginzburg and I. Frank. Theory of Transition Radiation. *Sov. Phys. JETP*, 1946.

[26] J. D. Jackson. *Classical Electrodynamics*. Wiley, New York, 3rd edition, 1998.

[27] M. L. Ter-Mikaelian. *High-Energy Electromagnetic Processes in Condensed Media*. Wiley-Interscience, New York, 1972.

[28] S. Casalbuoni, B. Schmidt, P. Schmuser, V. Arsov, and S. Wesch. Ultrabroadband terahertz source and beamline based on coherent transition radiation. *Physical Review Special Topics - Accelerators and Beams*, 12(3):1–13, 2009.

[29] C. Settakorn. Generation and Use of Coherent Transition Radiation from Short Electron Bunches. *SLAC-Report-576*, 2001.

[30] U. Happek, A. J. Sievers, and E. B. Blum. Observation of coherent transition radiation. *Physical Review Letters*, 67(21):2962–2965, 1991.

[31] Private communication with Jeroen van Tilborg.

[32] H.-C. Lihn, P. Kung, C. Settakorn, H. Wiedemann, and D. Bocek. Measurement of

subpicosecond electron pulses. *Physical Review E*, 53(6):6413–6418, 1996.

[33] I. Nozawa, K. Kan, J. Yang, A. Ogata, T. Kondoh, M. Gohdo, K. Norizawa, H. Kobayashi, H. Shibata, S. Gonda, and Y. Yoshida. Measurement of 20 fs bunch length using coherent transition radiation. *Physical Review Special Topics - Accelerators and Beams*, 17(7):072803, 2014.

[34] J. Thangaraj, G. Andonian, R. Thurman-Keup, J. Ruan, A. S. Johnson, A. Lumpkin, J. Santucci, T. Maxwell, A. Murokh, M. Ruelas, and A. Ovodenko. Demonstration of a real-time interferometer as a bunch-length monitor in a high-current electron beam accelerator. *Review of Scientific Instruments*, 83(4):1–6, 2012.

[35] G. Andonian, S. Boucher, P. Frigola, A. Murokh, and G. Travish. A real-time bunch length terahertz interferometer. *Proceedings EPAC08, Genua, Italy*, pages 1218–1220, 2008.

[36] X. E. Lu, C. E. Tang, R. E. Li, H. To, G. Andonian, and P. Musumeci. Generation and measurement of velocity bunched ultrashort bunch of pC charge. *Physical Review Special Topics - Accelerators and Beams*, 18(3):1–9, 2015.

[37] S. K. Barber, J. Van Tilborg, C. B. Schroeder, R. Lehe, H. E. Tsai, K. K. Swanson, S. Steinke, K. Nakamura, C. G.R. Geddes, C. Benedetti, E. Esarey, and W. P. Leemans. Parametric emittance measurements of electron beams produced by a laser plasma accelerator. *Plasma Physics and Controlled Fusion*, 60(5), 2018.

[38] S. K. Barber, J. Van Tilborg, C. B. Schroeder, R. Lehe, H. E. Tsai, K. K. Swanson, S. Steinke, K. Nakamura, C. G.R. Geddes, C. Benedetti, E. Esarey, and W. P. Leemans. Measured Emittance Dependence on the Injection Method in Laser Plasma Accelerators. *Physical Review Letters*, 119(10):1–5, 2017.

[39] C. Thaury, E. Guillaume, A. Lifschitz, K. Ta Phuoc, M. Hansson, G. Grittani, J. Gautier, J. P. Goddet, A. Tafzi, O. Lundh, and V. Malka. Shock assisted ionization injection in laser-plasma accelerators. *Scientific Reports*, 5:2–8, 2015.

[40] J. Faure, C. Rechatin, A. Norlin, A. Lifschitz, Y. Glinec, and V. Malka. Controlled injection and acceleration of electrons in plasma wakefields by colliding laser pulses. *Nature*, 444(7120):737–739, 2006.

[41] S. P. D. Mangles, A. G. R. Thomas, O. Lundh, F. Lindau, M. C. Kaluza, A. Persson, C. G. Wahlström, K. Krushelnick, and Z. Najmudin. On the stability of laser wakefield

electron accelerators in the monoenergetic regime. *Physics of Plasmas*, 14(5), 2007.

[42] Janos Technology Inc. Transmission Ranges for Optical Materials. *www.janostech.com*, 2018.

[43] Crystran Ltd. Optical Materials. *www.crystran.co.uk*, 2018.

[44] T. J. Maxwell and C. Behrens. Middle-infrared prism spectrometer for single-shot bunch length diagnostics at the LCLS. *Proceedings of IBIC2012, Tsukuba, Japan*, pages 463–467, 2012.

[45] T. J. Maxwell, C. Behrens, Y. Ding, A. S. Fisher, J. Frisch, Z. Huang, and H. Loos. Coherent-radiation spectroscopy of few-femtosecond electron bunches using a middle-infrared prism spectrometer. *Physical Review Letters*, 111(18):1–5, 2013.

[46] International Crystal Laboratories. Thallium Bromoiodide (KRS-5) Optical Crystals. *www.internationalcrystal.net*, 2018.

[47] Thorlabs Inc. [Various]. *www.thorlabs.com*, 2018.

[48] S. J. Pedrotti, L. M. Pedrotti, and S. P. Pedrotti. *Introduction to Optics*. Pearson, 3rd editio edition, 2006.

[49] W. S. Rodney and I. H. Malitson. Refraction and Dispersion of Thallium Bromide Iodide. *Journal of the Optical Society of America*, 46(11):956, 1956.

[50] Zemax LLC. Zemax OpticStudio, 2016.

[51] Private communication with Gerard Andonian.

[52] Vincent Associates. Uniblitz Optical Shutters. *www.uniblitz.com*, 2019.

[53] M. Planck. *The theory of heat radiation*. P. Blakiston's Son & Co., Philadelphia, 1914.

[54] J. Stefan. On the relationship between thermal radiation and temperature. *Bulletins from the Sessions of the Vienna Academy of Sciences*, pages 391–428, 1879.

[55] Private communication with Sam Barber.

[56] J. Rosenzweig. *Fundamentals of Beam Physics.* Oxford University Press, Oxford, 2003.

[57] G. Paraskaki. *Bunch Compressor Design for X-FEL & Improvement of DFS algorithm for the FERMI FEL Free Electron Lasers.* PhD thesis, Aristotle University of Thesaloniki, 2016.

[58] RadiaBeam Technologies LLC. [Various]. *www.radiabeam.com*, 2018.

[59] S. Di Mitri. Bunch-length Compressors. *Proceedings of the CAS-CERN Accelerator School: Free Electron Lasers and Energy Recovery Linacs*, 1(June 2016):363–380, 2016.

[60] N. Majernik, S. Barber, J. van Tilborg, J. Rosenzweig, and W. P. Leemans. Optimization of Low Aspect Ratio, Iron Dominated Dipole Magnets. *Physical Review Accelerators and Beams*, 22(3):32401, 2019.

[61] J. Tanabe. Iron Dominated Electromagnets: Design, Fabrication, Assembly and Measurements. *SLAC-R-754*, 2005.

[62] S. Caspi, D. Arbelaez, L. Brouwer, S. Gourlay, S. Prestemon, and B. Auchmann. Design of a canted-cosine-theta superconducting dipole magnet for future colliders. *IEEE Transactions on Applied Superconductivity*, 27(4):14–18, 2017.

[63] M. Karppinen, N. Andreev, G. Apollinari, B. Auchmann, E. Barzi, R. Bossert, V. V. Kashikhin, A. Nobrega, I. Novitski, L. Rossi, D. Smekens, and A. V. Zlobin. Design of 11 T twin-aperture Nb3Sn dipole demonstrator magnet for LHC upgrades. *IEEE Transactions on Applied Superconductivity*, 22(3):3–6, 2012.

[64] K. Halbach. Application of permanent magnets in accelerators and electron storage rings (invited). *Journal of Applied Physics*, 57(8):3605–3608, 1985.

[65] A. C. Boxer, R. Bergmann, J. L. Ellsworth, D. T. Garnier, J. Kesner, M. E. Mauel, and P. Woskov. Turbulent inward pinch of plasma confined by a levitated dipole magnet. *Nature Physics*, 6(3):207–212, 2010.

[66] E. Zavattini, G. Zavattini, G. Ruoso, E. Polacco, E. Milotti, M. Karuza, U. Gastaldi, G. Di Domenico, F. Della Valle, R. Cimino, S. Carusotto, G. Cantatore, and M. Bregant. Experimental observation of optical rotation generated in vacuum by a magnetic field. *Physical Review Letters*, 96(11):1–5, 2006.

[67] E. R. Andrew. *Nuclear Magnetic Resonance.* Cambridge University Press, Cambridge, UK, 2009.

[68] G. Moresi and R. Magin. Miniature permanent magnet for table-top NMR. *Concepts in Magnetic Resonance Part B: Magnetic Resonance Engineering*, 19(1):35–43, 2003.

[69] F. Cottone, H. Vocca, and L. Gammaitoni. Nonlinear energy harvesting. *Physical Review Letters*, 102(8):1–4, 2009.

[70] A. Brahme. Design principles and clinical possibilities with a new generation of radiation therapy equipment: A review. *Acta Oncologica*, 26(6):403–412, 1987.

[71] D. Schardt, T. Elsässer, and D. Schulz-Ertner. Heavy-ion tumor therapy: Physical and radiobiological benefits. *Reviews of Modern Physics*, 82(1):383–425, 2010.

[72] W. P. Leemans, P. Catravas, E. Esarey, C. G.R. Geddes, C. Toth, R. Trines, C. B. Schroeder, B. A. Shadwick, J. van Tilborg, and J. Faure. Electron-yield enhancement in a laser-wakefield accelerator driven by asymmetric laser pulses. *Physical Review Letters*, 89(17):174802/1–174802/4, 2002.

[73] W. P. Leemans, B Nagler, A. J. Gonsalves, Cs. Toth, K. Nakamura, C. G.R. Geddes, E. Esarey, C. B. Schroeder, and S M Hooker. GeV electron beams from a cm-scale accelerator. *LBNL*, 2014.

[74] E. Esarey, C. B. Schroeder, and W. P. Leemans. Physics of laser-driven plasma-based electron accelerators. *Reviews of Modern Physics*, 81(3):1229–1285, 2009.

[75] J. H. Mathews and R. W. Howell. *Complex Analysis : for Mathematics and Engineering.* Jones and Bartlett Pub. Inc, Sudbury, MA, 6th edition, 2012.

[76] E. T. Scharlemann. Wiggle plane focusing in linear wigglers. *Journal of Applied Physics*, 58(6):2154–2161, 1985.

[77] J. S. Ryu, Y. Yao, C. S. Koh, and Y. J. Shin. 3-D optimal shape design of pole piece in permanent magnet MRI using parameterized nonlinear design sensitivity analysis. *IEEE Transactions on Magnetics*, 42(4):1351–1354, 2006.

[78] A. Saleem. *Design and optimization of a magnet pole for Magnetic Resonant Imaging.* PhD thesis, Aalto University, 2018.

[79] J. Kennedy and R. Eberhart. Particle Swarm Optimization. *Proceedings of IEEE International Converence on Neural Networks*, IV:1942–1948, 1995.

[80] R. Holsinger and K. Halbach. Poisson Superfish, 2013.

[81] Y. Baghzouz. Magnetic Circuits. *www.egr.unlv.edu*, 2019.

[82] Private communication with James Rosenzweig.

[83] Kepco Inc. Series BOP-MG 1KW High Power Models. *www.KepcoPower.com*, 2018.

[84] C. Kittel. *Introduction to Solid State Physics*. John Wiley & Sons, Inc, New York, 8 edition, 2005.

[85] Standard Specification for Standard Nominal Diameters and Cross-Sectional Areas of AWG Sizes of Solid Round Wires Used as Electrical Conductors, 1994.

[86] Engineering Toolbox. Overall Heat Transfer Coefficients for Fluids - Heat Exchanger Surface Combinations. *www.engineeringtoolbox.com*, 2019.

[87] D. Meeker. Finite element method magnetics (FEMM), 2010.

[88] O. Chubar, P. Elleaume, and J. Chavanne. RADIA, 1997.

[89] J. A. Clarke. *The Science and Technology of Undulators and Wigglers*. Oxford University Press, 2004.

[90] M. Xie. Exact and variational solutions of 3D eigenmodes in high gain FELs. *Proceedings of 1999 Free Electron Laser Conference*, 1999.

[91] M. Xie. Exact and variational solutions of 3D eigenmodes in high gain FELs. *Nuclear Instruments and Methods in Physics Research, Section A: Accelerators, Spectrometers, Detectors and Associated Equipment*, 445(1-3):59–66, 2000.

[92] C. Pellegrini. X-ray free-electron lasers: From dreams to reality. *Physica Scripta*, 2016(T169), 2016.

[93] LightSources.org. Light sources of the world. *www.LightSources.org*, 2019.

[94] I. Ben-Zvi, Z. Y. Jiang, G. Ingold, L. H. Yu, and W. B. Sampson. The performance of a superconducting micro-undulator prototype. *Nuclear Inst. and Methods in Physics Research, A*, 297(1-2):301–305, 1990.

[95] Y. Ivanyushenkov, E. Baynham, T. Bradshaw, and Et al. Development of a superconducting helical undulator for the ILC positron source. *EPAC 2006 - Contributions to the Proceedings*, pages 706–708, 2006.

[96] Y. Ivanyushenkov, K. Harkay, M. Abliz, and Et al. Development and operating experience of a short-period superconducting undulator at the Advanced Photon Source. *Physical Review Special Topics - Accelerators and Beams*, 18(4):1–13, 2015.

[97] T. Tanaka, T. Hara, R. Tsuru, D. Iwaki, T. Bizen, X. Marechal, T. Seike, and H. Kitamura. Utilization of bulk high-temperature superconductors for shorter-period synchrotron radiation sources. *Superconductor Science and Technology*, 19(7), 2006.

[98] R. Kinjo, T. Kii, H. Zen, K. Higashimura, K. Masuda, K. Nagasaki, H. Ohgaki, and Y. U. Jeong. A bulk high-TC superconductor staggered array undulator. *30th International Free Electron Laser Conference, FEL 2008*, pages 473–476, 2008.

[99] T. Kii, R. Kinjo, N. Kimura, M. Shibata, M. A. Bakr, Y. W. Choi, M. Omer, K. Yoshida, K. Ishida, T. Komai, K. Shimahashi, T. Sonobe, H. Zen, K. Masuda, and H. Ohgaki. Low-temperature operation of a bulk HTSC staggered array undulator. *IEEE Transactions on Applied Superconductivity*, 22(3):11–14, 2012.

[100] A. A. Varfolomeev, A. S. Khlebnikov, S. N. Ivanchenkov, N. S. Osmanov, and A. H. Hairetdinov. Strong Magnetic Field Microundulator with Permanent Magnets Inserted into a Solenoid. *Nuclear Inst. and Methods in Physics Research, A*, 331:745–747, 1993.

[101] N. Balal, I. V. Bandurkin, V. L. Bratman, and A. E. Fedotov. Helical undulator based on partial redistribution of uniform magnetic field. *Physical Review Accelerators and Beams*, 20(12):1–5, 2017.

[102] J. Harrison, A. Joshi, Y. Hwang, O. Paydar, J. Lake, P. Musumeci, and R. N. Candler. Surface-micromachined electromagnets for 100 μm-scale undulators and focusing optics. *Physics Procedia*, 52:19–26, 2014.

[103] B. A. Peterson, O. D. Oniku, W. C. Patterson, D. Le Roy, A. Garraud, F. Herrault, N. M. Dempsey, D. P. Arnold, and M. G. Allen. Technology development for short-period magnetic undulators. *Physics Procedia*, 52:36–45, 2014.

[104] N. Majernik and J. B. Rosenzweig. Design of Comb Fabricated Halbach Undulators. *Instruments*, 3(58), 2019.

[105] N. Majernik and J. B. Rosenzweig. Halbach undulators using right triangular magnets. *Physical Review Accelerators and Beams*, 22(092401), 2019.

[106] C. Chang, M. Shumail, S. Tantawi, J. Neilson, and C. Pellegrini. Electron dynamics and transverse-kick elimination in a high-field short-period helical microwave undulator. *Applied Physics Letters*, 101(16), 2012.

[107] S. Tantawi, M. Shumail, J. Neilson, G. Bowden, C. Chang, E. Hemsing, and M. Dunning. Experimental demonstration of a tunable microwave undulator. *Physical Review Letters*, 112(16):1–5, 2014.

[108] S. V. Kuzikov, Y. Jiang, T. C. Marshall, G. V. Sotnikov, and J. L. Hirshfield. Configurations for short period rf undulators. *Physical Review Special Topics - Accelerators and Beams*, 16(7):1–12, 2013.

[109] F. H. O'Shea, G. Marcus, J. B. Rosenzweig, M. Scheer, J. Bahrdt, R. Weingartner, A. Gaupp, and F. Grüner. Short period, high field cryogenic undulator for extreme performance x-ray free electron lasers. *Physical Review Special Topics - Accelerators and Beams*, 13(7):1–12, 2010.

[110] J. Chavanne, G. Lebec, C. Penel, F. Revol, and C. Kitegi. Cryogenic permanent magnet undulators. *AIP Conference Proceedings*, 1234:25–28, 2010.

[111] C. Benabderrahmane, P. Berteaud, M. Valléau, C. Kitegi, K. Tavakoli, N. Béchu, A. Mary, J. M. Filhol, and M. E. Couprie. Nd 2Fe 14B and Pr 2Fe 14B magnets characterisation and modelling for cryogenic permanent magnet undulator applications. *Nuclear Instruments and Methods in Physics Research, Section A: Accelerators, Spectrometers, Detectors and Associated Equipment*, 669:1–6, 2012.

[112] A. G. Afonin, V. T. Baranov, S. Bellucci, V. M. Biryukov, G. I. Britvich, V. N. Chepegin, Yu A. Chesnokov, C. Balasubramanian, G. Giannini, V. Guidi, Yu M. Ivanov, V. I. Kotov, A. Kushnirenko, V. A. Maisheev, C. Malagu, G. Martinelli, A. A. Petrunin, V. A. Pikalov, A. Raco, V. V. Skorobogatov, M. Stefancich, V. I. Terekhov, F. Tombolini, and D. Vincenzi. Crystal undulator experiment at IHEP. *Nuclear Instruments and Methods in Physics Research, Section B: Beam Interactions with Materials and Atoms*, 234(1-2):122–127, 2005.

[113] S. Bellucci, V. M. Biryukov, G. I. Britvich, Yu A. Chesnokov, C. Balasubramanian, G. Giannini, V. Guidi, Yu M. Ivanov, V. I. Kotov, V. A. Maisheev, C. Malagu, G. Martinelli, A. A. Petrunin, V. A. Pikalov, A. Raco, L. Silvi, V. V. Skorobogatov, M. Stefancich, F. Tombolini, and D. Vincenzi. Crystal undulator as a new compact source of radiation. *Physical Review Special Topics - Accelerators and Beams*, 7(2):15–19, 2004.

[114] J.-H Tan, Y.-F. Li, B.-J. Zhu, C.-Q. Zhu, J.-G. Wang, D.-Z. Li, X. Lu, Y.-T. Li, and L.-M. Chen. Short-period high-strength helical undulator by laser-driven bifilar capacitor coil. *Optics Express*, 27(21):29676, 2019.

[115] S. Wang, C. Clayton, B. Blue, E. Dodd, K. Marsh, W. Mori, C. Joshi, S. Lee, P. Muggli, T. Katsouleas, F. Decker, M. Hogan, R. Iverson, P. Raimondi, D. Walz, R. Siemann, and R. Assmann. X-ray emission from betatron motion in a plasma wiggler. *Physical Review Letters*, 88(13):135004, 2002.

[116] D. K. Johnson, D. Auerbach, I. Blumenfeld, C. D. Barnes, C. E. Clayton, F. J. Decker, S. Deng, P. Emma, M. J. Hogan, C. Huang, R. Ischebeck, R. Iverson, C. Joshi, T. C. Katsouleas, N. Kirby, P. Krejcik, W. Lu, K. A. Marsh, W. B. Mori, P. Muggli, C. L. O'Connell, E. Oz, R. H. Siemann, D. Walz, and M. Zhou. Positron production by X rays emitted by Betatron motion in a plasma wiggler. *Physical Review Letters*, 97(17):1–4, 2006.

[117] N. Majernik and J. Rosenzweig. Resonant excitation of betatron oscillations. *Nuclear Inst. and Methods in Physics Research, A*, 865(October 2016):91–94, 2017.

[118] M. Yabashi, H. Tanaka, and T. Ishikawa. Overview of the SACLA facility. *Journal of Synchrotron Radiation*, 22:477–484, 2015.

[119] DESY XFEL Project Group. The European X-ray Free-Electron Laser. *DESY 2006-097*, 2007.

[120] D. E. Kim, Y. G. Jung, W. W. Lee, K. H. Park, S. B. Lee, B. G. Oh, S. H. Jeong, H. G. Lee, H. S. Suh, H. S. Kang, I. S. Ko, and J. Pflueger. Development of PAL-XFEL undulator system. *Proceedings of IPAC2016, Busan, Korea*, THPOW045, 2016.

[121] C. J. Milne, T. Schietinger, M. Aiba, and Et al. SwissFEL: The Swiss X-ray Free Electron Laser. *Applied Sciences*, 7(7):1–57, 2017.

[122] S. Schreiber, B. Faatz, J. Feldhaus, K. Honkavaara, and R. Treusch. FEL user facility FLASH. *Proceedings of IPAC'10, Kyoto, Japan FEL*, pages 2149–2151, 2010.

[123] FERMI@Elettra Design Team. FERMI@Elettra Conceptual Design Report. *Sincrotrone Trieste*, 2007.

[124] S. Reiche. GENESIS 1.3: A fully 3D time-dependent FEL simulation code. *Nuclear Instruments and Methods in Physics Research, Section A: Accelerators, Spectrometers, Detectors and Associated Equipment*, 429(1):243–248, 1999.

[125] R. Carr, M. Cornacchia, P. Emma, H.-D. Nuhn, B. Poling, R. Ruland, E. Johnson, G. Rakowsky, J. Skaritka, S. Lidia, P. Duffy, M. Libkind, P. Frigola, A. Murokh, C. Pellegrini, J. Rosenzweig, and A. Tremaine. Visible-infrared self-amplified spontaneous emission amplifier free electron laser undulator. *Physical Review Special Topics - Accelerators and Beams*, 4(12):43–51, 2001.

[126] J. van Tilborg, S. K. Barber, F. Isono, C. B. Schroeder, E. Esarey, and W. P. Leemans. Free-electron lasers driven by laser plasma accelerators. *AIP Conference Proceedings*, 1812, 2017.

[127] G. R. Plateau, C. G.R. Geddes, D. B. Thorn, M. Chen, C. Benedetti, E. Esarey, A. J. Gonsalves, N. H. Matlis, K. Nakamura, S. Rykovanov, C. B. Schroeder, S. Shiraishi, T. Sokollik, J. Van Tilborg, Cs Toth, S. Trotsenko, T. S. Kim, M. Battaglia, Th Stöhlker, and W. P. Leemans. Low-emittance electron bunches from a laser-plasma accelerator measured using single-shot X-ray spectroscopy. *AIP Conference Proceedings*, 1507(August):278–283, 2012.

[128] R. Weingartner, S. Raith, A. Popp, S. Chou, J. Wenz, K. Khrennikov, M. Heigoldt, A. R. Maier, N. Kajumba, M. Fuchs, B. Zeitler, F. Krausz, S. Karsch, and F. Grüner. Ultralow emittance electron beams from a laser-wakefield accelerator. *Physical Review Special Topics - Accelerators and Beams*, 15(11):1–5, 2012.

[129] G. Golovin, S. Banerjee, S. Chen, N. Powers, C. Liu, W. Yan, J. Zhang, P. Zhang, B. Zhao, and D. Umstadter. Control and optimization of a staged laser-wakefield accelerator. *Nuclear Instruments and Methods in Physics Research, Section A: Accelerators, Spectrometers, Detectors and Associated Equipment*, 830:375–380, 2016.

[130] M. R. Islam, E. Brunetti, R. P. Shanks, B. Ersfeld, R. C. Issac, S. Cipiccia, M. P. Anania, G. H. Welsh, S. M. Wiggins, A. Noble, R. A. Cairns, G. Raj, and D. A. Jaroszynski. Near-threshold electron injection in the laser-plasma wakefield accelerator leading to femtosecond bunches. *New Journal of Physics*, 17(9):0–12, 2015.

[131] Z. Zhang, W. Li, J. Liu, W. Wang, C. Yu, Y. Tian, K. Nakajima, A. Deng, R. Qi, C. Wang, Z. Qin, M. Fang, J. Liu, C. Xia, R. Li, and Z. Xu. Energy spread mini-

mization in a cascaded laser wakefield accelerator via velocity bunching. *Physics of Plasmas*, 23(5), 2016.

[132] X. Li, P. A. P. Nghiem, and A. Mosnier. Toward low energy spread in plasma accelerators in quasilinear regime. *Physical Review Accelerators and Beams*, 21(11):111301, 2018.

[133] B. Hidding, G. Pretzler, J. B. Rosenzweig, T. Königstein, D. Schiller, and D. L. Bruhwiler. Ultracold electron bunch generation via plasma photocathode emission and acceleration in a beam-driven plasma blowout. *Physical Review Letters*, 108(3):1–5, 2012.

[134] K. Halbach. Design of Permanent Multipole Magnets with Oriented Rare Earth Cobalt Material. *Nuclear Instruments and Methods*, 169, 1980.

[135] K. Halbach. Physical and optical properties of rare earth cobalt magnets. *Nuclear Instruments and Methods*, 187(1):109–117, 1981.

[136] K. Halbach, J. Chin, E. Hoyer, H. Winick, R. Cronin, J. Yang, and Y. Zambre. A Permanent Magnet Undulator for SPEAR. *IEEE Transactions on Nuclear Science*, 28(3):3136–3138, 1981.

[137] S. Lidia and R. Carr. An elliptically-polarizing undulator with phase adjustable energy and polarization. *Nuclear Inst. and Methods in Physics Research, A*, 347(1-3):77–82, 1994.

[138] A. Murokh, R. Agustsson, M. Babzien, I. Ben-Zvi, L. Bertolini, K. Van Bibber, R. Carr, M. Cornacchia, P. Frigola, J. Hill, E. Johnson, L. Klaisner, G. Le Sage, M. Libkind, R. Malone, H. D. Nuhn, C. Pellegrini, S. Reiche, G. Rakowsky, J. Rosenzweig, R. Ruland, J. Skaritka, A. Toor, A. Tremaine, X. Wang, and V. Yakimenko. Results of the VISA SASE FEL experiment at 840 nm. *Nuclear Instruments and Methods in Physics Research, Section A: Accelerators, Spectrometers, Detectors and Associated Equipment*, 507(1-2):417–421, 2003.

[139] M. Kumada, Y. Iwashita, M. Aoki, and E. Sugiyama. The strongest permanent dipole magnet. *Proceedings of the 2003 Particle Accelerator Conference*, pages 1993–1995, 2004.

[140] J. K. Lim, P. Frigola, G. Travish, J. B. Rosenzweig, S. G. Anderson, W. J. Brown, J. S. Jacob, C. L. Robbins, and A. M. Tremaine. Adjustable, short focal length permanent-

magnet quadrupole based electron beam final focus system. *Physical Review Special Topics - Accelerators and Beams*, 8(7):1–17, 2005.

[141] P. Elleaume, J. Chavanne, and Bart Faatz. Design considerations for a 1 angstrom SASE undulator. *Nuclear Instruments and Methods in Physics Research, Section A: Accelerators, Spectrometers, Detectors and Associated Equipment*, 455(3):503–523, 2000.

[142] T. Eichner, F. Grüner, S. Becker, M. Fuchs, D. Habs, P. Kunz, R. Weingartner, H. Backe, U. Schramm, and W. Lauth. Miniature magnetic devices for laser-based, table-top free-electron lasers. *Physical Review Special Topics - Accelerators and Beams*, 10(8):1–9, 2007.

[143] G. Ramian, L. Elias, and I. Kimel. Micro-undulator FELS. *Nuclear Inst. and Methods in Physics Research, A*, 250(1-2):125–133, 1986.

[144] J. Harrison, A. Joshi, J. Lake, and R. Candler. Surface-micromachined magnetic undulator with period length between 10 m and 1 mm for advanced light sources. *Physical Review Accelerators and Beams*, 070703:1–16, 2012.

[145] R. Kinjo, M. Shibata, T. Kii, H. Zen, K. Masuda, K. Nagasaki, and H. Ohgaki. Demonstration of a high-field short-period undulator using bulk high-temperature superconductor. *Applied Physics Express*, 6(4), 2013.

[146] S. Yamamoto. Undulator Development Towards Very Short Period Lengths. *Synchrotron Radiation News*, 28(3):19–22, 2015.

[147] G. Brown, K. Halbach, J. Harris, and H. Winick. Wiggler and undulator magnets - A review. *Nuclear Instruments and Methods In Physics Research*, 208(1-3):65–77, 1983.

[148] J. Greer. *Wire Electrical Discharge Machining of Helical Devices from Permanent Magnets*. Master's thesis, University of Utah, 2011.

[149] H. Takezawa, Y. Ichimura, T. Suzuki, T. Muramatsu, and N. Mohri. Relationship between thermal influence and magnetic characteristics in electrical discharge machining of magnetic materials. *Key Engineering Materials*, 516:575–579, 2012.

[150] J. B. Rosenzweig. Towards an Ultra-Compact X-ray Free-Electron Laser. *New Journal of Physics*, Submitted, 2019.

[151] K. Atallah and D. Howe. The application of halbach cylinders to brushless AC servo motors. *IEEE Transactions on Magnetics*, 34(4 PART 1):2057–2059, 1998.

[152] Z.Q. Zhu and D. Howe. Halbach permanent magnet machines and applications: a review. *IEE Proceedings - Electric Power Applications*, 148(4):299, 2002.

[153] D. Zhu, S. Beeby, J. Tudor, and N. Harris. Increasing output power of electromagnetic vibration energy harvesters using improved Halbach arrays. *Sensors and Actuators, A: Physical*, 203:11–19, 2013.

[154] H. Leupold. Triangular section permanent magnetic structure. *USPTO*, 5014028, 1991.

[155] D. C. Quimby, A. L. Pindroh, and K. E. Robinson. The wedged-pole concept for improving the performance of permanent magnet hybrid undulators. *Nuclear Inst . and Methods in Physics Research , A*, 259:304–311, 1987.

[156] A. A. Varfolomeev, A. H. Hairetdinov, S. N. Ivanchenkov, A. S. Khlebnikov, and N. S. Osmanov. Undulator scheme providing wide range magnetic field tuning. *Nuclear Inst. and Methods in Physics Research, A*, 341(1-3):459–461, 1994.

[157] H. Wang, P. Bencok, P. Steadman, E. Longhi, J. Zhu, and Z. Wang. Complete polarization analysis of an APPLE II undulator using a soft X-ray polarimeter. *Journal of Synchrotron Radiation*, 19(6):944–948, 2012.

[158] A. Temnykh, T. Kobela, A. Lyndaker, J. Savino, E. Suttner, and Y. Li. Compact undulator for cornell high energy synchrotron source. *IEEE Transactions on Applied Superconductivity*, 22(3), 2012.

[159] C. C. Wright, R. A. Stuart, J. Lucas, and A. Al-Shamma'A. Low cost undulator magnets for industrial free electron masers. *Optics Communications*, 185(4-6):387–391, 2000.

[160] Q. Jia. Effect of undulator harmonics field on free-electron laser harmonic generation. *Physical Review Special Topics - Accelerators and Beams*, 14(6):1–5, 2011.

[161] B. M. Kincaid. Analysis of field errors in existing undulators. *Nuclear Inst. and Methods in Physics Research, A*, 291:363–370, 1990.

[162] P. Musumeci, C. Pellegrini, and J. B. Rosenzweig. Higher harmonic inverse free-

electron laser interaction. *Physical Review E - Statistical, Nonlinear, and Soft Matter Physics*, 72(1):1–10, 2005.